Summer 2016

Terahertz nonlinear optical response of armchair graphene nanoribbons

Yichao Wang
University of Iowa

TERAHERTZ NONLINEAR OPTICAL RESPONSE OF ARMCHAIR GRAPHENE NANORIBBONS

by

Yichao Wang

A thesis submitted in partial fulfillment
of the requirements for the Doctor of Philosophy
degree in Electrical and Computer Engineering in the
Graduate College of
The University of Iowa

August 2016

Thesis Supervisor: Professor David R. Andersen

Graduate College
The University of Iowa
Iowa City, Iowa

CERTIFICATE OF APPROVAL

PH.D. THESIS

This is to certify that the Ph.D. thesis of

Yichao Wang

has been approved by the Examining Committee for
the thesis requirement for the Doctor of Philosophy degree
in Electrical and Computer Engineering at the August 2016 graduation.

Thesis committee: _____
David R. Andersen, Thesis Supervisor

_____
Michael E. Flatté

_____
Thomas F. Boggess

_____
Soura Dasgupta

_____
Anton Kruger

To my family
Jinliang, Yuling, Yiqun,
Xiaoling, and Yijie

After endless mountains and rivers that leave doubt whether there is a path out,
suddenly one encounters the shade of a willow, bright flowers and a lovely village.

You Lu

First, there is a mountain, then there is no mountain, then there is.

Zen Aphorism

ACKNOWLEDGEMENTS

First and foremost, I would like to express my deepest gratitude to my advisor, Professor David R. Andersen, for all his time, support and guidance on my research work, without his input and extensive knowledge this thesis would not be possible. I appreciate his vast knowledge and skills in many areas of physics and optics. His insightful comments have greatly shaped my Ph.D. research. It is impossible to complete my thesis without his guidance.

Prof. Andersen has supported me not only academically but also emotionally throughout my Ph.D. journey. I have learned many great things from him, not only the knowledge, but also critical & creative thinking, research attitude and passions for the research. I am so grateful that he never made me feel incapable when I encountered hard times. He was always willing to share his life and interest with me. The many hourly long conversations about different topics of interesting stuff in life, culture, history, hobbies, family and experiences made me optimistic for my life. A couple of afternoon drinks with him were also invaluable memories too.

I would like to extend my profound gratitude to Prof. Hassan Raza for his mentorship and discussion on the research I worked on. I would like also to thank my thesis committee members: Prof. Michael E. Flatté, Prof. Thomas F. Boggess, Prof. Soura Dasgupta and Prof. Anton Kruger for serving as my dissertation committee members for their insightful and valuable comments on my thesis.

Many thanks are due to my friends Dr. Ahmad Umair, Dr. Junjie Bai and

Jin Xin for their help, which have greatly brightened up my Ph.D. life.

Last but not least, I would like to extend my greatest gratitude to my family. My father worked very hard in the last two decades to give me a better platform. He has always been supportive of me in so many ways, without all his sacrifices, I will not even have a chance to purse my Ph.D. life. My mother is always there for me to help me endure the difficult times and show unconditional faith in me. To my twin brother, you are always the mirror of my soul, have overcome many difficulties and achieved great things these years.

ABSTRACT

It has become increasingly apparent that the future of next generation of electronic devices can and will rely on graphene nanoribbons. Graphene nanoribbons and sister structures showcase several key properties that can address the emerging need of terahertz science and technology, and break through the many technological limits on conventional semiconductor electronics operating in the terahertz spectrum.

In this thesis, we focus on the study of the terahertz nonlinear optical response of metallic armchair graphene nanoribbons and sister structures using a $\mathbf{k} \cdot \mathbf{p}$ model and time dependent perturbation theory. We find that these nanoribbons exhibit a stronger interband optical response, and a smaller critical field strength (of the order of 10 kV/m) than does 2D single layer graphene. We demonstrate that finite ribbon size, spatial profile of the applied terahertz radiation field, polarization of the applied terahertz radiation, a small band gap opening, and application of a superlattice potential are several ways to tune the strong terahertz nonlinear optical response of metallic armchair graphene nanoribbons.

The major contributions of this thesis include: 1) developes of a simpler method compared to other sophisticated methods of the terahertz nonlinear optical interband response of metallic armchair graphene nanoribbons; 2) extends the method in the characterization of various quantum size effects, elliptically polarized radiation field, small gap opening and superlattice on the terahertz optical response of these nanoribbons; 3) The versatility of the tunability showed in the terahertz

nonlinear response of metallic armchair nanoribbons and sister structures will help advance the development of the nonlinear terahertz armchair graphene nanoribbon opto-electronic and photonic technology.

PUBLIC ABSTRACT

Over the last decade, the world has been searching for the next generation of electronics that harvest terahertz spectrum. Conventional semiconductor electronics have encountered difficult fundamental challenges due to the physical limits of current technology. Graphene-based electronics are expected to be the basic building blocks for a wealth of new device applications, *i.e.* high speed electronic devices, medical, security, imaging, ultrafast wireless communications, display, automotive, wearable devices, and energy storage.

In this thesis, a simple method is developed and shows that metallic armchair graphene nanoribbon and its sister structures exhibit a strong terahertz nonlinear response and great tunability. Our analysis provides new advances in the fundamental understanding of metallic armchair graphene nanoribbons. Our result sets the stage for the development of the nonlinear terahertz armchair nanoribbon opto-electronic and photonic technology.

TABLE OF CONTENTS

LIST OF TABLES

Table

LIST OF FIGURES

Figure

CHAPTER 1
INTRODUCTION

1.1 Motivation

There has been a significant paradigm shift in the world of conventional semiconductor electronics with the foreseeable failure of Moore's Law. Device size limit, power/heat consumption, as well as quantum interference all serve as fundamental challenges that are difficult to overcome for the conventional semiconductor electronics. New horizons have opened with the emergence of graphene-based disruptive technologies in the last decade. Graphene based materials have many unique physical, electrical, optical, chemical, thermal biological and mechanical properties (see Fig. 1.1) when compared to conventional semiconductors [1,2]. Graphene is expected to have a major impact in various fields, serving as the basic building block for a wealth of new device applications (see Fig. 1.2), which cannot (or may be difficult to) be achieved with the conventional electronics [1].

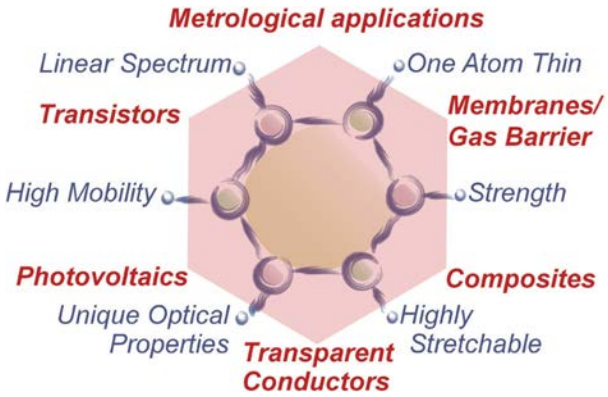

Figure 1.1: Graphene properties and its related application areas. This figure is obtained from [1].

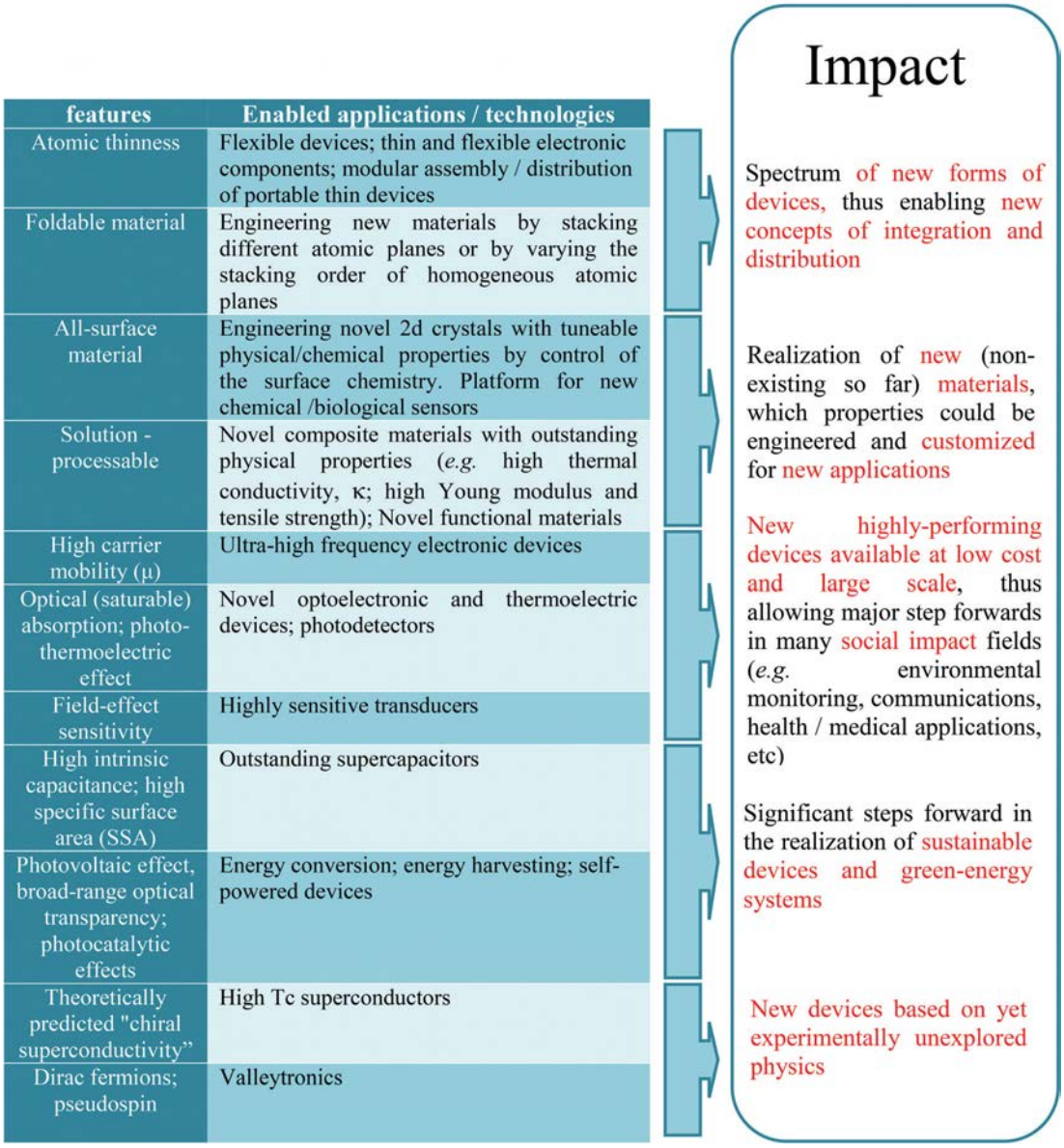

Figure 1.2: Graphene based platform for new technologies and applications, with **disruptive**, *not incremental* advances. This figure is obtained from [1].

Herbert Kroemer, one of the Laureates of the 2010 Nobel Prize in Physics, proposed the "Lemma of New Technology": "*The principal applications of any sufficiently new and innovative technology always have been and will continue to be applications* **created** *by that technology*" [3]. Rapidly-advancing research and devel-

opment activities in the last decade have already shown graphene as a very promising candidate for the basic building block of the next generation of electronics, offering great opportunities and benefits to science, technology and society as a whole [1]. Thus graphene is no exception to this lemma, and becomes disruptive in terms of offering not incremental, but orders of magnitude improvements when compared to the conventional electronics [1]. Graphene has many potential novel applications, including but not limited to, charge-based high speed electronic devices, spintronic devices, and energy storage devices (*e.g.* advanced batteries and supercapacitors) [1]. Fig. 1.3 shows the wide range of applications of graphene [1].

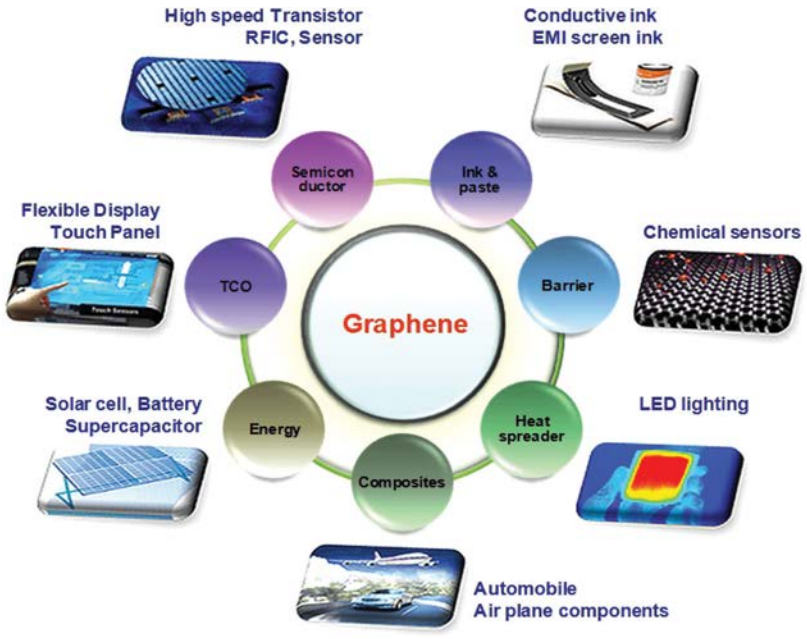

Figure 1.3: Overview of Applications of Graphene, ranging from conductive ink to chemical sensors, light emitting devices, composites, energy, touch panels and high frequency electronics. This figure is obtained from [1].

The International Technology Roadmap for Semiconductors considers graphene one of the promising candidates for post-Si conventional electronics [1]. The great potential of graphene is demonstrated by the soaring number of academic publications, patents and industrial activities in the last decade [1]. Progress in the state of art of the production of various graphene structures has been impressive [1, 4, 5].

1.2 Tunability of the terahertz nonlinear response of graphene nanoribbon structures

The terahertz (THz) spectrum region has been fairly unexploited using conventional semiconductors, especially given the difficulty in identifying the THz photon, which is usually below the thermal energy. The THz field has many promising applications due to its non-ionizing and low-energy characteristics, *e.g.* medical, security, imaging, ultrafast wireless communications, display, automotive, wearable devices and energy storage [1]. Furthermore, active devices at THz working frequencies are vital to the conversion of high frequency radiation (particularly solar THz radiation spectrum), which can lead to a self-powered behavior of devices [1]. Graphene has a linear dispersion, a constant Fermi velocity, easy tunability and the potential for band gap engineering [2, 6–8], thus graphene exhibits decisive advantage over all available conventional semiconductors in the THz spectral region to harvest the THz operation frequencies [1].

Fig. 1.4 shows the timeline of possible device applications and functional device prototypes. It is expected that there will be breakthroughs in high-speed graphene

nanoribbon THz optoelectronics [1]. Due to the linear band dispersion shown in metallic armchair graphene nanoribbons in the THz spectrum, it is therefore possible to generate charge carriers in these nanoribbons by optically stimulated direct inter-band transitions over the entire THz spectrum, a functionality unmatched by any known material [1, 9, 10].

Nonlinear effects can be used to broaden the already wide spectral range of graphene and provide a larger response. Nonlinear frequency conversion (*e.g.* higher harmonic generation, parametric oscillation and amplification, four-wave mixing, and super-continuum generation) is also useful to expand the working spectral region [1]. In particular, the development and optimization of the performance of THz graphene nanoribbon devices will contribute greatly to the technological progress in graphene.

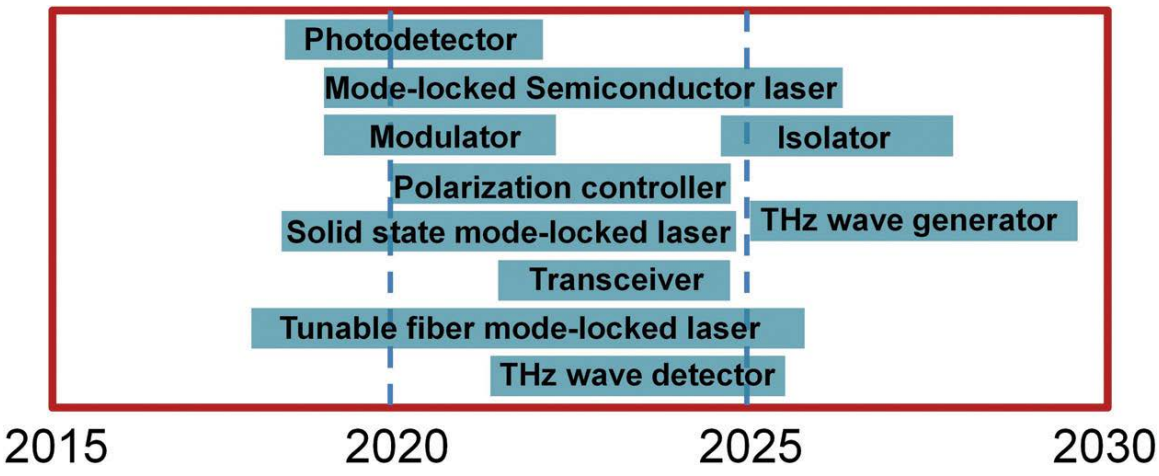

Figure 1.4: Graphene device applications timeline. The rectangles in the figure indicate the timeframe when functional device prototypes could be expected. This figure is obtained from [1].

The state of art progress toward precision atomic-scale graphene nanoribbon nanodevices will make these nanodevices a strong platform in the single-molecular electronics paradigm [11], and advance Boolean information processing [1]. As graphene nanoribbons allow quantum qubits due to the spin and valley [12–15], these might add an additional degree freedom in the future design of highly-integrated molecular Boolean logic circuit and quantum computing [1, 8, 16–21].

In most of the existing semiconductor technologies, the typical length-scale of THz devices is large [1]. However, graphene THz devices can be achieved at smaller length-scales. A typical linear THz device size is of the order of several µm, so one needs to consider the finite size effect of graphene nanoribbons too. With THz devices of the µm scale, one needs to consider the discrete electronic spectrum due to quantization, charge quantization and other effects caused by finite size [1]. As thin graphene nanoribbons may be treated as quasi-1D quantum wire [22], this requires an understanding of the nonlinear optical properties of the response of graphene nanoribbons due to the reduced dimensionality [1].

Band gaps can be tuned via different edge terminations, electric, magnetic modulation, chiral vector potential (*e.g.* kink, twisting), *etc.* [23–31]. The prospect of band gap engineering in graphene nanoribbon leads to the long term goal of producing graphene nanoribbons on demand, and achieves top-down control of graphene nanostructuring [1]. The engineering of graphene nanoribbon bandgaps lead to the further optimization of the THz response of graphene, *e.g.* small gap openings can induce second harmonic generation, and show larger nonlinearities in the linear forbidden

excitation region [8, 32–34].

Active control of THz polarization spectroscopy is vital for optical material characterization and various applications in communication theory. Unlike conventional semiconductors, Graphene nanoribbons can be easily tuned electrically in the THz range. Therefore, THz spectroscopy of graphene nanoribbons can lead to ultra-thin THz polarization modulators [1].

Another way to modulate and tune graphene nanoribbons is by means of superlattice. A superlattice is a large-scale periodic patterning of graphene, which can change the properties and THz response of the structure [1,35]. The manufacture and characterization of graphene nanoribbon superlattices is a challenging yet promising direction for device applications. The versatility of the tunability of graphene nanoribbons means that these structures may enable novel nonlinear optical, electronic and photonic devices working in a wide range of frequencies, including THz, with extremely high speed, high response, low driving voltage, low power consumption and compact footprints [1].

1.3 Overview of thesis

This thesis contains eight chapters and two appendices. The following is an overview of the remaining contents:

1. Chapter 2 provides the background for the electronic properties of graphene and armchair graphene nanoribbons. In it, the $\mathbf{k} \cdot \mathbf{p}$ Hamiltonian is derived from the tight-binding method, and is used to obtain the Hamiltonian of various

graphene structures. It also introduces briefly the N-photon coupling approach adopted in this thesis.

2. Chapter 3 serves as a basis of the computation of the THz nonlinear direct interband transition of infinitely long metallic armchair graphene nanoribbons with an applied linearly polarized electric field under relaxation free approximation.
3. Chapter 4 studies the effects of finite ribbon size, finite applied field spatial profile, and the scattering mechanism on the THz nonlinear response of metallic armchair graphene nanoribbons with an applied linearly polarized electric field.
4. Chapter 5 shows the calculation of the third order THz nonlinear response with an applied elliptical polarized electric field.
5. Chapter 6 demonstrates how small band gap openings affect the third order THz nonlinear response with an applied linearly polarized electric field.
6. Chapter 7 provides a theoretical calculation of the third order THz nonlinear response with an applied elliptical polarized electric field of a metallic armchair nanoribbon superlattice structure
7. Chapter 8 summarizes the conclusions and provide the outlooks for the development of armchair graphene nanoribbons based device applications.
8. The appendices provide some useful details for the derivation performed in Chapter 3.

CHAPTER 2
ELECTRONIC PROPERTIES OF GRAPHENE AND ARMCHAIR GRAPHENE NANORIBBON

2.1 Electronic properties of 2D single layer graphene

We use the tight-binding approximation up to the nearest neighbor atom to derive the electron band structure of 2D single layer graphene, in the massless Dirac equation ($\mathbf{k}\cdot\mathbf{p}$ approximation), which is valid at low energies.

2.1.1 Tight binding approximation in 2D single layer graphene

Graphene is a 2D hexagonal lattice (honeycomb) structure of covalently bonded carbon atoms. The carbon atom has 6 electrons in the nucleus ($1s^2 2s^2 2p^2$). The nature of the chemical bonds of carbon atom determines the graphene structure. In graphene, electrons occupying the external orbitals of the carbon nucleus $2s^2 2p^2$, are mixed to the sp^2 hybridization of the $2s$, $2p_x$ and $2p_y$. The fourth valence electron shells are half filled in the $2p_z$ orbital, which is orthogonal to the graphene sheet. The overlap of these half filled $2p_z$ orbitals form the $\pm\pi$ electrons. As a result, the electronic properties of graphene are determined by the delocalized π electrons [2,6]. As mentioned above, the graphene structure is determined by a honeycomb hexagonal lattice with two atoms in a unit cell (see Fig. 2.1). We may choose the basis of the unit cell in real space as

$$\mathbf{a_1} = a_0\,(1,0)\,, \quad \mathbf{a_2} = a_0\left(-\frac{1}{2}, \frac{\sqrt{3}}{2}\right)$$

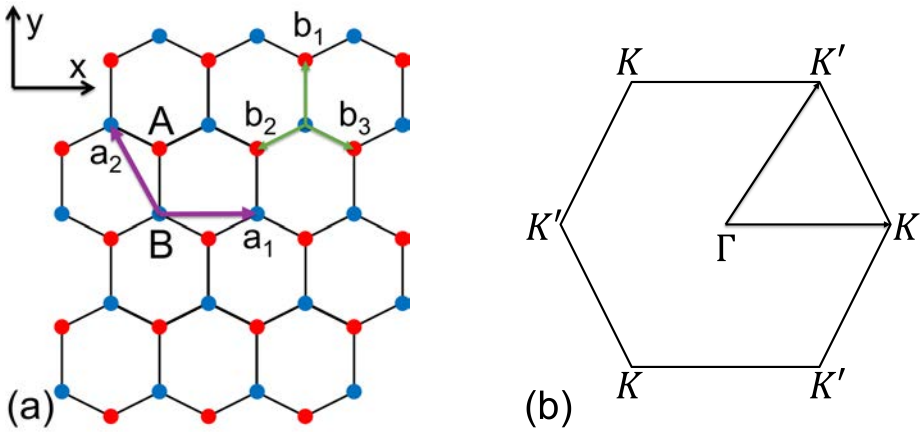

Figure 2.1: a) Graphene honeycomb lattice structure. Basis vectors in the unit cell are $\mathbf{a_1}$ and $\mathbf{a_2}$, A and B atoms of the unit cell. b) First Brillouin zone (BZ). The Dirac points K and K' are described by the massless Dirac equation, and are the vertex points of the BZ.

and the vectors connecting the nearest neighbor atoms are given by:

$$\mathbf{b_1} = a_{cc}\,(1,0)\,, \quad \mathbf{b_2} = a_{cc}\left(-\frac{\sqrt{3}}{2}, -\frac{1}{2}\right), \quad \mathbf{b_3} = a_{cc}\left(\frac{\sqrt{3}}{2}, -\frac{1}{2}\right)$$

where the lattice constants $a_{cc} = a_0/\sqrt{3} \simeq 1.42\,\text{Å}$.

The basis set for the reciprocal lattice is:

$$\mathbf{c_1} = \frac{2\pi}{a_0}\left(1, \frac{1}{\sqrt{3}}\right), \quad \mathbf{c_2} = \frac{2\pi}{a_0}\left(0, \frac{2}{\sqrt{3}}\right)$$

The first BZ is a hexagon (Fig. 2.1b), where the vertex points are called the Dirac points. There are two inequivalent Dirac points per BZ, traditionally labeled K and K', with the vector from the center Γ of the BZ :

$$\mathbf{K} = \frac{2\pi}{a}\left(\frac{2}{3}, 0\right), \quad \mathbf{K'} = \frac{2\pi}{a}\left(\frac{1}{3}, \frac{1}{\sqrt{3}}\right)$$

The electronic properties of graphene are well-described by the tight binding approximation of the $\pm\pi$ bonds [2, 6]. Let us define the creation (annihilation) operator, $c^{\dagger}_{\mathbf{R}}$ ($c_{\mathbf{R}}$) that creates (annihilates) a free p_z orbital electron at the lattice point $\mathbf{R} = x\hat{x} + y\hat{y}$, *e.g.*, $|p_z(\mathbf{R})\rangle = c^{\dagger}_{\mathbf{R}}|0\rangle$. The hopping parameter $\gamma_0 \approx 2.8\,\mathrm{eV}$ represents the coupling between nearest neighbor p_z orbitals. Thus the tight binding Hamiltonian for electron energies near the p_z orbital in graphene is [6]:

$$H = -\gamma_0 \sum_{\mathbf{R_A},\mathbf{b_j}} c^{\dagger}_{\mathbf{R_A}} - \mathbf{b_j}\, c_{\mathbf{R_B}} - \gamma_0 \sum_{\mathbf{R_B},\mathbf{b_j}} c^{\dagger}_{\mathbf{R_B}} - \mathbf{b_j}\, c_{\mathbf{R_B}} \tag{2.1}$$

where the sum contains the sum of two sublattices $\mathbf{R_A} = n_1\mathbf{a_1} + n_2\mathbf{a_2} + \mathbf{b_j}$ and $\mathbf{R_B} = n_1\mathbf{a_1} + n_2\mathbf{a_2}$, with n_1, $n_2 \in \mathbb{Z}$. If we set the energy of the p_z orbital to zero, eigenstates of the Hamiltonian (2.1) can be expanded as a Bloch function [2, 6]:

$$H = \frac{1}{\sqrt{N}} \sum_{\mathbf{R_A}} e^{i\mathbf{k}\cdot\mathbf{R_A}} c^{\dagger}_{\mathbf{R_A}} f_A(\mathbf{k}) + \frac{1}{\sqrt{N}} \sum_{\mathbf{R_B}} e^{i\mathbf{k}\cdot\mathbf{R_B}} c^{\dagger}_{\mathbf{R_B}} f_B(\mathbf{k}) Z \tag{2.2}$$

where the magnitude of the complex phase term $|Z| = 1$. After some algebra, the Hamiltonian (2.1) becomes:

$$H = -\gamma_0 \sum_{\mathbf{k}} \left(\sum_j Z^* e^{i\mathbf{k}\cdot\mathbf{b_j}} \cdot B^{\dagger}_{\mathbf{k}} A_{\mathbf{k}} + c.c. \right) \tag{2.3}$$

where $A_{\mathbf{k}}(B_{\mathbf{k}})$ are the Fourier transform of $c_{\mathbf{R_A}}(c_{\mathbf{R_B}})$. Eq. (2.3) contains an important energy weighting function, $T(\mathbf{k})$:

$$T(\mathbf{k}) = -\gamma_0 \sum_{\mathbf{k}} \sum_j Z e^{-i\mathbf{k}\cdot\mathbf{b_j}}$$

As a result, the Hamiltonian (2.3) can be expanded in matrix form:

$$H = \sum_{\mathbf{k}} \begin{pmatrix} A^{\dagger}_{\mathbf{k}} & B^{\dagger}_{\mathbf{k}} \end{pmatrix} \begin{pmatrix} 0 & T(\mathbf{k}) \\ T^*(\mathbf{k}) & 0 \end{pmatrix} \begin{pmatrix} A_{\mathbf{k}} \\ B_{\mathbf{k}} \end{pmatrix} \tag{2.4}$$

With the Bloch state satisfying $c_{\mathbf{k}}^{\dagger} = f_A(\mathbf{k})A_{\mathbf{k}}^{\dagger} + f_B(\mathbf{k})B_{\mathbf{k}}^{\dagger}$, the energy dispersion can be obtained by the following eigenvalue relation:

$$\begin{pmatrix} 0 & T(\mathbf{k}) \\ T^*(\mathbf{k}) & 0 \end{pmatrix} \begin{pmatrix} f_A(\mathbf{k}) \\ f_B(\mathbf{k}) \end{pmatrix} = E(\mathbf{k}) \begin{pmatrix} f_A(\mathbf{k}) \\ f_B(\mathbf{k}) \end{pmatrix} \tag{2.5}$$

The energy dispersion is obtained by setting the determinant:

$$\begin{vmatrix} -E(\mathbf{k}) & T(\mathbf{k}) \\ T^*(\mathbf{k}) & -E(\mathbf{k}) \end{vmatrix} = 0 \tag{2.6}$$

The solution of Eq. (2.6) determines the energy dispersion [2,6] of the band structure in 2D single layer graphene (SLG):

$$\epsilon(\mathbf{k}) = s\sqrt{T(\mathbf{k})T^*(\mathbf{k})} = s\gamma_0\sqrt{1 + 4\cos\left(\frac{ak_x}{2}\right)\cos\left(\frac{ak_y\sqrt{3}}{2}\right) + 4\cos^2\left(\frac{ak_x}{2}\right)} \tag{2.7}$$

and the eigenstate:

$$\xi(\mathbf{k}) = \frac{1}{\sqrt{2}} \begin{pmatrix} 1 \\ e^{-i\phi(\mathbf{k})} \end{pmatrix} \tag{2.8}$$

where $\phi(\mathbf{k}) = \arg[T(\mathbf{k})]$, the complex argument of $T(\mathbf{k})$, and $s = \pm 1$ the conduction-valence band index. Fig. 2.2 shows the energy dispersion of 2D intrinsic SLG. We note the special behavior of the conduction and valence bands near the Dirac points $\mathbf{K}$ and $\mathbf{K}'$. The conduction band and valence band cones touch precisely at the Dirac points. Thus, 2D intrinsic SLG is a zero gap semiconductor in general.

2.1.2 Dirac Continuum model under $\mathbf{k} \cdot \mathbf{p}$ approximation

We now make a Taylor expansion near the $\mathbf{K}$ and $\mathbf{K}'$ points up to the first order, and shift the coordinate with respect to the Dirac points, namely $\mathbf{k} \to \mathbf{k} + \mathbf{K}$ for $|\mathbf{k}| \ll |\mathbf{K}|$ and $\mathbf{k}' \to \mathbf{k}' + \mathbf{K}'$ for $|\mathbf{k}'| \ll |\mathbf{K}'|$. Now $T(\mathbf{k})$ can be expanded as follows:

$$T(\mathbf{k}) = -\gamma_0 \sum_j Z e^{-i(\mathbf{k}+\mathbf{K})\cdot\mathbf{b_j}} \approx -\gamma_0 \sum_j Z e^{-i\mathbf{K}\cdot\mathbf{b_j}} (1 - i\mathbf{k}\cdot\mathbf{b_j}) \tag{2.9}$$

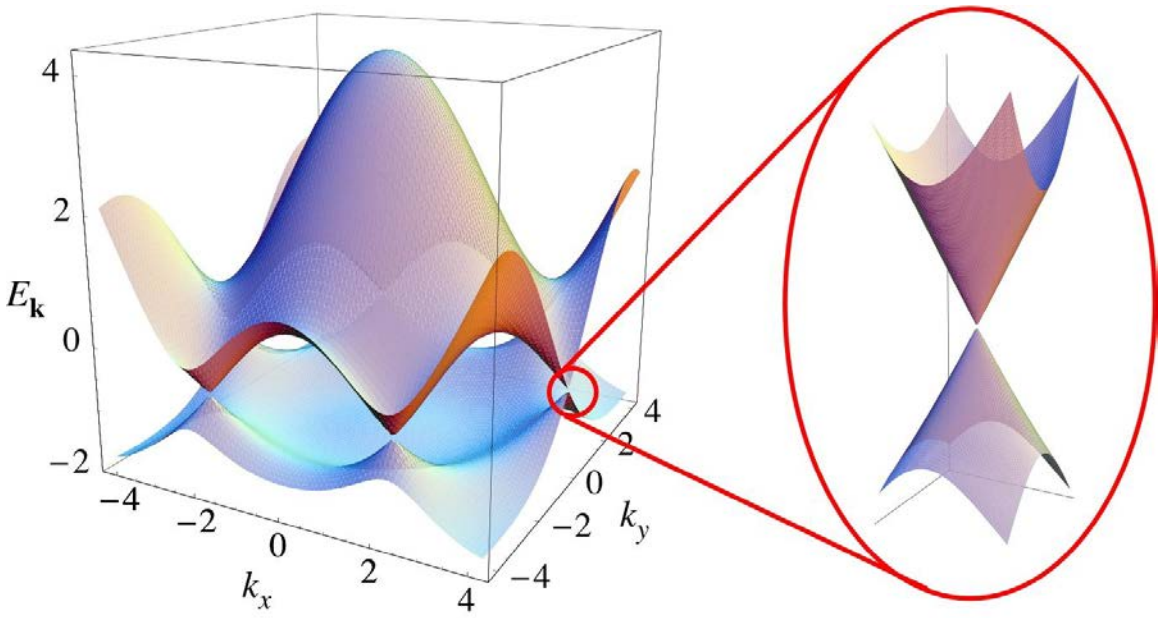

Figure 2.2: Energy dispersion of 2D intrinsic SLG. Left: Band structure (in units of $\Gamma_0 = 2.8\,\mathrm{eV}$) Right: Band Structure of the Dirac Cones. This figure is from [6].

After some algebra, the sums in Eq. (2.9) become:

$$\sum_j e^{-i\mathbf{K}\cdot\mathbf{b_j}} = 0$$

$$\sum_j \mathbf{b_j} e^{-i\mathbf{K}\cdot\mathbf{b_j}} = e^{-i\frac{2\pi}{3}} \frac{\sqrt{3}}{2} a \left(i\hat{x} + \hat{y}\right)$$

With the phase term $Z = e^{-i\pi/3}$ in Eq. (2.2), we obtain the expression for $T(\mathbf{k})$ and the effective Hamiltonian H_K in the vicinity of the Dirac point $\mathbf{K}$, or the Dirac continuum model in the $\mathbf{k}\cdot\mathbf{p}$ approximation:

$$T(\mathbf{k}) = \gamma_0 i\mathbf{k}\cdot\sum_j \mathbf{b_j} Z e^{-i\mathbf{K}\cdot\mathbf{b_j}} = \frac{\sqrt{3}}{2} a\gamma_0 \left(k_x - ik_y\right) \tag{2.10}$$

$$H_K = \frac{\sqrt{3}}{2} a\gamma_0 \begin{pmatrix} 0 & k_x - ik_y \\ k_x + ik_y & 0 \end{pmatrix} \tag{2.11}$$

It is convenient to introduce the Fermi velocity $v_F = \sqrt{3}a\gamma_0/(2\hbar) \approx 1 \times 10^6\,\mathrm{m/s}$ [2,6]. In this case, the Hamiltonian (2.11) for $\mathbf{K}(\mathbf{K}')$ valley reduces to:

$$H_K = \hbar v_F \boldsymbol{\sigma} \cdot \mathbf{k} \tag{2.12}$$

$$H_{K'} = \hbar v_F \boldsymbol{\sigma} \cdot \mathbf{k}' \tag{2.13}$$

where $\mathbf{k}(\mathbf{k}') = \pm\hat{x}k_x + \hat{y}k_y$, $\boldsymbol{\sigma} = \hat{x}\sigma_x + \hat{y}\sigma_y$, and:

$$\sigma_x = \begin{pmatrix} 0 & 1 \\ 1 & 0 \end{pmatrix}, \quad \sigma_y = \begin{pmatrix} 0 & -i \\ i & 0 \end{pmatrix}$$

are Pauli spin matrices.

With this Dirac continuum model in the $\mathbf{k}\cdot\mathbf{p}$ approximation, low energy graphene carriers near the vicinity of Dirac points $\mathbf{K}$ behave exactly like massless Dirac fermions with spin 1/2, or the pseudospin of graphene. The energy dispersion for H_K and the wavefunctions of H_K are obtained by solving the eigenvalue equation $H_K\psi_k = \epsilon(\mathbf{k})\psi_k$:

$$\epsilon(\mathbf{k}) = s\hbar v_F|\mathbf{k}| = s\hbar v_F\sqrt{k_x^2 + k_y^2} \tag{2.14}$$

$$\psi_k(\mathbf{r}) = \langle \mathbf{r}|s\mathbf{k}\rangle = \frac{1}{\sqrt{2}}\begin{pmatrix} s \\ e^{i\theta(\mathbf{k})} \end{pmatrix} \tag{2.15}$$

with the isospin angle $\tan[\theta(\mathbf{k})] = k_y/k_x$. Similarly, massless Dirac fermions near $\mathbf{K}'$ are described by $H_{K'} = \hbar v_F \boldsymbol{\sigma}\cdot\mathbf{k}'$, with $\mathbf{k}' = \hat{x}k'_x + \hat{y}k'_y = -\hat{x}k_x + \hat{y}k_y$. As the energy dispersion of $H_{K'}$ has the same expression for the $\mathbf{K}$ valley (see Fig. 2.2), so we have another degree freedom like the electron spin $g_s = 2$, the valley degeneracy $g_v = 2$ for the Dirac fermions [2, 6, 36].

2.2 Mesoscopics in graphene: Dirac points in graphene ribbons

Thin graphene nanoribbons (width sub-20 nm) may be treated as quasi 1D quantum wire [22]. Due to the small scale of graphene nanoribbon based structures and devices, quantum mechanics is known to affect the mesoscopic properties of such systems profoundly. These mesoscopic quantum effects in graphene nanoribbon based systems make tehm an attractive candidate for fast and compact electronic and optical devices [37].

The basic mesoscopic physics of how small size affects the electronic properties of semiconductors are well studied [38]. The electronic properties of conventional mesoscopic semiconductors are well described by the simplest model, the Schrödinger equation for electrons moving inside the semiconductors with an appropriate effective mass. Such a conventional model treats electrons as non-interacting particles, confined in the region defined by some effective potential due to the structure of the semiconductors, rather than free electrons in a vacuum [37].

However, electrons in graphene are not accounted for within this simple conventional model [37]. As shown in Section 2.1.2, the low energy electrons in the graphene honeycomb lattice structures are governed by the massless Dirac equation. The wavefunction, Eq. (2.15) has two components, acting as an effective spinor, and exhibiting pseudospin. The direction of the spinor changes with the wavefunction and the Berry's phase associated with it. These effects lead to quantum interference effects, completely different from electrons in conventional semiconductor systems. In the low energy Dirac continuum model in the $\mathbf{k} \cdot \mathbf{p}$ approximation, when inter and

intravalley scattering is negligible, these unusual electronic and quantum effects for the Dirac fermions associated with the quasiparticle and pseudospin nature of the wavefunctions become evident [37].

We begin our discussion of the mesoscopics of the Dirac points in *graphene nanoribbons* with the $\mathbf{k}\cdot\mathbf{p}$ approximation. As we are interested in the low-energy states, the electronic spectra and the wavefunctions produced by microscopic tight-binding calculations for graphene nanoribbons [39, 40] may be well described using the simpler Dirac equation under $\mathbf{k}\cdot\mathbf{p}$ approximation [41, 42]. In this approach, wavefunctions are expressed in terms of envelope functions $\psi_K(\mathbf{r}) = [\psi_A(\mathbf{r}), \psi_B(\mathbf{r})]$ and $\psi_{K'}(\mathbf{r}) = [\psi'_A(\mathbf{r}), \psi'_B(\mathbf{r})]$ for states near the $\mathbf{K}$ and $\mathbf{K}'$ points, respectively. The envelope functions may be combined into a four-vector $\psi = (\psi_A, \psi_B, \psi'_A, \psi'_B)^T$, which satisfies the envelope Dirac equation [41,42] (when the inter and intravalley scattering is negligible) $H\Psi = \epsilon\Psi$, with

$$H = \hbar v_F \begin{pmatrix} 0 & k_x - ik_y & 0 & 0 \\ k_x + ik_y & 0 & 0 & 0 \\ 0 & 0 & 0 & -k_x - ik_y \\ 0 & 0 & -k_x + ik_y & 0 \end{pmatrix} \tag{2.16}$$

$\mathbf{k}$ correspondes to the separation in the reciprocal space from the $\mathbf{K}(\mathbf{K}')$ point in the upper left (lower right) block of the Hamiltonian (2.16).

It should be noted that this $\mathbf{k}\cdot\mathbf{p}$ approximation description of graphene nanoribbon carriers is appropriate only at low energies $|\epsilon| \ll \gamma_0$, which is of the order of 2 eV. For Fermi energies E_F greater than the scale of the optical phonon energy 0.2 eV, one needs to use a more basic tight-binding description. For $E_F \ll 0.2$ eV, the description in terms of the block Dirac Hamiltonian should work relatively well [10, 37].

2.2.1 Armchair graphene nanoribbons

In this section, we discuss consequences of the quasiparticle and pseudospin nature of the graphene Dirac fermions in the mesoscopic setting, particularly for metallic armchair graphene nanoribbons in the low energy regime. The geometry for an armchair graphene nanoribbon is illustrated on the top and bottom edges of Fig. 2.3, along with the unit cell denoted by the vertical rectangle used in the corresponding tight-binding calculations. The width of the armchair graphene nanoribbon, is related to the number of atoms along the zigzag edge N, or $L_x = W_{ac} = Na_0/2$.

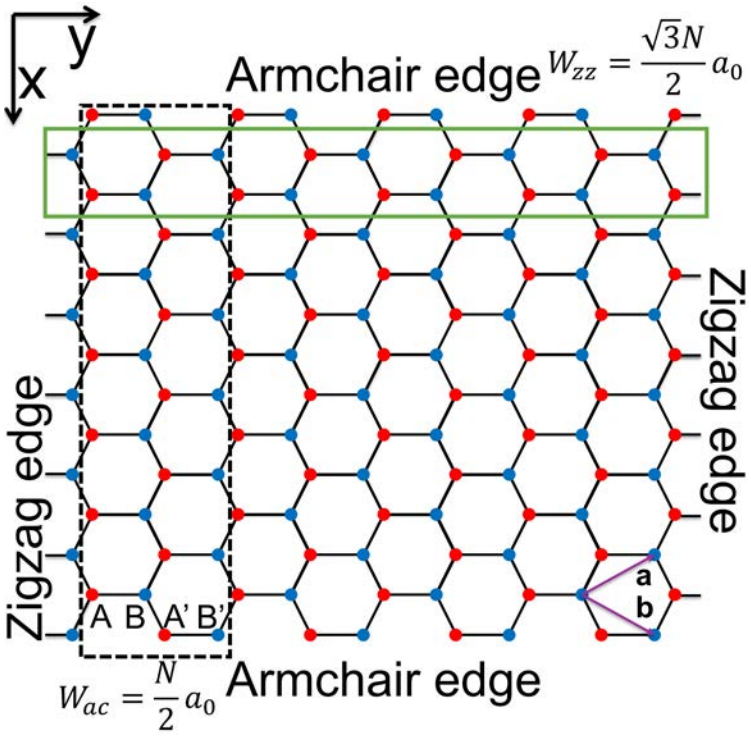

Figure 2.3: The lattice structure of graphene nanoribbon. The lattice is constructed from the vector $n_1\mathbf{a}+n_2\mathbf{b}$, with n_1, $n_2 \in \mathbb{Z}$. Atoms enclosed in the vertical(horizontal) rectangle represent the unit cell of armchair(zigzag) graphene nanoribbons. The width of the unit cell of armchair(zigzag) nanoribbons, $W_{ac}(W_{zz})$, as function of the number of atoms along the zigzag(armchair) edge, N, is also indicated.

The electronic spectra of armchair graphene nanoribbons strongly depend on their width L_x along the zigzag edge. Fig. 2.4 illustrates three examples of the band structure for armchair graphene nanoribbons of different width using the p_z orbital tight-binding up to the first nearest neighbors (pzTB) calculation [43].

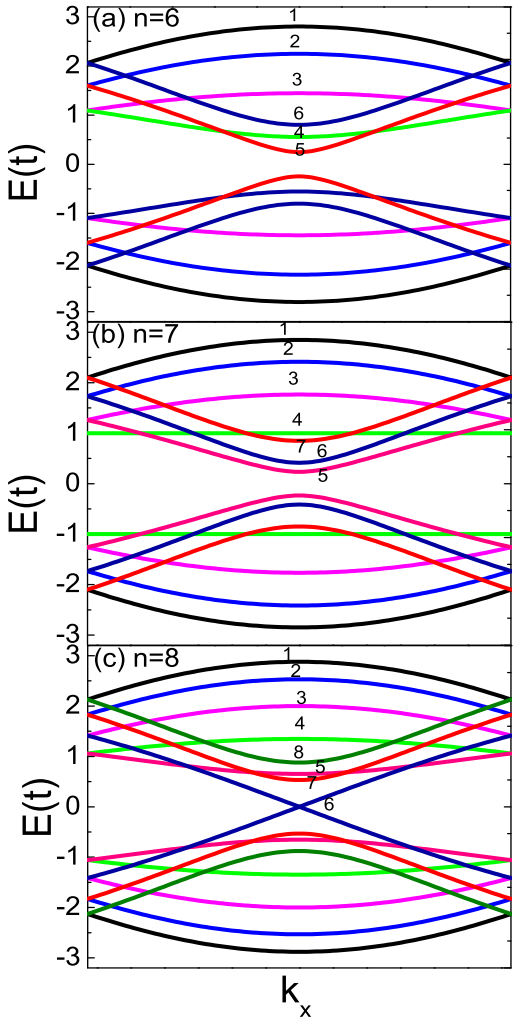

Figure 2.4: pzTB band structure of ideal armchair graphene nanoribbons with various widths (a) $n = 6$, (b) $n = 7$, and (c) $n = 8$ respectively. The value of the subband index in each figure is a convention adopted in [43]. This figure is obtained from [43].

We can see that in Fig. 2.4c, there is a Dirac point, leading to the metallic behavior for intrinsic nanoribbons whereas Fig. 2.4a and Fig. 2.4b are band insulators. In general, armchair graphene nanoribbons of $N = 3M - 1$ atoms wide along the zigzag edge, with M odd, are metallic, whereas all the other cases are semiconductors in the $\mathbf{k} \cdot \mathbf{p}$ approximation [41–43]. The energy of the confined states also behaves in a quantized discontinuous way, and is strongly dependent on the ribbon width L_x [37, 41–43].

This separation in energy as a function of the ribbon width L_x may be understood in terms of the quantization of k_x of the Dirac Hamiltonian (2.16) with the correct boundary conditions. In Fig. 2.3, the termination along armchair edges consists of a line of $A-B$ ($A'-B'$) dimers. It is natural to admix valleys, and require that the wavefunction amplitude vanish on both sublattices [41] at $x = 0$ and $x = L_x + \frac{a_0}{2}$:

$$\phi_\mu(x = 0) = \phi'_\mu(x = 0) \tag{2.17}$$

$$\phi_\mu(x = L_x + \frac{a_0}{2}) = \phi'_\mu(x = L_x + \frac{a_0}{2}) e^{i\Delta_K(L_x + \frac{a_0}{2})} \tag{2.18}$$

where $\mu = A, B$ and $\Delta_K = \frac{4\pi}{3a_0}$. As a result, solutions of the Dirac equation are essentially plane waves of the form:

$$\phi_B(x) = e^{ik_n x} \quad \text{and} \quad \phi'_B(x) = e^{-ik_n x} \tag{2.19}$$

with boundary condition $e^{2ik_n(L_x + \frac{a_0}{2})} = e^{i\Delta_K(L_x + \frac{a_0}{2})}$ derived from Eq. (2.18), the allowed values of k_n for armchair graphene nanoribbons are [41, 42]:

$$k_n = \frac{n\pi}{2L_x + a_0} + \frac{2\pi}{3a_0} \tag{2.20}$$

The admixing of different valley states means that the wavefunction will oscillate with period $2\pi/\Delta_K$ due to the boundary conditions [41, 43]. Such behavior can be

observed in Fig. 2.5, which illustrates the local density states in the lowest conduction or valence band at $k_n = 0$ from the pzTB calculation with various width. The short oscillation in the local density of states has exactly the period expected for the valley mixing due to the boundary conditions [37, 41, 43].

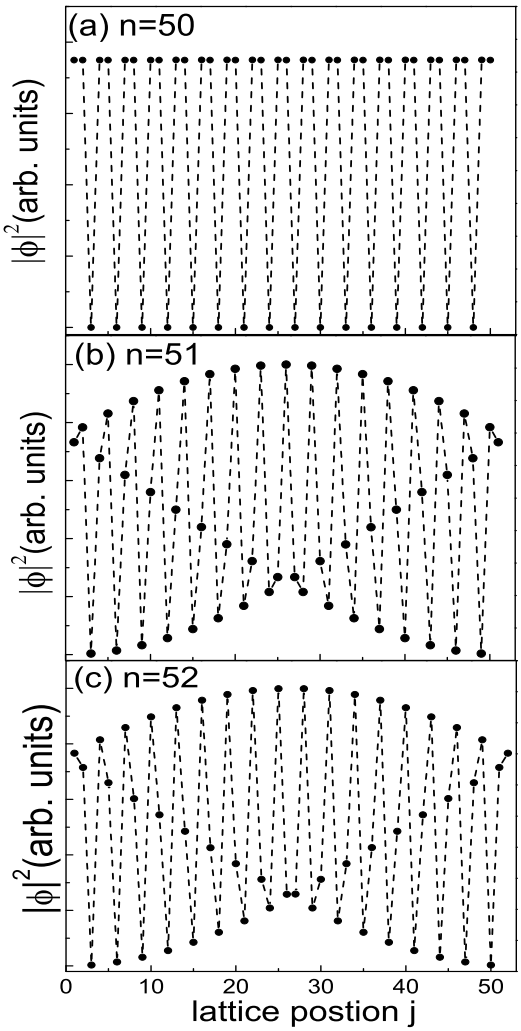

Figure 2.5: Local density of the states calculated using $\mathbf{k} \cdot \mathbf{p}$ and pzTB in the lowest conduction or valence band at $k_n = 0$ for armchair GNRs with various widths, (a) $n = 50$, (b) $n = 51$, and (c) $n = 52$, respectively. This figure is obtained from [43].

As a result, the Brey-Fertig wavefunction for armchair graphene nanoribbons is [41, 42]:

$$\psi_{n,s} = \frac{e^{ik_y y}}{2\sqrt{L_x L_y}} \begin{pmatrix} e^{-i\theta_{k_n,k_y}} e^{ik_n x} \\ s e^{ik_n x} \\ -e^{-i\theta_{k_n,k_y}} e^{-ik_n x} \\ s e^{-ik_n x} \end{pmatrix} \tag{2.21}$$

where the direction of the isospin of the state is $\theta_{k_n,k_y} = \tan^{-1}(k_n/k_y)$ and the energy $\epsilon(\mathbf{k}) = s\hbar\sqrt{k_n^2 + k_y^2}$. Thus for a width of the form $L_x = \frac{3M-1}{2}a_0$ with M odd, the allowed values of $k_n = \frac{2\pi}{3a_0}\frac{M+n}{M}$ create doubly-degenerate states for $n \neq -M$ and when $k_y \to 0$, the existence of a zero energy state indicates that the conduction and valence band touch at the Dirac points. However, we notice that this $\mathbf{k} \cdot \mathbf{p}$ model only predict the metallic acGNRs with $N = 2, 8, 14, \cdots$. In fact, metallic acGNRs are all metallic for the $N = 5, 11, 14, \cdots$ case as well (see Fig. 2.6).

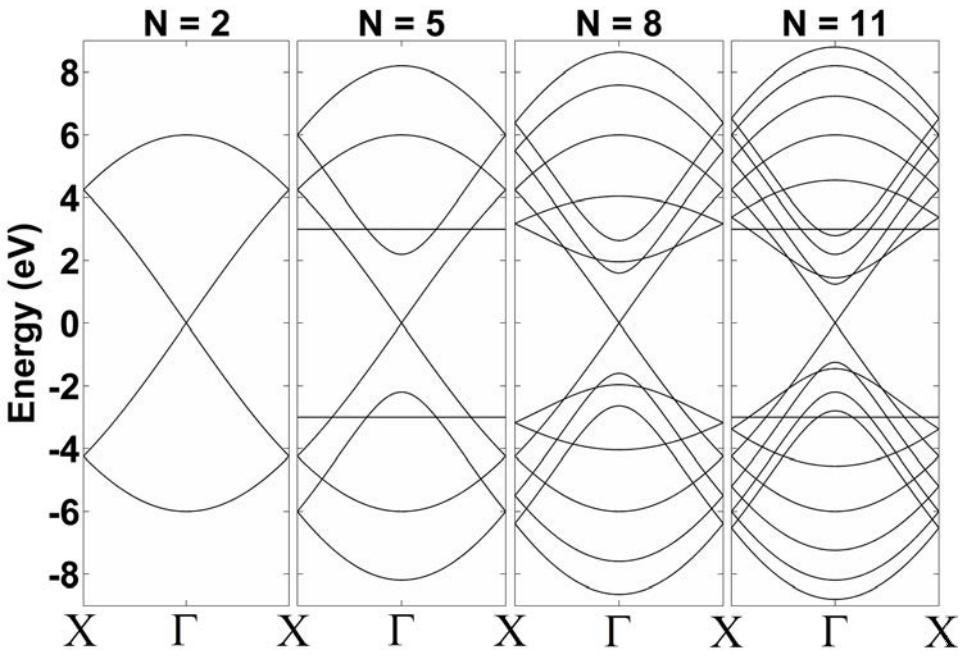

Figure 2.6: pzTB of ideal metallic armchair graphene nanoribbons (a) $n = 2$, (b) $n = 5$, (c) $n = 8$, and (d) $n = 11$ respectively. This figure is obtained from [39].

Armchair graphene nanoribbons with $N \neq 3M - 1$, with M integers are semi-conducting. These semi-conducting armchair graphene nanoribbons have nondegenerate states and do not have Dirac point (zero energy mode).

Lastly, we should mention the chirality in armchair graphene nanoribbons briefly. In general, unlike zigzag graphene nanoribbons, the lowest subbands in semi-conducting armchair graphene nanoribbons do not show chirality due to the admixing of valley states [37]. However, states in the lowest subbands ($k_n = 0$) for metallic armchair graphene nanoribbons do show a chirality. The appearance of the chirality in metallic armchair graphene nanoribbons comes from the symmetry from the interchange of the sublattice and valley indices of the Dirac fermions [37].

2.2.2 Nearly metallic armchair graphene nanoribbons

A bandgap can be opened in 2D SLG if we introduce an asymmetry into the graphene sublattices. This generates an electron-hole asymmetry in the band structure. All experimental reports on the syntheses of high quality GNR show that they have an energy gap, including acGNR that are predicted to be of metallic type under pzTB and $\mathbf{k} \cdot \mathbf{p}$ approximations [5, 44–49] (in what follows, we label gapped nearly-metallic acGNR as m*GNR). The energy gap in these m*GNR is inversely proportional to their width [44–47]. Several theoretical models have predicted the energy gap based on different edge terminations and calculation methods [23–29].

If we define the energy gap $E_{\text{gap}} = 2\hbar\Omega_g = 2\hbar v_F k_\Delta$ and following the $\mathbf{k} \cdot \mathbf{p}$ model for gapped 2D SLG [32,33], and GNR [41,42], the Hamiltonian for m*GNR in

the absence of intravalley and intervalley scattering may be written:

$$H = \hbar v_F \begin{pmatrix} -k_\Delta & k_n - ik_y & 0 & 0 \\ k_n + ik_y & k_\Delta & 0 & 0 \\ 0 & 0 & -k_\Delta & -k_n - ik_y \\ 0 & 0 & -k_n + ik_y & k_\Delta \end{pmatrix} \tag{2.22}$$

where $k_n = \frac{2\pi}{3a_0}\frac{M+n}{M}$, M the number of carton atoms in the $\hat{x}$ direction. For $k_\Delta \to 0$, Hamiltonian (2.22) reduces to the ideally metallic acGNR case.

2.2.3 Metallic armchair graphene nanoribbon superlattice

The electronic structure of armchair graphene nanoribbon structures may be manipulated by an applied external periodic potential, which allows one to *engineer* the band structures of such systems. The manipulation of the periodic potential to tailor the conduction properties of the system opens many possibilities for electronic devices [37].

A superlattice, which is essentially a 1D periodic series of barriers and wells, has a profound effect on the electronic transport properties in graphene. Electron motion along the superlattice axis (parallel to the superlattice wave vector $\mathbf{k}_\lambda$ in the vector space) is the same as the case in the absence of the periodic potential. The physical picture of such an effect is governed by the Klein paradox [37]. When massless Dirac fermions are incident normally upon a sharp potential barrier, the Dirac fermions are transmitted through the barrier rather than reflected as the case for an ordinary Schrödinger particle. This dramatic effect is known as the Klein paradox [2, 6]. One simple explanation for such phenomena is that the reflection of a Dirac fermion requires a 180° rotation of the spinor wavefunction, yielding a state completely perpendicular to the incident one, so that there is no amplitude for

backscattering due to the nature of the spinor structure of the wavefunction.

However, for electrons moving perpendicular to the superlattice axis, the velocity of the electron is degraded, or an anisotropy in the corresponding electron velocity around the Dirac point emerges, which may collimate the flow of electrons [50]. In principle, for a strong enough superlattice or superlattice with a high enough spatial frequency (see Ref. [35]), the electron velocity can be even inverted perpendicular to the superlattice axis. As a result, new Dirac points are generated at zero energy in the band structure and we shall expect that there is a clear signature in transport for the emergence of these new Dirac points [35, 37].

We note that, if new Dirac points emerges from the original Dirac point, the electric response is not quantitatively described by the $\mathbf{k}\cdot\mathbf{p}$ approximation when compared to tight-binding calculations [35]. If there are no new Dirac points introduced by the superlattice, in the limit of $L_y \gg L_x$, with L_y the length, L_x the width and the superlattice axis is in the $\hat{y}$ direction, the electron moves diffusively [35, 37] perpendicular to the superlattice axis. In the $\mathbf{k}\cdot\mathbf{p}$ approximation, this may be interpreted as the introduction of a group velocity anisotropy parameter λ, so that the effective group velocity in $\hat{x}$ direction is $v_x = \lambda v_F$. Thus the low energy Hamiltonian [35, 41, 42, 51] for armchair graphene nanoribbon superlattice in the absence of intravalley and intervalley scattering may be expressed as:

$$H = \hbar v_F \begin{pmatrix} 0 & \lambda k_n - i k_y & 0 & 0 \\ \lambda k_n + i k_y & 0 & 0 & 0 \\ 0 & 0 & 0 & -\lambda k_n - i k_y \\ 0 & 0 & -\lambda k_n + i k_y & 0 \end{pmatrix} \tag{2.23}$$

2.3 Overview of Method

In this Thesis, the THz nonlinear direct interband optical properties of armchair graphene nanoribbons are derived. The interband optical response is obtained by constructing the wavefunction using the Floquet theorem. The Fourier expansion of the wavefunction will leads us to an $N-$photon coupling mechanism under time dependent perturbation theory (TDPT) [52].

With the presence of an external electric field $\mathbf{E}(t) = e^{-i\omega t}\left(\hat{x}E_x + \hat{y}E_y\right)$, in the Coulomb gauge for a constant scalar potential, we have $\mathbf{E}(t) = -\partial_t \mathbf{A}(t)$. If the electric field is switched on adiabatically at $t_0 \to -\infty$, the corresponding magnetic vector potential is written [10, 53, 54]:

$$\mathbf{A}(t) = \frac{\mathbf{E}(t)}{i\omega} = \frac{e^{-i\omega t}}{i\omega}\left(\hat{x}E_x + \hat{y}E_y\right) \tag{2.24}$$

Full details of the derivation of the vector potential can be seen in Appendix A.

Following the general procedure of Ref. [10, 52], due to the Dirac nature of the Hamiltonian $H_0(\mathbf{k})$, with a smooth external external field $U(\mathbf{r})$, the perturbed Hamiltonian may be written as:

$$H(\mathbf{k}) = H_0(\mathbf{k}) + H_{int} = H_0\left(\mathbf{k} + q\mathbf{k}/\hbar\right) + U(\mathbf{r})\sigma_0 \otimes \sigma_0 \tag{2.25}$$

where σ_0 is the 2×2 identity matrix, and $H_{int} = H\left(q\mathbf{k}/\hbar\right)$. Eq. (2.25) implies that the external field $U(\mathbf{r})$ does not couple the $\mathbf{K}$ and $\mathbf{K}'$ valleys, provided that the external field $U(\mathbf{r})$ varies smoothly on the scale of the lattice constant a_0 [36]. According to the Floquet theorem, the solution of the Hamiltonian (2.25), in the absence of the

external electromagnetic field, is of the form [32, 52, 55–58]:

$$\Psi(\mathbf{r}, t; \mathbf{k}) = \sum_{n=0}^{\infty} \phi_n(\mathbf{k}) e^{i2\pi \mathbf{k}\cdot\mathbf{r}} e^{-in\omega t} e^{-i\epsilon t/\hbar} \tag{2.26}$$

with the requirement that when $\mathbf{A} \to 0$, $\Psi(\mathbf{r}, t; \mathbf{k})$ should be a solution of the Hamiltonian H_0 [32, 52, 55–57]. The spinor $\phi_n(\mathbf{k})$ represents the Dirac fermion-photon coupling strength and governs the multiple-photon process in the direct interband transitions [10, 32, 51, 52, 55, 57]. The spinor can be obtained by solving the Schrödinger equation:

$$i\hbar \frac{\partial \Psi(\mathbf{r}, t; \mathbf{k})}{\partial t} = H(\mathbf{k}) \Psi(\mathbf{r}, t; \mathbf{k}) \tag{2.27}$$

The Hamiltonian has $\mathbf{k}$ dependent $\boldsymbol{\sigma} \cdot \mathbf{k}$ off-diagonal terms, which will gives rise to a set of recursive coupled equations, that can be represented in terms of a transfer matrix:

$$\phi_n(\mathbf{k}) = T_n \left(\phi_{n-1}(\mathbf{k}), \mathbf{A} \right) \phi_{n-1}(\mathbf{k}) \tag{2.28}$$

Thus we can solve for $\phi_n(\mathbf{k})$ up to any arbitrary order.

Let us find the local current density conductivity and local current density operators for Dirac fermions. The particle density for a single Dirac fermion density is simply $\rho = |\Psi(\mathbf{r}, t; \mathbf{k})|^2$. Thus the charge density operator is:

$$\rho_{op}(\mathbf{r}) = \delta(\mathbf{r} - \mathbf{r_{op}}) \tag{2.29}$$

After applying the equation of continuity:

$$q \frac{\partial \rho}{\partial t} + \nabla \cdot \mathbf{j} = 0 \tag{2.30}$$

joining with the Schrödinger equation:

$$i\hbar\frac{\partial\Psi(\mathbf{r},t;\mathbf{k})}{\partial t} = H(\mathbf{k})\Psi(\mathbf{r},t;\mathbf{k}) \tag{2.31}$$

we obtain the local (single-particle) current density for Dirac fermions:

$$\mathbf{j}(\mathbf{k},t) = \hat{x}j_x(\mathbf{k},t) + \hat{y}j_y(\mathbf{k},t) \tag{2.32}$$

with the local current density Fourier component defined as:

$$j_\nu(\mathbf{k},t) = q\Psi(\mathbf{r},t;\mathbf{k})^\dagger\frac{\partial H(\mathbf{k})}{\hbar\partial k_\nu}\Psi(\mathbf{r},t;\mathbf{k}) \tag{2.33}$$

where $\nu = x, y$ indicates the component of the induced current.

If we define the group velocity operator $\mathbf{v} = \nabla_k H(\mathbf{k})/\hbar$, we have,

$$\begin{aligned}&\langle\Psi(\mathbf{r},t;\mathbf{k})|\mathbf{v}|\Psi(\mathbf{r},t;\mathbf{k})\rangle \\ &\equiv sv_F\left[\langle\Psi_K(\mathbf{r},t;\mathbf{k})\left|\frac{\mathbf{k}}{|\mathbf{k}|}\right|\Psi_K(\mathbf{r},t;\mathbf{k})\rangle + \langle\Psi_{K'}(\mathbf{r},t;\mathbf{k})\left|\frac{\mathbf{k}'}{|\mathbf{k}|}\right|\Psi_{K'}(\mathbf{r},t;\mathbf{k})\rangle\right]\end{aligned} \tag{2.34}$$

where s represents the state's chirality. Eq. (2.34) indicates that for a given $\mathbf{k}$ state, the group velocity operator $\mathbf{v}$ is parallel to the isospin in the $\mathbf{K}(\mathbf{K}')$ valley. As the chirality in metallic armchair graphene nanoribbons only exists for the metallic lowest bands [37] where $k_n = 0$, so the group velocity and isospin are parallel/antiparallel to $\mathbf{k}$ for the valence/conduction states in metallic armchair graphene nanoribbons only for the lowest bands ($k_n = 0$), respectively [36, 37]. The fact that the isospin of the wavefunciton is tied to the propagation direction has important implications for the transport properties, *e.g.*, the absence of backscattering [36, 37, 59].

Next, we comment on the quantum-relativistic analog of the local current density. In general, the valley degree of freedom corresponds to the opposite sign of the

two subblocks, which have left-handed or right-handed circular polarization [36]. In quasi-1D graphene ribbon structures, due to the block nature of the $\mathbf{k}\cdot\mathbf{p}$ Hamiltonian, the relative sign of the two subblocks can be changed via a unitary transformation, hence a distinction between the left or right handedness of the valley degree freedom cannot be made. Low energy electrons in armchair graphene nanoribbons are called "chiral" because the direction of motion is tied to the direction of the isospin. As the local current operator $\mathbf{j}(\mathbf{k},t)$ is proportional to the expectation value of the group velocity operator $\mathbf{v}$, so low energy electrons moving in the $\hat{x}$ or $\hat{y}$ direction always have an isospin pointing in the $\hat{y}$ direction for metallic armchair graphene nanoribbon. As this isospin is 1D, there is no analog of circular polarization and therefore no left or right handedness in metallic armchair graphene nanoribbons [36].

The local current density $j_\nu(\mathbf{k},t)$ conserves charge current density [54, 60, 61] with an applied vector potential $\mathbf{A}$. The total optical current density component is:

$$\begin{aligned} J_\nu(\mathbf{k},t) &= e\left\langle \Psi(\mathbf{r},t;\mathbf{k})\left|\mathbf{v}\right|\Psi(\mathbf{r},t;\mathbf{k})\right\rangle\cdot\hat{\nu} \\ &= e\sum_{\mathbf{k}}\Psi(\mathbf{r},t;\mathbf{k})^\dagger\frac{\partial H}{\hbar\partial k_\nu}\Psi(\mathbf{r},t;\mathbf{k}) \\ &= e\sum_{\mathbf{k}}\left[\phi_0(\mathbf{k})^\dagger+\phi_1(\mathbf{k})^\dagger+\phi_2(\mathbf{k})^\dagger+\cdots\right]\frac{\partial H}{\hbar\partial k_\nu}\left[\phi_0(\mathbf{k})+\phi_1(\mathbf{k})+\phi_2(\mathbf{k})+\cdots\right] \end{aligned} \tag{2.35}$$

with $\nu = x, y$ indicating current component in the $\hat{\nu}$ direction. Thus the terms $\propto |\mathbf{E}|^n$ represents the n-th order direct interband nonlinear optical response.

CHAPTER 3
FIRST PRINCIPLES STUDY OF THE TERAHERTZ THIRD ORDER NONLINEAR RESPONSE OF METALLIC ARMCHAIR GRAPHENE NANORIBBONS

[1]In this chapter, we compute the terahertz third-order nonlinear conductance of metallic armchair graphene nanoribbons using time-dependent perturbation theory. Significant enhancement of the intrinsic third-order conductance over the result for intrinsic 2D single-layer graphene is observed over a wide range of temperatures. We also investigate the nonlinear response of extrinsic metallic acGNR with $|E_F| \ll 200\,\text{meV}$. We find that the third-order conductance exhibits a strong Fermi level dependence at low temperatures. A third-order critical field strength of between ~ 1 and $5\,\text{kV/m}$ is computed for the Kerr conductance as a function of temperature. For the third-harmonic conductance, the minimum critical field is computed to be $\sim 5\,\text{kV/m}$.

3.1 Introduction

Graphene, a monolayer of carbon atoms arranged in a 2D honeycomb lattice, has excellent electronic, mechanical, thermal and optoelectronic properties. [2] The spectrum of graphene is described by the massless Dirac equation. Due to the many unique properties of graphene, it is considered a promising material for electronic device applications.

In the terahertz (THz) to far-infrared (FIR) spectral regime, the optical con-

[1]This chapter was published in *Phy. Rev. B.* **93**, 235430 (2016) [10].

ductance of graphene based systems has attracted much interest due to the ongoing search for viable THz devices. Graphene is traditionally a poor conductor in the THz to FIR spectrum, with universal conductivity $\sigma_0 = e^2/(4\hbar)$ leading to an absorption of only 2.3% at normal incidence per graphene layer. [62] However, graphene has a number of features that make it an attractive nonlinear system to study. [8, 16–18] These include a tunable Fermi level, and more importantly a linear dispersion relation near the Dirac point. [6,7] This linear dispersion and the accompanying constant Fermi velocity v_F have led to the theoretical prediction of the generation of higher-order harmonics in graphene. [16] Mikhailov and Ziegler have developed a quasi classical kinetic theory and a quantum theory on the third order nonlinear process in graphene. [63,64] Wright *et.al.* [52] adopted a time dependent perturbation theory to analyse the linear and third order nonlinear optical response of intrinsic 2D single layer graphene (2D SLG) with an applied electric field of approximately 100 kV/m, which indicates that the strong nonlinear conductance makes graphene a potential candidate for THz photonic and optoelectronic devices. Ang *et.al.* [32,57] investigated the nonlinear optical conductivity of bilayer graphene (BLG), semihydrogenated graphene (SHG) and Kronig-Penney (KP) graphene superlattices. Gullans *et.al.* [65] studied the single photon nonlinear mechanism in graphene nanostructures and showed strong confinement of plasmons and large intrinsic nonlinearity in graphene nanostructures led to significant electric field enhancement. Recently, Mikhailov *et.al.* [66–68], Cheng *et.al.* [34,69–72] and Morimoto *et.al.* [73] proposed quantum theories of the third-order nonlinear response with an uniform external electric field in 2D SLG independently.

This work [34, 66, 68, 69, 71, 73] studies the relationship of the Fermi energy with the direct interband transition, which confirms the resonant frequencies for the third-harmonic conductance which appeared in Refs. [52, 55], and the missing resonant frequencies for the Kerr conductance in Refs. [52, 55] as we perform the calculations of Refs. [52, 55].

Hendry *et.al.* [17] first report measurement of the coherent nonlinear optical response of single and few-layer graphene using four-wave mixing. Their results experimentally demonstrate that graphene structures exhibits a strong nonlinear optical response in the NIR spectral region. Harmonic generation, frequency mixing, optical rectification, linear and circular photogalvanic effect, photon drag effect, photoconductivity, coherently controlled ballistic charge currents, etc. in graphene are currently the subject of intense research, and have already found a number of applications. [8] Kumar *et.al.* [19] found third harmonic generation in graphene and multi-layer graphite films grown by exfoliation. They found the nonlinear emission frequency matched well with the theoretical prediction and deducted an effective third order susceptibility on the order of $100\,\mu m^2/kV^2$. Maeng *et.al.* [20] measured the nonlinear conductivity of gate controlled graphene grown by CVD. Their work show nonlinear conductance of graphene can be efficient controlled via applied gate voltage and doping. Recently, Hafez *et.al.* [21] reported experimental results on the carrier dynamics in epitaxially grown monolayer graphene [21]. This work demonstrates that the microscopic mechanisms of nonlinear effects in graphene can be quite different from their counterparts in ordinary semiconductor systems [21]. The large

nonlinear response originating from interband transitions is seven orders of magnitude stronger than the nonlinear response observed in dielectric materials without such transitions [17,74]. These theoretical and experimental studies have shown that the linear energy dispersion and high electron Fermi velocity in graphene leads to a strongly nonlinear optical response in the THz to FIR regime for various 2D graphene systems compared with the counterparts in conventional parabolic semiconductor systems.

While the nonlinear optical properties of 2D graphene structures have been studied extensively, the nonlinear optical response, which is proportional to the higher powers of the applied electric field, has been much less studied for graphene nanoribbons (GNR). Duan *et.al.* [9] studied the linear response of intrinsic metallic armchair GNR in the infrared regime with a linearly-polarized applied electric at low temperatures. Sasaki *et.al.* [75] proposed optical interband transition selection rules for acGNR with linearly-polarized electric fields in the transverse and longitudinal directions. Chung *et.al.* [76] also investigated the interband selection rules for acGNR. All of this work focused on the linear response of GNR and did not address the nonlinear response of acGNR at THz frequencies for an applied linearly-polarized electric field in the longitudinal and transverse directions.

Wang *et.al.* [22] find that thin GNRs (sub-20 nm) with smooth edges can be treated as quasi 1D quantum wires, not dominated by defects. In general, new physics (quantization of energy, momentum *etc.*) emerges when the dimensionality of 2D graphene is reduced to a quasi 1D quantum wire. With the rapid development of

techniques for the synthesis of thin GNRs [22, 48, 49], thin GNRs (sub-20 nm) may have ultra smooth edges, higher mobility and longer carrier mean free path than expected theoretically. Depending on the nature of the edges, there are two types of GNR: armchair graphene nanoribbons (acGNR) and the zigzag graphene nanoribbon (zzGNR). Electron dynamics of both acGNR and zzGNR have distinct properties, due to their geometry and boundary conditions. [41, 42] Metallic acGNR exhibits a linear band structure in both tight-binding [39, 40] and $\mathbf{k} \cdot \mathbf{p}$ models. Edge states contribute significantly to GNR properties, since in a nanoscale GNR, massless Dirac fermions can reach the ribbon edge within a few femtoseconds before encountering any other scattering and screening effects, such as electron-electron and electron-phonon interactions, the Peierls instability, *etc.* In general, the nonlinearity of GNR originates from the redistribution of the Dirac fermions in momentum and energy space induced by the applied electric field [8]. As a consequence, conductivity components oscillating in time and space, as well as spatially homogeneous steady state components are expected to be obtained from the resulting nonequilibrium distribution. Thus the resulting nonlinear response is sensitive to the applied field strength and polarization [8]. Therefore, it is important to study the electrodynamics for higher order harmonic generation with the existence of an applied electric field in GNR. In light of recent reports of the growth of ultra thin acGNR (sub-10 nm) reported by Kimouche *et.al.* [48] and Jacobberger *et.al.* [49], and the fact that Kimouche *et.al.* [48] show that defects (kinks) do not strongly modify the electronic structure of ultrathin acGNR, the study of the nonlinear response of these metallic acGNR is of particular significance

today.

In this chapter, we develop a semi-analytic approach based on the $\mathbf{k} \cdot \mathbf{p}$ approximation in the Coulomb gauge to calculate the nonlinear THz response of thin acGNR (width $< 20\,\text{nm}$) under a moderate applied linearly-polarized electric field in the longitudinal and transverse directions. We use time dependent perturbation theory to do a Fourier analysis of the wavefunction in the presence of a strong linearly-polarized time-harmonic electric field, and obtain the linear and third-order optical THz response of thin metallic acGNR.

The chapter is organized as follows. In Section 3.2, we begin with the $\mathbf{k} \cdot \mathbf{p}$ approximation to obtain the time-independent wavefunction and the interaction Hamiltonian with an applied electric field for acGNR, and we present a brief derivation of our semi-analytical approach to calculate the nonlinear conductance. In Section 3.3, we apply our model to calculate the nonlinear conductance of metallic acGNR. In particular, we compare the nonlinear properties of single layer metallic acGNR with those of intrinsic 2D SLG. We also propose a correction to previous work [52, 55] on the third order Kerr conductance in intrinsic 2D SLG. We analyze the third-order nonlinear terms using standard definitions for these quantities: Kerr conductance for the third-order terms oscillating at frequency ω and third-harmonic conductance for the terms oscillating at frequency 3ω, determine the required applied electric field strength to induce non-negligible nonlinear effects and investigate the temperature and Fermi level dependence of the nonlinear conductance. Following this, a brief analysis of the selection rules for nonlinear THz direct interband transitions in metallic

thin acGNR is discussed. Finally, the conclusions are presented in Section 3.5.

3.2 Model

3.2.1 H_0, ψ_0 and the applied field E_μ

Graphene is a 2D hexagonal lattice (honeycomb) structure of covalently bonded carbon atoms. As there are 2 atoms per unit cell, we label them A and B respectively. At low energies, graphene carriers can be described by the massless Dirac equation. As a consequence, graphene shows a linear energy band structure near the Dirac points $\mathbf{K} = \frac{2\pi}{a_0}\left(\frac{1}{3}, \frac{1}{\sqrt{3}}\right)$ and $\mathbf{K'} = \frac{2\pi}{a_0}\left(\text{-}\frac{1}{3}, \frac{1}{\sqrt{3}}\right)$ of the Brillouin zone. Here a_0 is the triangular lattice parameter of the graphene structure. [41, 42] ($a_0 = \sqrt{3}a_{cc}$ where a_{cc} is the carbon-carbon separation distance in acGNR and $a_{cc} = 1.42\,\text{Å}$).

The unperturbed $\mathbf{k}\cdot\mathbf{p}$ Hamiltonian for graphene can be written in terms of Pauli matrices as $H_{0,K} = \hbar v_F \boldsymbol{\sigma}\cdot\mathbf{k}$ for the $\mathbf{K}$ valley and $H_{0,K'} = \hbar v_F \boldsymbol{\sigma}\cdot\mathbf{k'}$ for the $\mathbf{K'}$ valley with $\mathbf{k}(\mathbf{k'})$ the perturbation from the center of the $\mathbf{K}(\mathbf{K'})$ valley. The corresponding wavefunctions are expressed as envelope functions $\psi_K(\mathbf{r}) = [\psi_A(\mathbf{r}), \psi_B(\mathbf{r})]$ and $\psi_{K'}(\mathbf{r}) = [\psi'_A(\mathbf{r}), \psi'_B(\mathbf{r})]$ for states near the $\mathbf{K}$ and $\mathbf{K'}$ points, respectively.

Following the development in [41, 42], the time-independent (unperturbed) Hamiltonian for a single Dirac fermion in GNR can be written as:

$$\begin{aligned} H_0 &= \begin{pmatrix} H_{0,K} & 0 \\ 0 & H_{0,K'} \end{pmatrix} \\ &= \hbar v_F \begin{pmatrix} 0 & k_x - ik_y & 0 & 0 \\ k_x + ik_y & 0 & 0 & 0 \\ 0 & 0 & 0 & -k_x - ik_y \\ 0 & 0 & -k_x + ik_y & 0 \end{pmatrix} \end{aligned} \tag{3.1}$$

with wave envelope functions in the case of acGNR:

$$\psi_{n,s}(\mathbf{r},0) = \begin{pmatrix} \psi_{n,s}(\mathbf{r})_K \\ \psi_{n,s}(\mathbf{r})_{K'} \end{pmatrix} = \frac{e^{ik_y y}}{2\sqrt{L_x L_y}} \begin{pmatrix} e^{-i\theta_{k_n,k_y}} e^{ik_n x} \\ s e^{ik_n x} \\ -e^{-i\theta_{k_n,k_y}} e^{-ik_n x} \\ s e^{-ik_n x} \end{pmatrix} \tag{3.2}$$

with L_x the width of acGNR in the x (zigzag) direction, L_y the length of the acGNR in the y (armchair) direction and the direction of the isospin of the state is $\theta_{k_n,k_y} = \tan^{-1}(k_n/k_y)$.

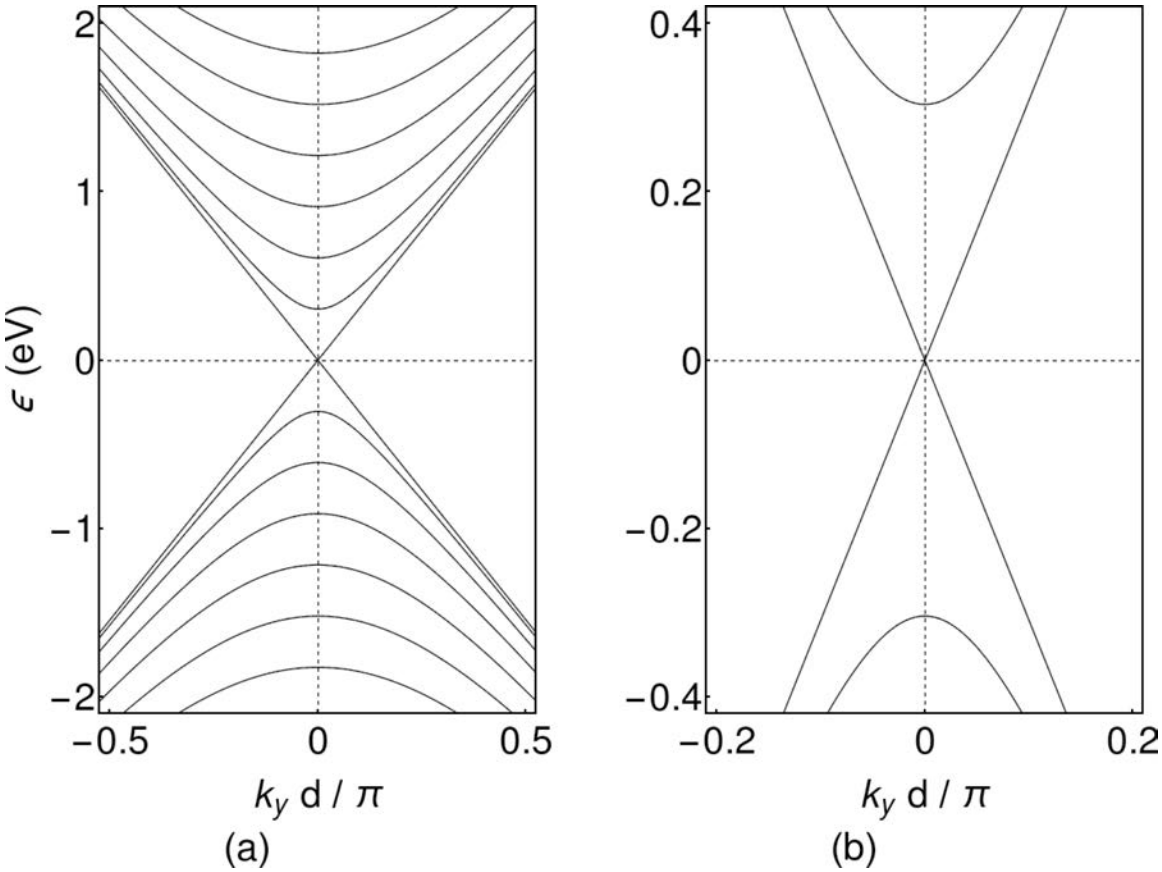

Figure 3.1: $\mathbf{k}\cdot\mathbf{p}$ band structure of infinitely long metallic acGNR of width $L_x = 24.6$Å (acGNR20) and $L_y \to \infty$. (a) illustrates the seven lowest-energy bands, and (b) illustrates the gap of $\sim 608\,\text{meV}$ between $n = 1$ conduction and valence band. Here d is the width of the acGNR unit cell ($d = (1+\sqrt{3})a_{cc}$).

The electronic properties of acGNR depend strongly on their width L_x. The width of acGNR can be calculated using $L_x = \frac{N}{2}a_0$, where N is the number of atoms along the zigzag edge ($\hat{x}$ direction). In general, acGNR of $N = 3M - 1$ atoms wide along the zigzag edge, with M odd, are metallic, whereas all the other cases are semiconductors [41, 42]. In Fig. 3.1 we plot the band structure of infinitely long metallic ($L_y \to \infty$) acGNR for $N = 20$ (acGNR20). One can see that in Fig. 3.1 there is a Dirac point, leading to metallic behavior for a single-electron model. Thus for a width of the form $L_x = \frac{3M-1}{2}a_0$ with M odd, the allowed values of $k_n = \frac{2\pi}{3a_0}\frac{M+n}{M}$ create doubly-degenerate states for $n \neq -M$ and when $k_y \to 0$, the existence of a zero energy state indicates that the conduction and valence band touch at the Dirac points. The non-metallic bands in Fig. 3.1 are well above THz energies, and as a result, a THz direct interband transition can only occur between metallic subbands ($k_n = 0$) for thin metallic acGNR.

Because thin acGNR (sub-20 nm) can be treated as a quasi-1D quantum wire system [22], we have Bloch states where $k_{x,n} = \frac{2\pi}{3a_0}\frac{M+n}{M}$ and $k_{y,m} = \frac{2\pi}{L_y}m$. In metallic acGNR when $n = -M$, we can write the time-independent wave envelope function for one Dirac fermion in the lowest subband near the Dirac point, with $k_{x,n} = 0$ as:

$$\psi(\mathbf{r}, 0; m) = \phi_0(m)e^{i2\pi my/L_y} \tag{3.3}$$

where $\phi_0(m)$ is found to be:

$$\phi_0(m) = \begin{bmatrix}\phi_{K,0}(m)\\ \phi_{K',0}(m)\end{bmatrix} = \frac{1}{2\sqrt{L_xL_y}}\begin{bmatrix}\mathrm{sgn}(k_y)\\ s\\ -\mathrm{sgn}(k_y)\\ s\end{bmatrix} \tag{3.4}$$

constructed from Eq. (3.2).

Let us consider metallic acGNR under an applied linearly-polarized electric field $\mathbf{E} = \hat{\mu} E_\mu e^{-i\omega t}$, of frequency ω with normal incidence. Notice that the time dependent part of the applied field $e^{-i\omega t}$ corresponds to the absorption process and $e^{i\omega t}$ corresponds to the emission process. For time-harmonic fields that turn on adiabatically [53,54] at $t \to -\infty$ and constant scalar potential $\nabla\varphi = 0$, in the Coulomb gauge [53] ($\nabla \cdot \mathbf{A} = 0$) the vector potential [52,53,55] is of the form $\mathbf{A} = \hat{\mu} E_\mu \exp(-i\omega t)/(i\omega)$ (see Appendix A for a brief discussion). The interaction with the vector potential is described by writing the canonical momentum $\mathbf{k} \to \mathbf{k} + \frac{q\mathbf{A}}{\hbar}$, where q is the elementary charge. In other words, the total Hamiltonian for graphene in the presence of a normally-incident electromagnetic field can be written as $H_K = \hbar v_F \boldsymbol{\sigma} \cdot (\mathbf{k} + \frac{q\mathbf{A}}{\hbar})$ for the $\mathbf{K}$ point and $H_{K'} = \hbar v_F \boldsymbol{\sigma} \cdot (\mathbf{k}' + \frac{q\mathbf{A}}{\hbar})$ for the $\mathbf{K}'$ point. The total Hamiltonian for acGNR can be expressed as: $H = H_0 + H_{int}$, where the interaction part of the Hamiltonian is given by:

$$H_{int} = \begin{pmatrix} H_{int,K} & 0 \\ 0 & H_{int,K'} \end{pmatrix} \tag{3.5}$$

with $H_{int,K(K')} = \frac{q v_F}{i\omega} \boldsymbol{\sigma} \cdot \mathbf{E_0} e^{-i\omega t}$ where $\boldsymbol{\sigma} = \hat{x}\sigma_x + \hat{y}\sigma_y$ is the Pauli matrix and $\mu = x, y$ indicates the direction of the applied linearly-polarized electric field.

3.2.2 Local conductivity and conductance

In this work, we follow Refs. [32, 34, 52, 54, 55, 57, 68, 69, 71, 73, 77] and make the relaxation-free approximation, neglecting carrier-phonon and carrier-carrier [78] scattering, defect scattering, and many body effects in our calculation. Acoustic phonon scattering may be neglected because the interaction is not phasematched due

to the large (three orders of magnitude) difference between the carrier Fermi velocity v_F and the acoustic velocity. The optical phonon energy in graphene is $\sim 200\,\text{meV}$ and so for low-energy carriers of the order of a few tens of meV and below, optical phonon scattering may be neglected as well. Carrier-carrier scattering increases with the square of the carrier density. Since our model considers extrinsic metallic acGNR with Fermi energies of the order of a few meV and small excitation field strengths ($\sim 10\,\text{kV/m}$), carrier-carrier scattering and many-body effects may be neglected to a good approximation. Ultrathin metallic acGNR with smooth edges have recently been fabricated showing ballistic transport due to the low defect density [48], and so it is appropriate to neglect defect scattering. Due to the block nature of the total Hamiltonian $H = H_0 + H_{int}$ in the $\mathbf{k}\cdot\mathbf{p}$ approximation, we also neglect intravalley and intervalley scattering in thin metallic acGNRs as well. Thus, the theory presented in this chapter applies to low-energy (THz) carriers in thin, smooth metallic acGNR where the higher index bands ($k_{x,n} \neq 0$) are well-separated from the lowest-order linear bands (see Fig. 3.1).

In metallic acGNR, we describe the Dirac fermion under the influence of an applied electric field $\hat{\mu}E_\mu e^{-i\omega t}$ for the metallic band ($k_{x,n} = 0$) as an envelope wavefunction $\psi_\mu(\mathbf{r}, t; m) = [\psi_\mu(\mathbf{r}, t; m)_K, \psi_\mu(\mathbf{r}, t; m)_{K'}]^T$. Using the Floquet theorem, the Fourier series expansion of $\psi_\mu(\mathbf{r}, t; m)$ can be written [32, 52, 55–58] as:

$$\psi_\mu(\mathbf{r}, t; m) = \sum_{l=0}^{\infty} \phi_\mu(m, l) e^{i2\pi m y/L_y} e^{-i\omega l t} e^{-i\epsilon t/\hbar} \tag{3.6}$$

with the initial condition $\phi_\mu(m, 0) = \phi_0(m)$, which satisfies the requirement that when $\mathbf{A} \to 0$, $\psi_\mu(\mathbf{r}, t; m)$ should be a solution of the Hamiltonian without an applied

field [32, 52, 55–57]. The spinor $\phi_\mu(m,l)$ is given by:

$$\phi_\mu(m,l) = \begin{bmatrix} \phi_\mu(m,l)_K \\ \phi_\mu(m,l)_{K'} \end{bmatrix} = \begin{bmatrix} a_l(m) \\ b_l(m) \\ c_l(m) \\ d_l(m) \end{bmatrix} \tag{3.7}$$

We can then calculate the charge density as: $\rho = |\psi_\mu(\mathbf{r},t;m)|^2$, where the particle density operator is $\rho_{op}(\mathbf{r}) = \delta(\mathbf{r} - \mathbf{r_{op}})$. After applying the continuity equation $q\frac{\partial \rho}{\partial t} + \nabla \cdot \mathbf{j} = 0$, along with the Schrödinger equation $H\psi_\mu(\mathbf{r},t;m) = i\hbar\frac{\partial \psi_\mu(\mathbf{r},t;m)}{\partial t}$ under the Coulomb gauge, we obtain the local (single-particle) current density for Dirac fermions in the metallic sub-band of acGNR:

$$\mathbf{j}(m,t) = \hat{x} j_x(m,t) + \hat{y} j_y(m,t) \tag{3.8}$$

with the local current density component defined as:

$$j_\nu(m,t) = q\psi_\mu(\mathbf{r},t;m)^\dagger \frac{\partial H}{\hbar \partial k_\nu} \psi_\mu(\mathbf{r},t;m) \tag{3.9}$$

where $\mu = x, y$ indicates the direction of the polarization of the applied electric field, and $\nu = x, y$ indicates the component of the induced current.

After substituting Eq. (3.6) into Eq. (3.9), the Fourier series expansion of the local current density becomes:

$$
\begin{aligned}
j_\nu(m,t) =& q\left[\phi_\mu(m,0)+\phi_\mu(m,1)e^{-i\omega t}+\phi_\mu(m,2)e^{-i2\omega t}+\cdots\right]^\dagger \\
&\times\frac{\partial H}{\hbar\partial k_\nu}\left[\phi_\mu(m,0)+\phi_\mu(m,1)e^{-i\omega t}+\phi_\mu(m,2)e^{-i2\omega t}+\cdots\right] \\
=& q\left\{\left[\phi_\mu^\dagger(m,0)\frac{\partial H}{\hbar\partial k_\nu}\phi_\mu(m,0)+\phi_\mu^\dagger(m,1)\frac{\partial H}{\hbar\partial k_\nu}\phi_\mu(m,1)+\cdots\right]\right. \\
&+e^{-i\omega t}\left[\phi_\mu^\dagger(m,0)\frac{\partial H}{\hbar\partial k_\nu}\phi_\mu(m,1)+\phi_\mu^\dagger(m,1)\frac{\partial H}{\hbar\partial k_\nu}\phi_\mu(m,2)+\cdots\right] \\
&+e^{+i\omega t}\left[\phi_\mu^\dagger(m,1)\frac{\partial H}{\hbar\partial k_\nu}\phi_\mu(m,0)+\phi_\mu^\dagger(m,2)\frac{\partial H}{\hbar\partial k_\nu}\phi_\mu(m,1)+\cdots\right] \\
&+e^{-i2\omega t}\left[\phi_\mu^\dagger(m,0)\frac{\partial H}{\hbar\partial k_\nu}\phi_\mu(m,2)+\phi_\mu^\dagger(m,1)\frac{\partial H}{\hbar\partial k_\nu}\phi_\mu(m,3)+\cdots\right] \\
&+e^{+i2\omega t}\left[\phi_\mu^\dagger(m,2)\frac{\partial H}{\hbar\partial k_\nu}\phi_\mu(m,0)+\phi_\mu^\dagger(m,3)\frac{\partial H}{\hbar\partial k_\nu}\phi_\mu(m,1)+\cdots\right] \\
&+e^{-i3\omega t}\left[\phi_\mu^\dagger(m,0)\frac{\partial H}{\hbar\partial k_\nu}\phi_\mu(m,3)+\cdots\right] \\
&\left.+\ e^{+i3\omega t}\left[\phi_\mu^\dagger(m,3)\frac{\partial H}{\hbar\partial k_\nu}\phi_\mu(m,0)+\cdots\right]+\cdots\right\}
\end{aligned}
\tag{3.10}
$$

In general, for the study of third-order nonlinear optical processes induced by an arbitrary superposition of three time-harmonic electric fields, it is customary to write the local current density due to an individual atom as the product of a fourth-rank conductivity tensor with the three arbitrary applied fields. In the current work, we consider a much simpler case. The applied electric field is linearly-polarized along the longitudinal armchair (transverse zigzag) or $\hat{y}$ ($\hat{x}$) direction and has a single frequency ω. As a result, the expression for the local current density can be written [68]:

$$
\begin{aligned}
j_\nu(m,t) = \big[& e^{-i\omega t}\tilde{\sigma}^{(1)}_{\mu\nu}(\omega)E_\mu + \{e^{-i\omega t}\tilde{\sigma}^{(3)}_{\nu\mu\mu\mu}(-\omega,\omega,\omega)E^3_\mu \\
& + e^{-i\omega t}\tilde{\sigma}^{(3)}_{\nu\mu\mu\mu}(\omega,-\omega,\omega)E^3_\mu + e^{-i\omega t}\tilde{\sigma}^{(3)}_{\nu\mu\mu\mu}(\omega,\omega,-\omega)E^3_\mu\} \\
& + e^{-i3\omega t}\tilde{\sigma}^{(3)}_{\nu\mu\mu\mu}(\omega,\omega,\omega)E^3_\mu + \cdots \big] + c.c. \\
= \big[& j^{(1)}_\nu(m,\omega,t) + j^{(3)}_\nu(m,\omega,t) + j^{(3)}_\nu(m,3\omega,t) + \ldots \big] + c.c.
\end{aligned}
\tag{3.11}
$$

By matching term-by-term the expansions in Eqs. (3.10) and (3.11) , we can obtain the individual non-zero elements in the local third-order conductivity tensor. Further, by rewriting Eq. (3.11), we see that the expressions for the Fourier components of the local current density reduce to terms involving a local 2×2 conductivity matrix and the applied electric field [32, 52, 55, 57]:

$$
j^{(i)}_\nu(m,\omega_0) = \sigma^{(i)}_{\mu\nu}(m,\omega_0)E_\mu e^{-i\omega_0 t} \tag{3.12}
$$

where for $i = 1$, $\omega_0 = \omega$; and for $i = 3$, $\omega_0 = \omega$ ($\omega_0 = 3\omega$) for the Kerr (third-harmonic) terms in the local current density expansion, and where $\sigma^{(i)}_{\mu\nu}(m,\omega_0)$ is the local ith-order conductivity matrix defined as for 2D SLG in Refs. [32, 52, 55, 56, 56–58, 74, 79]

To compute the *total* current density, we sum over all possible states, using the thermal distribution $N(\epsilon, E_F) = n_F(-|\epsilon|, E_F) - n_F(|\epsilon|, E_F)$ where $|\epsilon| = |m|hv_F/L_y$. The total current density [32, 52, 55, 56, 56–58, 74, 79] is therefore:

$$
J_\nu(t) = g_s\, g_v \sum_m j_\nu(m,t)N(\epsilon, E_F) \tag{3.13}
$$

with g_s, $g_v = 2$ the spin and valley degeneracies respectively. Here the initial occupancy of the system is described by the Fermi function $n_F(\epsilon, E_F)$. Conduction band states are occupied with probability $n_F(|\epsilon|, E_F)$ and valence band states are occupied

with probability $n_F(-|\epsilon|, E_F)$. The Brey-Fertig wavefunction of Eqs. (3.3) and (3.4) is normalized over the entire sample [41,42], implying that the states at k_y for each valley are occupied with probability 1/2 (assumes N carriers per unit cell). Since there are $2N$ carriers per unit cell, we multiply by $g_v = 2$ to include the contribution to the total current from all $2N$ carriers. As the local current density $j_\nu(m,t)$ conserves charge current density [54, 60, 61] with an applied vector potential $\mathbf{A}$ and the symmetry of graphene, it is straightforward to expand the total current component $J_\nu(t)$ as Fourier series of odd higher-harmonics [16, 17, 32, 34, 52, 55–57, 63, 64, 66, 68, 69, 71]. Again, following Refs. [68], we write the total current density as:

$$\begin{aligned} J_\nu(t) &= \big[e^{-i\omega t}\sigma^{(1)}_{\mu\nu}(\omega)E_\mu + \{e^{-i\omega t}\sigma^{(3)}_{\nu\mu\mu\mu}(-\omega,\omega,\omega)E^3_\mu + e^{-i\omega t}\sigma^{(3)}_{\nu\mu\mu\mu}(\omega,-\omega,\omega)E^3_\mu \\ &\quad + e^{-i\omega t}\sigma^{(3)}_{\nu\mu\mu\mu}(\omega,\omega,-\omega)E^3_\mu\} + e^{-i3\omega t}\sigma^{(3)}_{\nu\mu\mu\mu}(\omega,\omega,\omega)E^3_\mu + \cdots\big] + c.c. \\ &= \big[J^{(1)}_\nu(\omega,t) + J^{(3)}_\nu(\omega,t) + J^{(3)}_\nu(3\omega,t) + \cdots\big] + c.c \end{aligned} \tag{3.14}$$

Adopting the notation in Refs. [32, 52, 55, 57, 75], we define the ith-order conductance component [32, 52, 55, 57] as a 2×2 conductance matrix relating the total nonlinear current density and the applied linearly-polarized electric field:

$$J^{(i)}_\nu(\omega_0,t) = g^{(i)}_{\mu\nu}(\omega_0)E_\mu e^{-i\omega_0 t} \tag{3.15}$$

For the metallic band in thin acGNR, with an applied a $\hat{y}$-polarized electric field $\hat{y}E_y e^{-i\omega t}$, the Hamiltonian H for $k_y = 2\pi m/L_y$ can be written as:

$$H = H_0 + H_{int}$$

$$= \hbar v_F \begin{bmatrix} 0 & -i(k_y + \frac{eE_y e^{-i\omega t}}{i\hbar\omega}) & 0 & 0 \\ +i(k_y + \frac{eE_y e^{-i\omega t}}{i\hbar\omega}) & 0 & 0 & 0 \\ 0 & 0 & 0 & -i(k_y + \frac{eE_y e^{-i\omega t}}{i\hbar\omega}) \\ 0 & 0 & +i(k_y + \frac{eE_y e^{-i\omega t}}{i\hbar\omega}) & 0 \end{bmatrix} \tag{3.16}$$

We then proceed to solve the Schrödinger equation $H\psi_\mu(\mathbf{r}, t; m) = i\hbar\frac{\partial}{\partial t}\psi_\mu(\mathbf{r}, t; m)$. Due to the orthogonal properties of the basis sets $\{e^{-il\omega t}\}$, we obtain the following recursion relations for the spinor components:

$$(\epsilon + n\hbar\omega)a_l(m) = \hbar(-ik_y)b_l(m) - \frac{ev_F E_y}{\omega}b_{l-1}(m) \tag{3.17a}$$

$$(\epsilon + n\hbar\omega)b_l(m) = \hbar(+ik_y)a_l(m) + \frac{ev_F E_y}{\omega}a_{l-1}(m) \tag{3.17b}$$

$$(\epsilon + n\hbar\omega)c_l(m) = \hbar(-ik_y)d_l(m) - \frac{ev_F E_y}{\omega}d_{l-1}(m) \tag{3.17c}$$

$$(\epsilon + n\hbar\omega)d_l(m) = \hbar(+ik_y)c_l(m) + \frac{ev_F E_y}{\omega}c_{l-1}(m) \tag{3.17d}$$

For the lowest band in metallic acGNR, the energy of the carriers in the absence of an applied electric field is $-\hbar v_F|k_y|$. Following this procedure, we arrive at the following local current density terms defined in Eq. (3.12):

$$j_y^{(1)}(m,\omega) = qv_F\left[i\left(a_1(m)b_0^\dagger(m) - a_0^\dagger(m)b_1(m)\right) + i\left(c_1(m)d_0^\dagger(m) - c_0^\dagger(m)d_1(m)\right)\right] \tag{3.18a}$$

$$j_y^{(3)}(m,\omega) = qv_F\left[i\left(a_2(m)b_1^\dagger(m) - a_1^\dagger(m)b_2(m)\right) + i\left(c_2(m)d_1^\dagger(m) - c_1^\dagger(m)d_2(m)\right)\right] \tag{3.18b}$$

$$j_y^{(3)}(m,3\omega) = qv_F\left[i\left(a_3(m)b_0^\dagger(m) - a_0^\dagger(m)b_3(m)\right) + i\left(c_3(m)d_0^\dagger(m) - c_0^\dagger(m)d_3(m)\right)\right] \tag{3.18c}$$

$$j_x^{(1)}(m,\omega) = qv_F\left[\Big(a_1(m)b_0^\dagger(m) + a_0^\dagger(m)b_1(m)\Big) - \Big(c_1(m)d_0^\dagger(m) + c_0^\dagger(m)d_1(m)\Big)\right] \tag{3.18d}$$

$$j_x^{(3)}(m,\omega) = qv_F\left[\Big(a_2(m)b_1^\dagger(m) + a_1^\dagger(m)b_2(m)\Big) - \Big(c_2(m)d_1^\dagger(m) + c_1^\dagger(m)d_2(m)\Big)\right] \tag{3.18e}$$

$$j_x^{(3)}(m,3\omega) = qv_F\left[\Big(a_3(m)b_0^\dagger(m) + a_0^\dagger(m)b_3(m)\Big) - \Big(c_3(m)d_0^\dagger(m) + c_0^\dagger(m)d_3(m)\Big)\right] \tag{3.18f}$$

We make the relaxation-free approximation, neglecting all scattering effects as discussed above. We introduce an infinitesimal broadening factor [34,52,54,68,69,71,73,77] Γ, by making the substitution $\omega = \omega + i\Gamma$ in the $\phi_\mu(m,l)$ spinor. The ith-order local nonlinear conductivity $\sigma_{\mu\nu}^{(i)}(m,\omega_0)$ is then obtained from Eq. (3.12) and summing over all states, with the Fermi energy E_F, $k_y = 2\pi m/L_y$ and $\omega_y = v_F k_y$, we obtain the nonlinear conductance as:

$$\begin{aligned} g_{\mu\nu}^{(i)}(\omega_0) &= \lim_{\Gamma\to 0} g_s g_v \sum_{m=-\infty}^{\infty} \sigma_{\mu\nu}^{(i)}(m,\omega_0) N(\omega_y, E_F) \\ &= \lim_{\Gamma\to 0} g_s g_v \frac{L_y}{2\pi} \int_{-\infty}^{\infty} dk_y\, \sigma_{\mu\nu}^{(i)}(m,\omega_0) N(\omega_y, E_F) \end{aligned} \tag{3.19}$$

where the thermal factor in Eq. (3.19) is:

$$N(\omega_y, E_F) = n_F(-\hbar|\omega_y|, E_F) - n_F(\hbar|\omega_y|, E_F) = \frac{\sinh[\hbar|\omega_y|/(k_B T)]}{\cosh[E_F/(k_B T)] + \cosh[\hbar|\omega_y|/(k_B T)]} \tag{3.20}$$

3.3 Results and Discussion

In what follows, we summarize the characteristics of the nonlinear conductance for all combinations of applied field polarization and current direction.

3.3.1 E_x

If the applied electric field **E** is linearly polarized along the transverse direction of the acGNR ($\hat{x}$ direction), for the metallic band where $k_{x,n} = 0$, a net zero local current density for the $j_x(m,t)$ and $j_y(m,t)$ components is obtained. This result implies there is neither linear nor third-order nonlinear current in metallic acGNR when an electric field polarized transverse to the longitudinal direction of the acGNR is applied.

3.3.2 E_y

For the case where the applied electric field **E** is linearly polarized along the longitudinal direction of the acGNR ($\hat{y}$ direction), for metallic band where $k_{x,n} = 0$, we arrive at the following expressions for the isotropic nonlinear conductance:

$$\begin{aligned} g_{yy}^{(1)}(\omega) &= g_0 \frac{g_s g_v v_F}{\omega L_x} \left[-N(\frac{\omega}{2}, E_F) \right] \\ g_{yy}^{(3)}(\omega) &= g_0 \frac{e^2 E_y^2 v_F^2}{\hbar^2 \omega^4} \frac{g_s g_v v_F}{\omega L_x} \left[-2N(\frac{\omega}{2}, E_F) - N(\omega, E_F) \right] \\ g_{yy}^{(3)}(3\omega) &= g_0 \frac{e^2 E_y^2 v_F^2}{\hbar^2 \omega^4} \frac{g_s g_v v_F}{\omega L_x} \left[\frac{1}{2} N(\frac{\omega}{2}, E_F) - N(\omega, E_F) + \frac{1}{2} N(\frac{3\omega}{2}, E_F) \right] \end{aligned} \tag{3.21}$$

and the anisotropic nonlinear conductance:

$$\begin{aligned} g_{yx}^{(1)}(\omega) &= g_0 \frac{g_s g_v v_F}{\omega L_x} \left[N(\frac{\omega}{2}, E_F) \right] \\ g_{yx}^{(3)}(\omega) &= g_0 \frac{e^2 E_y^2 v_F^2}{\hbar^2 \omega^4} \frac{g_s g_v v_F}{\omega L_x} \left[N(\omega, E_F) \right] \\ g_{yx}^{(3)}(3\omega) &= g_0 \frac{e^2 E_y^2 v_F^2}{\hbar^2 \omega^4} \frac{g_s g_v v_F}{\omega L_x} \left[-\frac{1}{2} N(\frac{\omega}{2}, E_F) + N(\omega, E_F) - \frac{1}{2} N(\frac{3\omega}{2}, E_F) \right] \end{aligned} \tag{3.22}$$

with the $N(\omega)$ defined in Eq. (3.20), and the quantum conductance $g_0 = \frac{e^2}{4\hbar}$. Due to the inversion symmetry inherent in acGNR, the *2*nd-order current makes no contribution to the total current.

In the discussion below, we compare our results for the nonlinear conductance of metallic acGNR with those reported by Wright, *et.al.* [52] and Ang *et.al.* [55] for intrinsic 2D SLG. In Eq. 70 of Ang *et.al.* [55], they write the expression for the third-order Kerr conductance as:

$$g^{(3)}(\omega)_{2D} = -g_0 \frac{e^2 E_0^2 v_F^2}{\hbar^2 \omega^4} \left[2 \tanh \left(\frac{\hbar\omega}{2k_B T} \right) \right] \tag{3.23}$$

We believe this expression omits an additional required term due to the resonance at $\epsilon = \hbar\omega/2$. The correct expression for the third-order Kerr conductance is:

$$g^{(3)}(\omega)_{2D} = -g_0 \frac{e^2 E_0^2 v_F^2}{\hbar^2 \omega^4} \left[\frac{5}{4} N \left(\frac{\omega}{2}, E_F \right) + 2N(\omega, E_F) \right] \tag{3.24}$$

Notice that for intrinsic 2D SLG ($E_F = 0$), $N(\omega, 0) = \tanh\left[\hbar|\omega|/(2k_B T)\right]$, and we recover the thermal factor used in Refs. [52,55]. The missing $\frac{5}{4}N(\frac{\omega}{2})$ term in Eq. (3.23) is the missing contribution for $|\epsilon| = \hbar\omega/2$. As both $\epsilon = \pm\hbar\omega/2$ and $\epsilon = \pm\hbar\omega$ contribute to the generation of the third-order Kerr current [68, 69, 71], we believe that Eq. (3.24) is correct. At $T = 0\,\mathrm{K}$, the real part of the Kerr conductance has two threshold frequencies, $\omega = \pm 2E_F/\hbar$ and $\omega = \pm E_F/\hbar$, corresponding to the contribution for states with energies $\epsilon = \pm\hbar\omega/2$ and $\pm\epsilon = \hbar\omega$, or the resonant transitions for which the Fermi level gap $2|E_F/\hbar|$ matches the one photon and two photon frequencies respectively [69, 71]. We note that the zero temperature result of Refs. [34, 66, 68, 69, 71, 73] contain the same threshold frequencies. As a result, the N-photon coupling approach we have adopted [52, 55] here and the quantum theories of the third-order nonlinear response [34,66,68,69,71,73] show qualitative agreement. The position of the peaks shown in the plots of Refs [34, 68, 69, 71] in the absence

of broadening are at the threshold frequencies with respect to $E_F/\hbar$ derived from Eq. (3.24) at $T = 0\,\mathrm{K}$. Therefore, we compute $g^{(3)}(\omega)$ for 2D SLG using Eq. (3.24) in what follows.

In Eq. (71) of Ang *et.al.* [55], they write the expression for the third-order third-harmonic conductance as:

$$g^{(3)}(3\omega)_{2D} = g_0 \frac{e^2 E_0^2 v_F^2}{\hbar^2 \omega^4} \left[\frac{13}{48} \tanh(\frac{\hbar\omega}{4k_B T}) - \frac{2}{3} \tanh(\frac{\hbar\omega}{2k_B T}) + \frac{45}{48} \tanh(\frac{3\hbar\omega}{4k_B T}) \right] \tag{3.25}$$

Our analysis of the problem gives the same set of coefficients as Eq. (3.25), to wit:

$$g^{(3)}(3\omega)_{2D} = g_0 \frac{e^2 E_0^2 v_F^2}{\hbar^2 \omega^4} \left[\frac{13}{48} N(\frac{\omega}{2}, E_F) - \frac{2}{3} N(\omega, E_F) + \frac{45}{48} N(\frac{3\omega}{2}, E_F) \right] \tag{3.26}$$

For intrinsic 2D SLG ($E_F = 0$), $N(\omega, 0) = \tanh\left[\hbar|\omega|/(2k_B T)\right]$, and therefore Eq. (3.26) reduces to Eq. (3.25) used in Refs. [52, 55]. As a result, we compute $g^{(3)}(3\omega)$ for intrinsic 2D SLG using Eq. (3.26) in what follows. The three threshold frequencies in Eq. (3.26) are the same as those obtained by Morimoto *et.al.* [73]. At $T = 0\,\mathrm{K}$, the resonant frequencies are $\omega = \pm 2E_F/\hbar$, $\omega = \pm E_F/\hbar$ and $\omega = \pm 2E_F/3\hbar$, corresponding to the contribution for states at $\epsilon = \pm\hbar\omega/2$, $\epsilon = \pm\hbar\omega$ and $\epsilon = \pm 3\hbar\omega/2$, or the resonant transitions for which the Fermi level gap $2|E_F/\hbar|$ matches the frequencies of the one photon, two photon, and three photon transitions respectively [69, 71]. Interestingly, the coefficients for $\omega/2$, ω and $3\omega/2$ for the third-harmonic expression in Refs. [34, 69, 71], are $17/48$, $-4/3$ and $45/48$ respectively. As Mikhailov pointed out, different theories of the THz nonlinear response in 2D SLG may show somewhat contradictory [68] results, the difference between these coefficients being due to the

extreme complexity of the problem. However, we point out that Eq. (3.26) shows that the main contribution for third-harmonic conductance is from the $3\omega/2$ resonance. This observation is confirmed by the results from three independent models: Wright *et.al.* [52], Mikhailov [68] and Cheng *et.al.* [34, 69, 71].

A thorough analysis of our objection to the Wright *et.al.* [52] and Ang *et.al.* [55] calculation of the Kerr conductance for intrinsic 2D SLG is provided in the Appendix B below. The total third-order nonlinear current for metallic acGNR can be expressed as:

$$J_{\nu}^{(3)}(t) = g_{y\nu}^{(3)}(\omega)E_y e^{-i\omega t} + g_{y\nu}^{(3)}(3\omega)E_y e^{-i3\omega t} + c.c. \tag{3.27}$$

This result shows that for metallic acGNR, the third-order nonlinear current is a superposition of two frequency terms: (i) $g_{y\nu}^{(3)}(\omega)$, the third-order Kerr conductance, which has a single frequency electron current density term corresponding to the absorption of two photons and the simultaneous emission of one photon; and (ii), $g_{y\nu}^{(3)}(3\omega)$, the third-order third-harmonic conductance term corresponding to the simultaneous absorption of three photons. The complex conjugate parts in Eq. (3.27) are for the emission process.

In this chapter we consider the case where the length of the ribbon $L_y \to \infty$, and as a result, we have a quasi continuum of states for the linear bands near the Dirac points in metallic acGNR. To simplify the discussion, we present results for acGNR20, the armchair graphene nanoribbon $N = 20$ atoms wide.

Figs. 3.2 to 3.7 present results computed using our model described in Section 3.2. Fig. 3.2 summarizes the comparison between the results for intrinsic 2D

SLG and acGNR, indicating that at low temperatures, the isotropic third-order Kerr conductances is significantly larger than for 2D SLG. At $T = 0\,\mathrm{K}$, the third-order third-harmonic conductance is zero. The room temperature Kerr conductance continues to be significantly larger, and the third-harmonic conductance becomes of the order of that for 2D SLG. Fig. 3.3 describes both the temperature and width dependence of the third-order conductances for thin, metallic acGNR. The decay with increasing temperature for the acGNR Kerr conductances are similar to that of 2D SLG, with the acGNR conductances maintaining their significantly larger relative size. For the third-harmonic conductances, quite different behavior is observed; the acGNR third-harmonic conductance is 0 at $T = 0\,\mathrm{K}$, increases to a maximum, and then decays much faster than for 2D SLG with further increases in temperature. The decay rate as a function of width for all acGNR third-order conductances is observed to follow a simple width dependence rule discussed below.

Fig. 3.4 describes the temperature dependence of the field strength required for the nonlinear conductance to dominate over the linear conductance. Results indicate that this critical field is quite small, varying from $1 - 5\,\mathrm{kV/m}$ for the third-order Kerr conductance, and exhibiting a minimum of $\sim 5\,\mathrm{kV/m}$ for the third-order third-harmonic conductance. Figs. 3.5 and 3.6 illustrate several novel features of the Kerr and third-harmonic conductances for *extrinsic* acGNR as a function of temperature. For the Kerr conductance, an antiresonance develops at low temperature and broadens with increasing E_F. For the third-harmonic nonlinearity, the antiresonance found at $T = 0\,\mathrm{K}$ for intrinsic acGNR is seen to shift to higher temperatures as E_F increases.

Finally, Fig. 3.7, illustrates the behavior of the third-order Kerr and third-harmonic nonlinearities for extrinsic acGNR as a function of excitation frequency $\omega = 2\pi f$. Most remarkably, the third-harmonic nonlinearity is non-zero over a finite bandwidth at $T = 0\,\mathrm{K}$; a result of the state-blocking that occurs in extrinsic material. The excitation-frequency dependence of the nonlinear conductances at room temperature is also show. In the discussion that follows, we investigate each of these features in more detail.

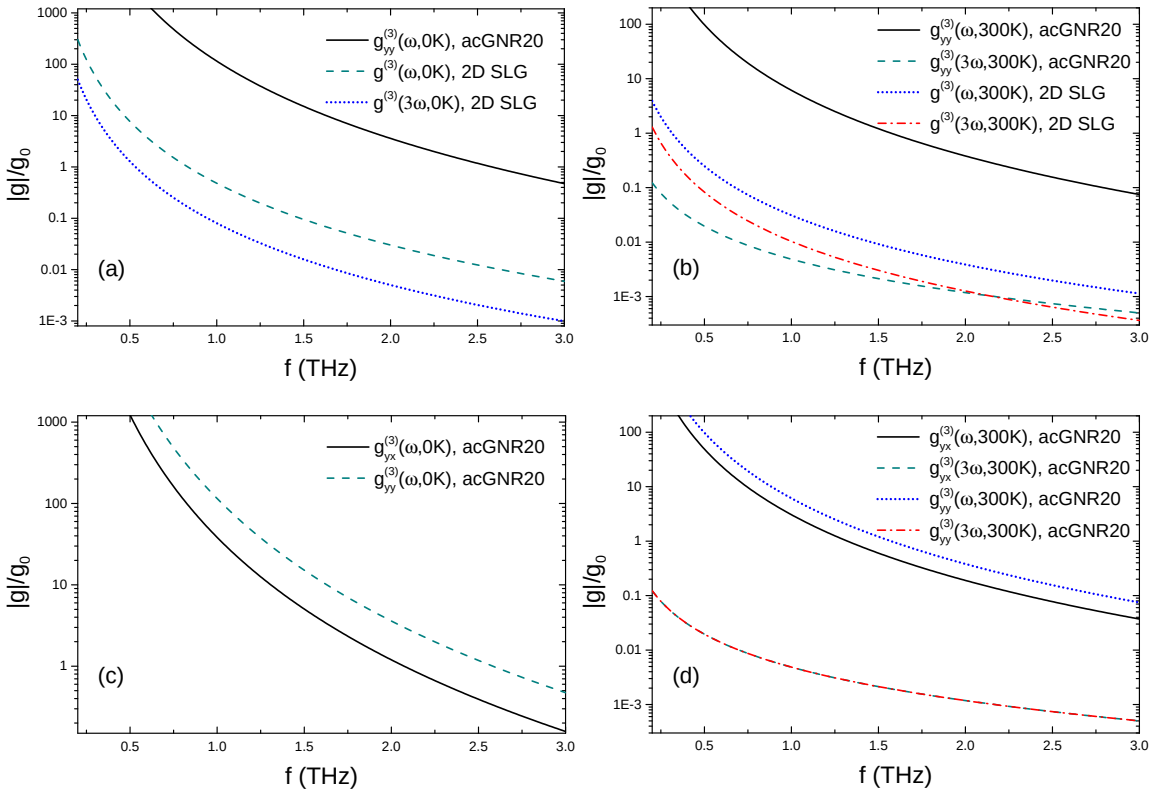

Figure 3.2: Comparison of the Kerr and third-harmonic nonlinear conductances for intrinsic acGNR20 with 2D SLG at (a) $T = 0\,\mathrm{K}$ and (b) $T = 300\,\mathrm{K}$; and comparison of isotropic and anisotropic conductances for acGNR20 at (c) $T = 0\,\mathrm{K}$ and (d) $T = 300\,\mathrm{K}$. The field strength used in all calculations is $E_y = 10\,\mathrm{kV/m}$ and the excitation frequency $f = \omega/2\pi$.

The frequency dependent nonlinear conductance in units of $g_0 = e^2/4\hbar$ for intrinsic acGNR20, calculated assuming an applied field strength of 10 kV/m, is plotted in Fig. 3.2, together with the third-order Kerr conductance of 2D SLG. Both nonlinear terms for intrinsic metallic acGNR20 and 2D SLG decrease rapidly with frequency. The huge nonlinearities at lower frequencies are associated with the strong interaction of carriers with low energy photons. The third-order Kerr conductance, $g^{(3)}_{y\nu}(\omega)$ for acGNR20 is approximately three orders of magnitude larger than that for 2D SLG.

The exact enhancement factor for nonlinear conductances in metallic acGNR is a function of the nanoribbon width, and from Eqs. (3.21) and (3.22), is determined to be $v_F/\omega Lx$. Due to the thermal factor cancellation in the expression for the nonlinear third-harmonic conductance, $g^{(3)}_{y\nu}(3\omega)$ tends to be much less than $g^{(3)}_{y\nu}(\omega)$. When $T = 0$ K, the third-harmonic conductance is zero for intrinsic acGNR20. For $T = 300$ K, the third-harmonic conductance is of the same order as for 2D SLG.

In Fig. 3.3, we illustrate the temperature and width dependence of the third-order nonlinear conductance for intrinsic metallic acGNR and 2D SLG for an excitation frequency of 1 THz and an applied field strength of 10 kV/m. In Figs. 3.3a and 3.3b, $g^{(3)}_{y\nu}(\omega)$ is shown to decrease monotonically with temperature T. However, $g^{(3)}_{y\nu}(3\omega)$ is initially zero at $T = 0$ K and increases to its maximum value (~ 2 orders of magnitude above that for 2D SLG) at approximately $T = 17$ K (the exact location of the maximum is a function of the thermal factor appearing in the expressions for the conductance). It then decreases at a faster rate then $g^{(3)}_{y\nu}(\omega)$ for $T > 17$ K. The rate

of decrease with temperature for $g^{(3)}_{yy}(\omega)$ is approximately the same as for 2D SLG.

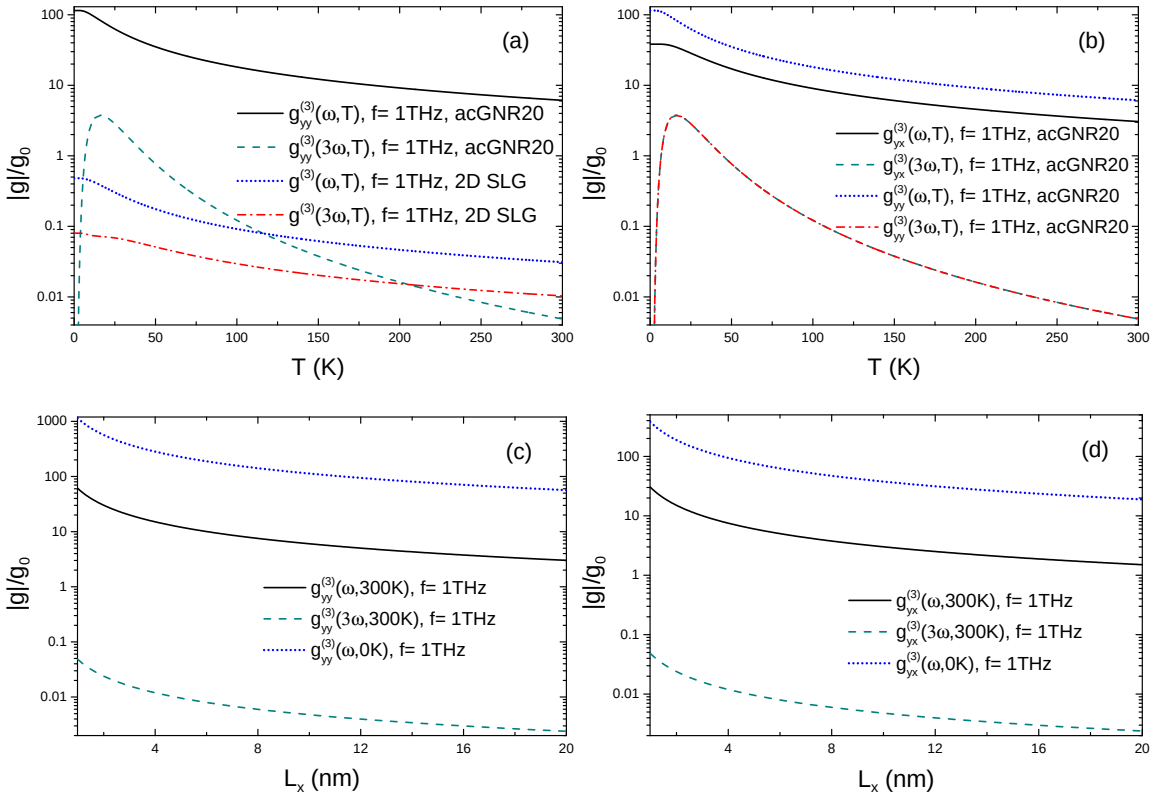

Figure 3.3: Comparison of the temperature dependence of the Kerr and third-harmonic nonlinear conductances for (a) intrinsic acGNR20 with that of 2D SLG; (b) isotropic and anisotropic nonlinear conductances for intrinsic acGNR20; comparison of the nanoribbon width dependence of (c) the Kerr and third-harmonic isotropic nonlinear conductances; and (d) the Kerr and third-harmonic anisotropic nonlinear conductance. The excitation frequency used in all calculations is $f = \omega/2\pi = 1\,\mathrm{THz}$.

In Figs. 3.3c and 3.3d we see that both third-order nonlinear conductance components are inversely proportional to the width of the acGNR L_x. This dependence of the conductance on L_x is due to the unitless factor $v_F/\omega L_x$ in Eqs. (3.21)

and (3.22), which implies that the total quasi-1D nonlinear current is constant and invariant of the nanoribbon width. We see that for $L_x \simeq 20\,\text{nm}$, or acGNR164, $g^{(3)}_{y\nu}(\omega)$ is still greater than that of 2D SLG for an excitation frequency of 1 THz, which again suggests that thin metallic acGNR ($L_x \leqslant 20\,\text{nm}$) manifests a much stronger Kerr conductance $g^{(3)}_{y\nu}(\omega)$ than 2D SLG over a wide range of widths. These findings suggest that metallic acGNR of submicron width is a better candidate than 2D SLG for nonlinear THz device applications.

In order to evaluate the frequency-conversion device potential of metallic acGNR, we define a critical field strength $E^{(3)}_{c,y\nu}(\omega, T)$ as the field strength when the nonlinear conductance dominates over the linear conductance ($|g^{(3)}_{y\nu}|/g_0 > 1$ where $g_0 = e^2/4\hbar$).

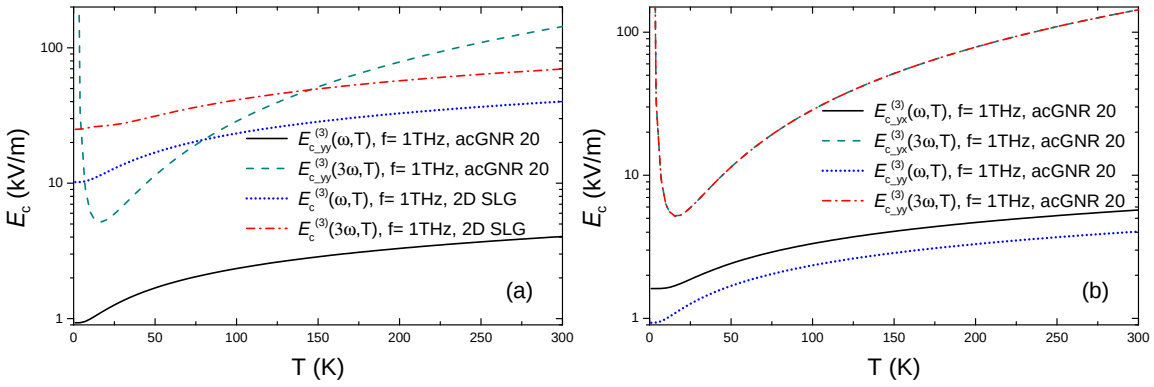

Figure 3.4: Comparison of the temperature dependence of the critical fields for (a) the isotropic Kerr and third-harmonic processes for intrinsic acGNR20 with those of 2D SLG; and (b) the isotropic and anisotropic Kerr and third-harmonic nonlinear processes for intrinsic acGNR20. The excitation frequency used in all calculations is $f = \omega/2\pi = 1\,\text{THz}$.

In Fig. 3.4 we plot the temperature dependence of the critical field strength for intrinsic metallic acGNR assuming a 1 THz excitation frequency. Fig. 3.4a illustrates the change in critical field as a function of temperature for both intrinsic metallic acGNR and 2D SLG. Due to the thermal factor cancellation, at low temperatures, the third-order conductance $g^{(3)}_{y\nu}(3\omega)$ for acGNR20 exhibits a larger critical field strength than 2D SLG. As the thermal distribution broadens with increasing T, the critical strength drops to 10% of the critical field strength for 2D SLG. As the temperature rises further, $E^{(3)}_{c,y\nu}(3\omega, T)$ increases until it rises above that for 2D SLG near $T = 170\,\mathrm{K}$ again. For the Kerr conductance term, the critical field $E^{(3)}_{c,y\nu}(\omega, T)$, increases as temperature increases, but it stays ~ 1 order of magnitude below the critical field for 2D SLG. Further, the relatively small change in critical field for $g^{(3)}_{y\nu}(\omega)$ from $T = 0\,\mathrm{K}$ to $T = 300\,\mathrm{K}$ indicates that metallic acGNR should exhibit excellent frequency conversion efficiencies for the optical Kerr process. The critical field strength we obtained is much smaller than the damage threshold [74], the strong nonlinear response, or the small values of the critical field exhibited by metallic acGNR for both Kerr and third-harmonic nonlinearities suggest that, low THz and low doped metallic acGNR are preferable to exploit the nonlinearity at intensities well below the damage threshold [80]. As a result, low dopend thin metallic acGNR will be excellent for use in the fabrication of nonlinear optical frequency-conversion devices [17, 74].

In Figs. 3.5 and 3.6 we study the Kerr $g^{(3)}_{y\nu}(\omega)$ and third-harmonic $g^{(3)}_{y\nu}(3\omega)$ conductances as a function of the Fermi level E_F (since the behavior of the system is symmetric for E_F about $E_F = 0$ in Figs. 3.5a and 3.6a, we only plot results for

positive E_F). For E_F well below the optical phonon energy ($\sim 200\,\text{meV}$), we plot the

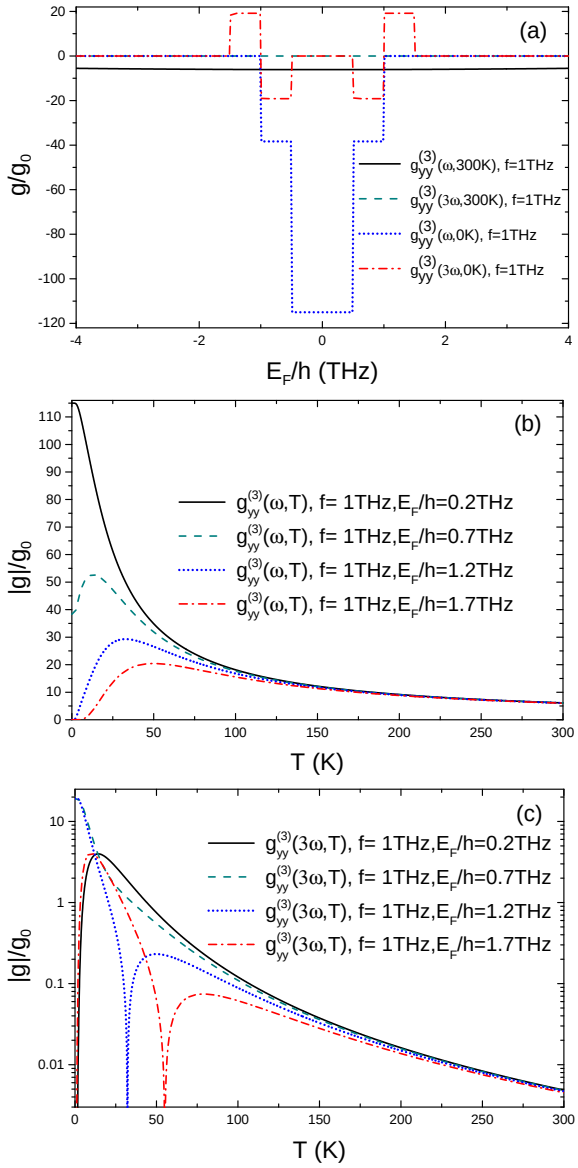

Figure 3.5: (a) The E_F dependence of the isotropic Kerr and third-order nonlinear conductances of acGNR20 at $T = 0\,\text{K}$ and $T = 300\,\text{K}$; (b) the temperature dependence of the isotropic Kerr nonlinear conductance of acGNR20 for various Fermi levels; and (c) the temperature dependence of the isotropic third-harmonic nonlinear conductances of acGNR20 for various Fermi levels. The excitation frequency used in all calculations is $f = \omega/2\pi = 1\,\text{THz}$.

Fermi-level dependence of $g^{(3)}_{y\nu}(\omega)$ and $g^{(3)}_{y\nu}(3\omega)$ assuming a 1 THz excitation at $T = 0$ K and $T = 300$ K. Perhaps the most important observations are for the 0 K case. We see three threshold frequencies for E_F/h: 0.5 THz, 1 THz and 1.5 THz. These frequencies correspond to turning on/off the thermal distribution [34, 68, 69, 71] at $\omega/2$, ω and $3\omega/2$. We note that $g^{(3)}_{y\nu}(3\omega)$ is nonzero over the $\omega/2$ to $3\omega/2$ doping window. In this window, only the $N(\omega)$ thermal factor term contributes to the $g^{(3)}_{y\nu}(3\omega)$ transition. Near room temperature, there are always electron and hole states [34,69,71] in the energy range determined by the thermal factor. As a result, we always observe nonzero conductance at all non-zero temperatures. This result suggests that at low temperatures, light doping will greatly enhance $g^{(3)}_{y\nu}(3\omega)$. But the enhancement we observe at low temperature for $g^{(3)}_{y\nu}(3\omega)$ disappears near room temperature. Also, the curves for different values of E_F asymptotically approach the intrinsic acGNR conductance, as the temperature increases.

In Fig. 3.7, we compare the conductances $g^{(3)}_{y\nu}(\omega)$ and $g^{(3)}_{y\nu}(3\omega)$ of extrinsic acGNR20 ($E_F/h = 0.7$ THz) for different temperatures and with the corresponding values for intrinsic 2D SLG. For the $T = 0$ K case, we observe a sharp onset for both the isotropic and anisotropic Kerr conductances at E_F/h ($\omega/2\pi = 0.7$ THz) and a further increase at $2E_F/h$ ($\omega/2\pi = 1.4$ THz) for the isotropic Kerr conductance. These changes are due to different terms in the thermal factor turning on at these excitation frequencies (see Table I).

The third-harmonic result is significantly different at $T = 0$ K. In this case the conductance turns on abruptly at $2E_F/3h$ ($\omega/2\pi = 0.467$ THz) and turns off abruptly

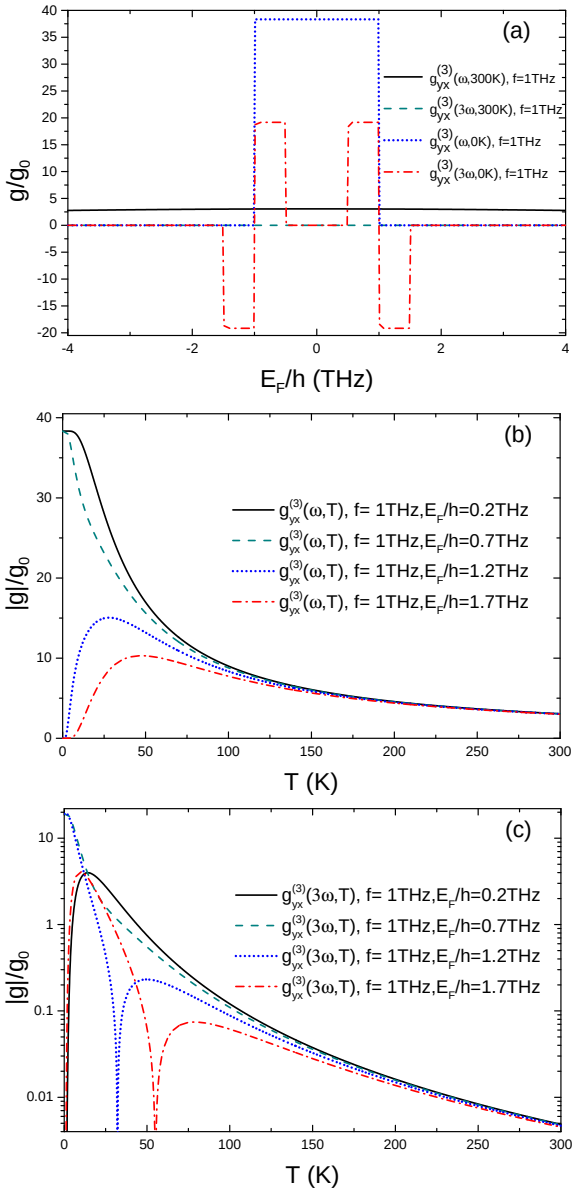

Figure 3.6: (a) The E_F dependence of the anisotropic Kerr and third-order nonlinear conductances of acGNR20 at $T = 0\,\mathrm{K}$ and $T = 300\,\mathrm{K}$; (b) the temperature dependence of the anisotropic Kerr nonlinear conductances of acGNR20 for various Fermi levels; and (c) the temperature dependence of the anisotropic third-harmonic nonlinear conductances of acGNR20 for various Fermi levels. The excitation frequency used in all calculations is $f = \omega/2\pi = 1\,\mathrm{THz}$.

at $2E_F/h$ ($\omega/2\pi = 1.4\,\mathrm{THz}$). These changes are also due to the relevant terms in the thermal factor turning on at particular excitation frequencies (see Table I). For

Table 3.1: Thermal Factor Terms for excitation frequency ω (*cf.* Eqs. (3.21) and (3.22))

Kerr Conductance ($T = 0\,\mathrm{K}$)	
Frequency Range	Thermal Factor Terms
$0 < \omega \leq E_F/\hbar$	all terms are 0
$E_F/\hbar < \omega \leq 2E_F/\hbar$	$N(\omega, E_F) = 1$
$\omega > 2E_F/\hbar$, isotropic	$2N(\omega/2, E_F) + N(\omega, E_F) = 3$
$\omega > 2E_F/\hbar$, anisotropic	$N(\omega, E_F) = 1$
Third-harmonic Conductance ($T = 0\,\mathrm{K}$)	
Frequency Range	Thermal Factor Terms
$0 < \omega \leq 2E_F/3\hbar$	all terms are 0
$2E_F/3\hbar < \omega \leq E_F/\hbar$	$-\frac{1}{2}N(3\omega/2, E_F) = -\frac{1}{2}$
$E_F/\hbar < \omega \leq 2E_F/\hbar$	$N(\omega, E_F) - \frac{1}{2}N(3\omega/2, E_F) = \frac{1}{2}$
$\omega > 2E_F/\hbar$	$-\frac{1}{2}N(\omega/2, E_F) + N(\omega, E_F) - \frac{1}{2}N(3\omega/2, E_F) = 0$

$T = 300\,\mathrm{K}$, we note that the extrinsic Kerr conductance is strongly enhanced over intrinsic 2D SLG, as it is in the intrinsic case. Further, the extrinsic third-harmonic conductance is of the same order as the 2D SLG nonlinear Kerr conductance value. Comparing the isotropic conductances with their anisotropic counterparts, we note similar behavior at $T = 300\,\mathrm{K}$. These results indicate that for low temperatures, there is a strong enhancement of the third-harmonic nonlinearity; however at room temperature, the Kerr nonlinearity dominates.

Finally, it is worth noting the limitations of our approach. The singularity around the Dirac point in metallic acGNR leads to high mobility, but acGNR can

be more prone to edge defects. Furthermore the $\mathbf{k} \cdot \mathbf{p}$ approximation is appropriate only at low energies, well below 2 eV [37]. For Fermi energies greater than optical phonon energy 200 meV, one needs to use a more basic tight-binding description, and the Dirac physics becomes largely irrelevant [37]. For undoped and lightly-doped acGNR, the Fermi energy is well away from these energy scales and the description in terms of the Dirac Hamiltonian should work relatively well.

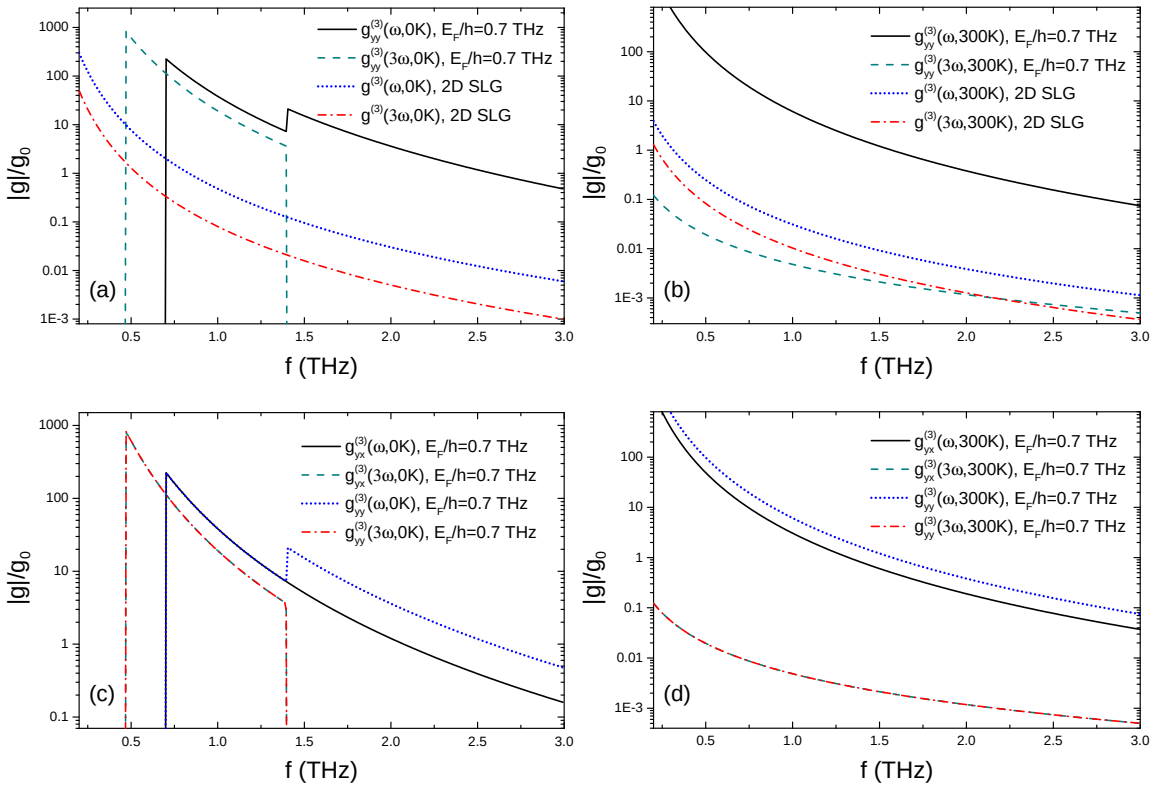

Figure 3.7: Comparison of isotropic Kerr and third-harmonic nonlinearities of extrinsic acGNR20 ($E_F/h = 0.7\,\mathrm{THz}$) at (a) $T = 0\,\mathrm{K}$; and (b) $T = 300\,\mathrm{K}$ with those of intrinsic 2D SLG; and comparison of isotropic and anisotropic Kerr and third-harmonic nonlinearities of extrinsic acGNR20 ($E_F/h = 0.7\,\mathrm{THz}$) at (c) $T = 0\,\mathrm{K}$; and (d) $T = 300\,\mathrm{K}$. The field strength used in all calculations is $E_y = 10\,\mathrm{kV/m}$ and the excitation frequency $f = \omega/2\pi$.

In this chapter, we assume there is no coupling of the local nonlinear current density with the spatial distribution of the applied electric field. Further, we treat the metallic acGNR with no applied longitudinal bias voltage, so that the Fermi level does not change across the longitudinal direction of the nanoribbon. It will be important to introduce additional effects in the present model such as the finite extent of the excitation field and the finite longitudinal size of the nanoribbon, as well as material effects such as electron-electron, electron-phonon interactions, and other edge effects. These topics are the subject of our future work.

3.4 Selection rules related to acGNR

In this section, we discuss the applicability of well-known selection rules for acGNR and 2D SLG to the problem of THz nonlinear harmonic generation in thin metallic acGNR. We focus on the interband transition in the lowest (linear) band ($k_{x,n} = 0$). The fact that we have nonzero g_{yy} and zero g_{xx} is consistent with the selection rules for acGNR found by Sasaki *et.al.* [75] and HC Chung *et.al.* [76]

In general, for 2D SLG there is no anisotropic current (J_y, J_x induced by E_x, E_y). The anisotropic conductance for intrinsic 2D SLG can be written:

$$g_{yx}^{(1)}(\omega)_{2D} = \lim_{\Gamma\to 0} -\frac{g_0}{\pi^2}\int_0^{2\pi}\sin(2\theta)d\theta\int_0^{\infty}\Re\left[i\frac{v_F^2}{\omega^2}\frac{kv_F}{2kv_F-\omega-i\Gamma}k\tanh(\frac{\hbar v_F k}{2k_BT})\right]dk$$

$$g_{yx}^{(3)}(\omega)_{2D} = \lim_{\Gamma\to 0}\frac{g_0}{\pi^2}\frac{\eta^2}{2}\int_0^{2\pi}\sin(2\theta)d\theta \times\int_0^{\infty}\Re\left[i\frac{v_F^2}{\omega^2}\frac{k^2v_F^2[-kv_F+\omega+kv_F\cos(2\theta)]}{[(2kv_F-\omega)^2+\Gamma^2](kv_F-\omega-i\Gamma)}k\tanh(\frac{\hbar v_F k}{2k_BT})\right]dk$$

$$g_{yx}^{(3)}(3\omega)_{2D} = \lim_{\Gamma\to 0}\frac{g_0}{\pi^2}\frac{\eta^2}{6}\int_0^{2\pi}\sin(2\theta)d\theta \times \int_0^{\infty}\Re\left[i\frac{v_F^2}{\omega^2}\frac{kv_F[k^2v_F^2 - 3kv_F\omega + 4\omega^2 - k^2v_F^2\cos(2\theta)]k\tanh(\frac{\hbar v_F k}{2k_BT})}{(2kv_F-\omega-i\Gamma)(kv_F-\omega-i\Gamma)(2kv_F-3\omega-i3\Gamma)}\right]dk \tag{3.28}$$

where $\eta = \frac{eA_yv_F}{\hbar\omega} = \frac{eE_yv_F}{\hbar\omega^2}$ measures the e-h coupling strengh. Using this result, we see that because $\int_0^{2\pi}\sin(2\theta) = 0$, the conductance terms $g_{yx}^{(i)}(\omega_0)_{2D} = 0$ for 2D SLG. The $g_{xy}^{(i)}(\omega_0)_{2D} = 0$ from similar analysis. The zero anisotropic current in 2D SLG results from that fact that the net sum is zero over all possible angles, and agrees with the quantum analysis performed in Ref. [68] for 2D SLG.

However, as shown above for metallic acGNR, J_ν, $\sigma_{\mu\nu}^{(i)}(m,\omega)$ has the general form:

$$\sigma_{y\nu}^{(i)}(m,\omega) = F_{y\nu}^{(i)}(|k_y|)\cos(\theta_{k_n,k_y}) \tag{3.29}$$

For metallic acGNR, we no longer integrate all possible angles as we did for 2D SLG. Due to the 1D nature of acGNR, we only have $\theta_{k_n,k_y} = 0,\pi$ depending on the sign of k_y, and thus we only evaluate at two angles according to the initial condition given by Eq. (3.4) when we evaluate the total current density J_ν for metallic acGNR. As a result, J_ν is not always zero for all E_F, ω and T. For direct interband transitions between states where $k_{x,n} \neq 0$, we make a similar argument as we only require states at $|\epsilon| = \hbar v_F k_{x,n}\csc(\theta_{k_n,k_y})$ to be at resonance. Thus, we only have the θ_{k_n,k_y} and $\pi - \theta_{k_n,k_y}$ pair as the two solutions. In this way, we extend the selection rules of the direct interband transition for acGNR to the J_x case, *i.e.* $k_{x,n}$ does not change from initial state to final state. This is the same requirement as for J_y in acGNR.

3.5 Concluding Remarks

Kimouche *et.al.* [48] and Jacobberger *et.al.* [49] have successfully fabricated ultrathin, smooth acGNR with widths $L_x < 10\,\text{nm}$. Our calculation of the nonlinear conductance in acGNR suggest that experimental measurements of the THz nonlinear response in thin metallic acGNR should be measurable at relatively low excitation field strengths. The relatively small critical field strength at room temperature implies that thin metallic acGNR have significant potential for nonlinear device applications. The striking turn on and turn off of the third-order harmonics with small changes in Fermi level at low temperatures suggest that metallic acGNR could be the the basis for developing a sensitive graphene-based low temperature detector or oscillator.

In this chapter, we have modeled the third-order THz response of metallic acGNR using a nonlinear semi-analytical approach. The time-dependent Dirac equation for massless Dirac Fermions is solved via the Fourier expansion method. We have shown intrinsic metallic acGNR exhibits strong nonlinear effects from the THz to the FIR regime under applied electric field amplitudes less than $10\,\text{kV/m}$. We also describe the behavior of these nonlinearities for extrinsic, metallic acGNR. Under certain conditions, metallic acGNR will exhibit a larger nonlinear conductance, require less applied electric field strength to generate moderate strong high harmonics and show better temperature stability than intrinsic 2D SLG. This opens the potential for use in many device applications for intrinsic and slightly doping metallic acGNR.

CHAPTER 4
QUANTUM SIZE EFFECTS IN THE TERAHERTZ THIRD ORDER NONLINEAR RESPONSE OF METALLIC ARMCHAIR GRAPHENE NANORIBBONS

[1] In this chapter, we use time dependent perturbation theory to study quantum size effects on the terahertz nonlinear response of metallic graphene armchair nanoribbons of finite length under an applied electric field. Our work shows that quantization due to the finite length of the nanoribbon, the applied field profile, and the broadening of the graphene spectrum all play a significant role in the resulting nonlinear conductances. In certain cases, these effects can significantly enhance the nonlinearity over that for infinitely-long metallic armchair graphene nanoribbon.

4.1 Introduction

Graphene has many unique electronic, mechanical, thermal and optoelectronic properties [2]. A tunable Fermi level and linear dispersion relation near the Dirac point are some of the features that make graphene attractive for the study of nonlinear effects in the terahertz (THz) regime [6–8, 16–18]. Various theoretical predictions of the generation of higher-order harmonics in graphene structures had been performed [32,52,57,63–65]. Recent experimental reports on the measurement of the THz nonlinear response in single- and multi-layer graphene [19–21] further demonstrate that graphene structures possess a strong nonlinear THz response. These theoretical

[1]This chapter was published in *IEEE. J. Sel. Top. Quant. Electro.* **23**(*1*), 5100108 (2017) [81].

and experimental studies demonstrate that, when compared to conventional parabolic semiconductor structures, unique graphene properties, such as linear energy dispersion, high electron Fermi velocity and tunable Fermi level, lead to a stronger nonlinear optical response in many 2D graphene structures [6–8, 16–21, 32, 52, 57, 63–65].

Unlike the extensive research on the nonlinear response of 2D graphene structures, prior to our work, only the linear THz response [9,82] and selection rules [75,76] of graphene nanoribbons (GNR) for a linearly polarized electric field have been investigated. Thin GNRs (sub-20 nm) with smooth edges can be treated as quantum wires, not dominated by defects [22]. The reduced dimensionality of 2D graphene to a quasi 1D quantum wire for narrow GNR opens the study of new physics (including quantization of energy, momentum *etc.*). GNRs have two types of edges: armchair graphene nanoribbons (acGNR) and zigzag graphene nanoribbons (zzGNR). These two types of GNR shows distinct electronic characteristics due to the geometry and boundary conditions [39–42]. In general, redistribution of the Dirac fermions induced by the applied electric field in momentum and energy space leads to large THz nonlinearities in GNR. The resulting nonequilibrium distribution predicts the conductivity components oscillating in time and space, and spatially homogeneous steady state components. As a result, nonlinear response in GNRs are sensitive to the applied field strength and polarization [8].

A widely used model, the perturbation of the Fourier expansion of the wavefunction first adopted by Wright *et.al.* [52] in the study of the THz nonlinear response of various 2D graphene systems [32, 52, 55, 57] has two important assumptions: *i)* the

absence of coupling between the induced nonlinear response and the applied electric field spatial profile; and *ii)* charge carriers propagate with ideal ballistic transport in graphene, with the absence of broadening due to various scattering processes [10]. Velickỳ, Mašek and Kramer have developed a model of the AC ballistic/quasi-ballistic conductance in 1D quantum wires with an arbitrary spatial profile of the applied electric field [83–85]. Wróbel *et.al.* measured and analyzed the role of reduced dimensionality in the quantized conductance of an GaAlAs/GaAs quantum wire [86, 87]. As thin GNRs with finite length in our study possess a low dimensional mesoscopic structure, it is natural to use these ideas to extend this analytical approach to the nonlinear response of thin GNRs with an applied electric field.

Carrier relaxation in graphene near the Dirac point is caused primarily by scattering of hot carriers [88–91]. Two typical carrier relaxation times have been reported, 25 ps for $E_F \ll 200\,\text{meV}$, where 200 meV corresponds to the optical phonon energy [88] and a few ps for states involving optical phonon scattering [88–93]. Current limitations to the utilization of thin GNRs for nonlinear device applications result from scattering due to edge defects and hot carriers [89–91,94–96]. Furthermore, edge disorder can affect the interband transition process due to the extra energy required to satisfy the conservation laws in the interband transition process [92,97]. Our work focuses on the THz emission due to direct interband transition of graphene carriers with energy $\ll 200\,\text{meV}$ in thin metallic acGNR. Scattering due to hot carriers and optical phonons is reduced for the THz direct interband transition [90,97,98]. Further, scattering due to acoustic phonons is prohibited for these interband transition [98].

Therefore, carrier relaxation in finite GNR structures mainly depends on edge disorder and defects.

Theoretical studies show that non-perfect edges destroy the quantization of the conductance for GNRs [99]. However, the rapid development of techniques for the synthesis of thin GNRs [22,48,49], show that thin GNR may have ultra smooth edges, higher mobility, and longer carrier mean free path than expected theoretically. The recent reported synthesis of ultra thin acGNR (sub-10 nm) show that the electronic structure of ultrathin acGNR is not strongly affected by defects (kinks) [48, 49]. It is possible for thin GNR mesoscopic structures grown in the laboratory to show ballistic and quasi-ballistic transport. Scattering along the channel direction is greatly reduced in the ballistic and quasi-ballistic regime [4]. Such progess in the state of art of the growth of ultra thin GNR highlights the potential for quasi 1D GNR mesoscopic structures to be used in modern ultra-high-speed electronic and quantum devices [4]. Thus the study the nonlinear electrodynamics for thin metallic acGNR with an applied electric field with finite length in the mesoscopic regime is of particular significance today.

In this chapter, we present important new results showing that the quantum size effects of nanonribbon length, spectral broadening, and excitation field coupling significantly modify the THz nonlinear response of thin metallic acGNR. *These novel effects play an essential role in the behavior of THz nonlinearities in acGNR, and have not previously been investigated.* In particular, we find that quantization of the broadened Dirac particle spectrum results in a transition from a discrete quantum dot-

like spectrum for small nanoribbon lengths to a continuous spectrum as the length of the nanoribbon increases. We evaluate the boundary between these two qualitatively distinct behaviors in terms of the coupling between adjacent energy states due to the broadening. Further, we find that the exact spatial profile of the THz excitation field plays a significant role in the nonlinear response. The spatial Fourier spectrum of the excitation field serves to enhance the nonlinearity at photon energies near states where the spectrum exhibits maxima, and reduces the response near spectral minima. By apodizing [100] the excitation field profile it becomes possible to optimize the THz nonlinearities at a particular desired pump frequency.

The chapter is organized as follows: In Section 4.2, we model the THz nonlinear response for thin metallic acGNR of finite length. We analyze the nonlinear response of these acGNR in the presence of intrinsic broadening and the coupling of the applied electric field profile to study the impact of quantum size effects on the THz nonlinearities. In Section 4.3, we apply our model to calculate the nonlinear THz conductance of thin metallic acGNR. We analyze the dependence of the third-order nonlinear terms on the ribbon length, temperature, and length of illumination. Following the introduction of broadening, we propose an effective critical length, characterizing the quantization of energy due to finite length impacting the continuum of states. We then show that in metallic acGNR with length smaller than the effective critical length, the THz third-harmonic conductance is greatly enhanced to nearly the order of the THz third-order Kerr conductance in the THz regime. This result shows that the tunability of thin metallic acGNR in the terahertz regime is increased.

Finally, we present our conclusions in Section 4.4.

4.2 Model

Following the low energy model for GNR [41, 42], the time-dependent, unperturbed $\mathbf{k}\cdot\mathbf{p}$ Hamiltonian for a single Dirac fermion near the Dirac points may be written in terms of Pauli matrices as $H_{0,K} = \hbar v_F \boldsymbol{\sigma}\cdot\mathbf{k}$ for the $\mathbf{K}$ valley and $H_{0,K'} = \hbar v_F \boldsymbol{\sigma}\cdot\mathbf{k}'$ for the $\mathbf{K}'$ valley with $\mathbf{k}\,(\mathbf{k}')$ the perturbation from the center of the $\mathbf{K}\,(\mathbf{K}')$ valley. The time-independent (unperturbed) Hamiltonian for GNR may be written:

$$H_0 = \hbar v_F \begin{pmatrix} 0 & k_x - ik_y & 0 & 0 \\ k_x + ik_y & 0 & 0 & 0 \\ 0 & 0 & 0 & -k_x - ik_y \\ 0 & 0 & -k_x + ik_y & 0 \end{pmatrix} \tag{4.1}$$

with wavefunctions in the case of acGNR:

$$\psi_{n,s} = \frac{e^{ik_y y}}{2\sqrt{L_x L_y}} \begin{pmatrix} e^{-i\theta_{k_n,k_y}} e^{ik_n x} \\ s e^{ik_n x} \\ -e^{-i\theta_{k_n,k_y}} e^{-ik_n x} \\ s e^{-ik_n x} \end{pmatrix} \tag{4.2}$$

where $L_x = Na_0/2$ is the width of the acGNR in the $\hat{x}$ (zigzag) direction, L_y is the length of the acGNR in the $\hat{y}$ (armchair) direction, and $\theta_{k_n,k_y} = \tan^{-1}(k_n/k_y)$ is the direction of the isospin state. This Hamiltonian does not include intervalley scattering processes due to its block-diagonal character.

The width of acGNR determines the metallic or semiconductor character of the acGNR [41, 42]. In general, acGNR of $N = 3M - 1$ atoms wide along the zigzag edge, with M odd, are metallic, whereas all other cases are semiconducting. The energy dispersion relation arising from this model is doubly-degenerate, with one

branch coming from each of the **K** and **K′** valleys.

4.2.1 AC conductance

Due to the quasi-1D structure of the thin acGNR [22] and the resultant quantization in k space, we need to consider the coupling of the applied electric field with the quantized k-states. The AC conductance $\tilde{g}(\omega)$ is defined in terms of the absorbed power $P(\omega)$ for an acGNR locally excited with electric field $\mathbf{E}(\mathbf{r},\omega)$:

$$\tilde{g}(\omega) \equiv \frac{P(\omega)}{\phi^2(\omega)/2}, \quad \phi(\omega) = \int \mathbf{E}(\mathbf{r},\omega)\cdot d\mathbf{r} \tag{4.3}$$

where $\phi(\omega)$ is the change of the electric potential in the irradiated region. The absorbed power may be expressed by the conductivity and the acting field as:

$$\tilde{g}(\omega) = \frac{1}{2}\int \frac{dk}{2\pi}\,\sigma(k,\omega)\,|E(k,\omega)|^2 \tag{4.4}$$

The ith order AC conductance for infinitely long acGNR $\tilde{g}^{(i)}_{y\nu}(\omega)$ is written [83–85]:

$$\tilde{g}^{(i)}_{y\nu}(\omega,L) = \frac{g_s g_v L_y}{2\pi}\int_{-\infty}^{+\infty} dk_y\,\sigma^{(i)}_{y\nu}(m,\omega)\left(\frac{\sin(k_y L/2)}{k_y L/2}\right)^2 \tag{4.5}$$

with L the length of illumination. For simplicity, we assume a constant field strength over the length of illumination L.

Defining $\omega_y = k_y v_F$, the corresponding angular frequency of k_y in GNR with a group velocity of v_F in the relaxation-free approximation, neglecting all scattering effects [10], we rewrite Eq. (4.5) for the third-order AC conductance as:

$$\tilde{g}^{(3)}_{y\nu}(\omega,L) = \sum_{l=1}^{2} 2\int_0^{\infty} d\omega_y\,\tilde{f}^{(\omega)}_{y\nu}(\omega_y,\frac{\omega l}{2})\delta(\omega_y-\frac{\omega l}{2}) \tag{4.6a}$$

$$\tilde{g}^{(3)}_{y\nu}(3\omega,L) = \sum_{l=1}^{3} 2\int_0^{\infty} d\omega_y\,\tilde{f}^{(3\omega)}_{y\nu}(\omega_y,\frac{\omega l}{2})\delta(\omega_y-\frac{\omega l}{2}) \tag{4.6b}$$

where

$$\tilde{f}_{y\nu}^{(\omega_0)}(\omega_y, \frac{\omega l}{2}) = f_{y\nu}^{(\omega)}(\omega_y, \frac{\omega l}{2}) N(\omega_y) S(\omega_y, L) \tag{4.7}$$

with the thermal factor:

$$N(\omega_y) = \frac{\sinh\left(\frac{\hbar|\omega_y|}{k_B T}\right)}{\cosh\left(\frac{E_F}{k_B T}\right) + \cosh\left(\frac{\hbar|\omega_y|}{k_B T}\right)} \tag{4.8}$$

and the illumination factor:

$$S(\omega_y, L) = \mathrm{sinc}^2\left(\frac{\omega_y L}{2 v_F}\right) \tag{4.9}$$

and where the Fermi level is $E_F = h f_\mu$, and $f_{y\nu}^{(\omega_0)}(\omega_y, \frac{\omega l}{2})$ is the coefficient associated with the corresponding $\delta(\omega_y - \frac{\omega l}{2})$ term in the expansion of the expression for the local third-order conductivity (see [10, eq. (41-42)]).

With an applied electric field linearly polarized along the $\hat{y}$ direction of an infinitely long acGNR, for the metallic band where $k_{x,n} = 0$, the AC isotropic nonlinear conductance becomes [10]:

$$\tilde{g}_{yy}^{(1)}(\omega, L) = -g_0 \eta_x N\left(\frac{\omega}{2}\right) S\left(\frac{\omega}{2}, L\right) \tag{4.10a}$$

$$\tilde{g}_{yy}^{(3)}(\omega, L) = -g_0 \eta\, \eta_x \sum_{l=1}^{2} \left(\frac{1}{2}\right)^{-z(l)} N\left(\frac{\omega l}{2}\right) S\left(\frac{\omega l}{2}, L\right) \tag{4.10b}$$

$$\tilde{g}_{yy}^{(3)}(3\omega, L) = -g_0 \eta\, \eta_x \sum_{l=1}^{3} \left(-\frac{1}{2}\right)^{z(l)} N\left(\frac{\omega l}{2}\right) S\left(\frac{\omega l}{2}, L\right) \tag{4.10c}$$

similarly, the AC anisotropic nonlinear conductance is:

$$\tilde{g}_{yx}^{(1)}(\omega, L) = g_0 \eta_x N\left(\frac{\omega}{2}\right) S\left(\frac{\omega}{2}, L\right) \tag{4.11a}$$

$$\tilde{g}_{yx}^{(3)}(\omega, L) = g_0 \eta\, \eta_x N(\omega) S\left(\omega, L\right) \tag{4.11b}$$

$$\tilde{g}_{yx}^{(3)}(3\omega, L) = g_0 \eta\, \eta_x \sum_{l=1}^{3} \left(-\frac{1}{2}\right)^{z(l)} N\left(\frac{\omega l}{2}\right) S\left(\frac{\omega l}{2}, L\right) \tag{4.11c}$$

where the quantum conductance $g_0 = e^2/(4\hbar)$, Fermi level $E_F = hf_\mu$, harmonic constant $z(l) = \left[1-(-1)^l\right]/2$, gain due to the width $\eta_x = (g_s g_v v_F)/(\omega L_x)$ and the coupling strength $\eta = \left(e^2 E_y^2 v_F^2\right)/(\hbar^2\omega^4)$. The illumination factor $S(\omega, L)$ in Eq. (4.10) and Eq. (4.11) arises from the finite illumination length and is the square modulus of the Fourier transform of the applied field profile. As a result of the inversion symmetry inherent in acGNR, the *2*nd-order current makes no contribution to the total current.

The total third-order nonlinear conductance for metallic acGNR then can be expressed as:

$$\tilde{g}^{(3)}_{tot,y\nu}(\omega, L) = \tilde{g}^{(3)}_{y\nu}(\omega, L)e^{-i\omega t} + \tilde{g}^{(3)}_{y\nu}(3\omega, L)e^{-i3\omega t} + c.c. \tag{4.12}$$

This result shows that for infinitely long metallic acGNR, the third-order nonlinear conductance is a superposition of two frequency terms: *i)* $\tilde{g}^{(3)}_{y\nu}(\omega, L)$, the Kerr conductance term corresponding to the absorption of two photons and the simultaneous emission of one photon; and *ii)* $g^{(3)}_{y\nu}(3\omega, L)$, the third-harmonic conductance term corresponding to the simultaneous absorption of three photons. The complex conjugate parts in Eq. (4.12) are for the emission process.

We observe that by taking the limit $L \to 0$, the ideal conductance and AC conductance in our definition are equivalent: $g^{(i)}_{\mu\nu}(\omega) = \tilde{g}^{(i)}_{\mu\nu}(\omega, 0)$. For $L = 0$, there is no coupling between the induced nonlinear response and the applied field spatial profile. Due to the current operator $qv_F\sigma_{x,y}\delta(\mathbf{r} - \mathbf{r_{op}})$ used in our previous work [10], we assume graphene carriers at $\mathbf{r_{op}}$ interact only with the incoming photon field at $\mathbf{r_{op}}$. The conductance $g^{(i)}_{\mu\nu}(\omega)$ is a special case of the AC conductance $\tilde{g}^{(i)}_{\mu\nu}(\omega, L)$, and

the AC conductance $\tilde{g}^{(i)}_{\mu\nu}(\omega, L)$ reduces to the ideal conductance $g^{(i)}_{\mu\nu}(\omega)$ at $L = 0$.

4.2.2 Broadening

We employ a Gaussian broadening model to study the impact on the nonlinear conductance due to spectral broadening of acGNR in the THz regime. This Gaussian broadening method has been widely used in the study of many graphene and GNR structures [101–103]. The Gaussian kernel,

$$Z_g(\omega_y, \omega) = \frac{1}{\sqrt{\pi}\Gamma_\omega} \exp\left[-\frac{(\omega_y - \omega)^2}{\Gamma_\omega^2}\right] \tag{4.13}$$

with $\Gamma_\omega = 2\pi f_\Gamma = 2\pi \left(2\tau\sqrt{\ln 2}\right)^{-1}$ and τ the relaxation time, replaces the Dirac delta function in the integrand of Eq. (4.6).

In this work, we neglect edge defects in the acGNR. We further assume the broadening parameter remains a constant in the THz regime, and is invariant of the temperature and applied field strength E_y. We obtain the value $\tau = 25\,\text{ps}$ from [88, Table I] and therefore, the broadening parameter used in Eq. (4.13) becomes $f_\Gamma = 0.024\,\text{THz}$. This choice of the broadening parameter is appropriate because the direct interband transition in the THz regime is well below the 200 meV optical phonon band. We note however, that our model can be extended to situations with larger carrier scattering. As τ is reduced, the quantization of the conductance tends to be dominated by other scattering processes. As a result, the mean free path of the carriers becomes shorter, and the interaction between adjacent states defined by the quantization condition becomes stronger.

4.2.3 Quantization due to finite length

In all real nanoribbons, the length L_y of the nanoribbon will be finite. This results in a discrete set of electronic states along the k_y direction, as opposed to the continuum of states that results for $L_y \to \infty$. In this case, the resulting third-order conductances are obtained by summing over the discrete set of states rather than integrating over the continuum.

In metallic acGNR, when $k_{x,n} = 0$, the energy dispersion relation may be written $\epsilon = s|m|\hbar\omega_{y0}$, with $\omega_{y0} = 2\pi v_F/L_y$. For a finite nanoribbon length of L_y and broadening Γ_ω, with $\omega_y = m\omega_{y0}$, the third-order AC conductance becomes:

$$\tilde{g}^{(3)}_{y\nu}(\omega, L, L_y, \Gamma_\omega) = \sum_{m=0}^{\infty}\sum_{l=1}^{2} 2\tilde{f}^{(\omega)}_{y\nu}(\omega_y, \frac{\omega l}{2}) Z_g(\omega_y, \frac{\omega l}{2})\omega_{y0} \tag{4.14a}$$

$$\tilde{g}^{(3)}_{y\nu}(3\omega, L, L_y, \Gamma_\omega) = \sum_{m=0}^{\infty}\sum_{l=1}^{3} 2\tilde{f}^{(3\omega)}_{y\nu}(\omega_y, \frac{\omega l}{2}) Z_g(\omega_y, \frac{\omega l}{2})\omega_{y0} \tag{4.14b}$$

4.3 Results and Discussion

We consider thin acGNR with finite length L_y, for which there exists an energy quantization with quantum number m, for states of the linear bands near the Dirac points in thin metallic acGNR. To simplify the discussion, we present results for acGNR20, the armchair graphene nanoribbon $N = 20$ atoms wide, which can be treated as a quasi 1D quantum wire [22], and the applied field strength is $E_y = 10\,\mathrm{kV/m}$ throughout. In what follows, we summarize the characteristics of the AC nonlinear conductance for all combinations of length of illumination and Fermi level, given in Eq. (4.14). We plot the isotropic and anisotropic AC conductances as a function of L_y with $T = 0\,\mathrm{K}$ and $300\,\mathrm{K}$, and $L \to 0$ for intrinsic acGNR in Fig. 4.1.

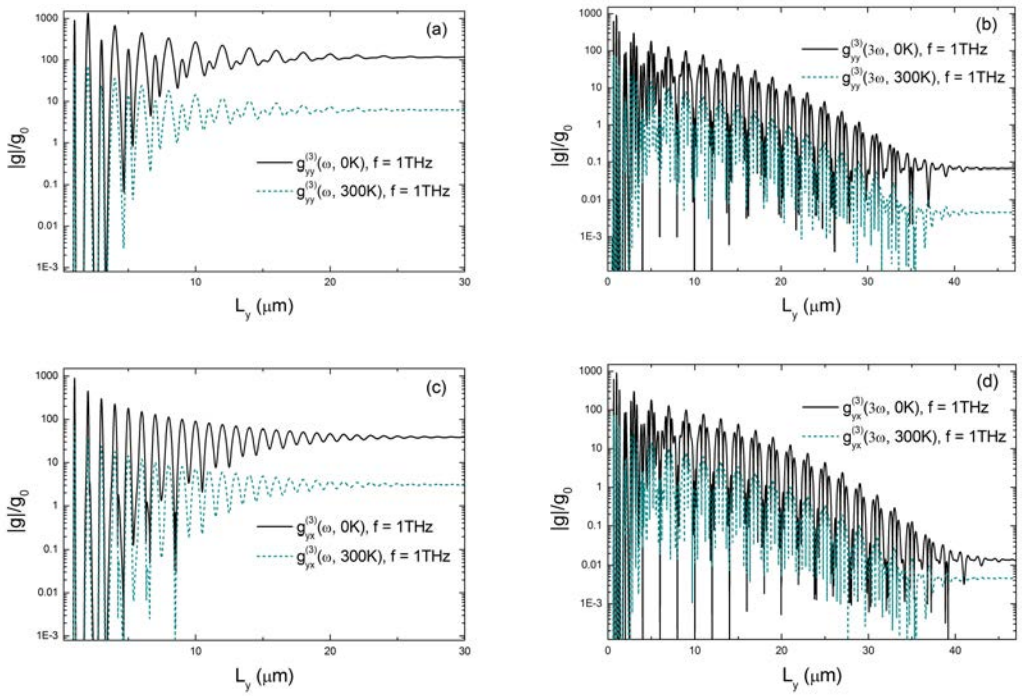

Figure 4.1: Magnitude of the third-order nonlinear conductances in acGNR20 at $T = 0\,\mathrm{K}$ and $300\,\mathrm{K}$ as a function of nanoribbon length L_y. a) isotropic Kerr conductance, b) isotropic third-harmonic conductance, c) anisotropic Kerr conductance, and d) anisotropic third-harmonic conductance. For all plots, $f = 1\,\mathrm{THz}$, $E_F = 0$, $L = 0$, and $f_\Gamma = 0.024\,\mathrm{THz}$.

The frequency of the applied field is $f = 1\,\mathrm{THz}$. Due to the energy quantization resulting from finite L_y, interband transitions can only be excited for states coupled by the excitation frequency $2\pi f = \omega$, namely those where $\omega/2 = M\omega_{y0}/2$ (single-photon resonance), $\omega = M\omega_{y0}$ (two-photon resonance), and $3\omega/2 = 3M\omega_{y0}/2$ (three-photon resonance for the third-harmonic nonlinearity) where M is an integer and where $\omega_{y0} = 2\pi v_F/L_y$ is the separation between the discrete states. If M is odd,

then $M/2$ and $3M/2$ are not integers and states at these energies do not exist. This implies that contributions from the $\omega/2$ and $3\omega/2$ components of the conductance are nearly zero (exactly zero in the absence of broadening). If M is even, $M/2$ and $3M/2$ are both integers, thus contributions from the $\omega/2$ and $3\omega/2$ components of the conductance are non-zero. In summary, for $M = fL_y/v_F$ even, Eq. (4.14) is equivalent to Eqs. (4.10) and (4.11). For M odd, the $N(\omega/2)$ and $N(3\omega/2)$ terms in Eq. (4.14) are negligible. In Fig. 4.1, we can see clearly how the ribbon length L_y affects the conductance. For small L_y, the broadening is smaller than the separation between states and we observe quantization of the conductance. In essense, the acGNR behaves as a rectangular quantum dot. When L_y becomes longer, the states move closer together and there is overlap due to broadening for adjacent energy states. As a result, the overall conductance approaches a constant value. We arrive at an effective critical length $L_{yc}^{(\omega)} = 2v_F/3f_\Gamma$ bounding the quantum and continuum regions for the Kerr conductance. Similarly, the effective critical length for the third-harmonic conductance $L_{yc}^{(3\omega)} = v_F/f_\Gamma$. Both critical lengths are independent of f in the THz regime. For $f_\Gamma = 0.024\,\mathrm{THz}$, $L_{yc}^{(\omega)} \sim 27\,\mu\mathrm{m}$ and $L_{yc}^{(3\omega)} \sim 42\,\mu\mathrm{m}$. When L_y is greater than the effective critical length, the conductance converges to the conductance of an infinitely-long acGNR, and we enter the quasi-continuum regime due to the fact that the broadening now overlaps adjacent states. Such asymptotic behaviour can be observed in Fig. 4.1 when L_y is greater than the critical length.

In Fig. 4.2 we plot the temperature dependence of the isotropic and anisotropic AC conductances for several nanoribbon lengths L_y with $L \to 0$. The frequency of

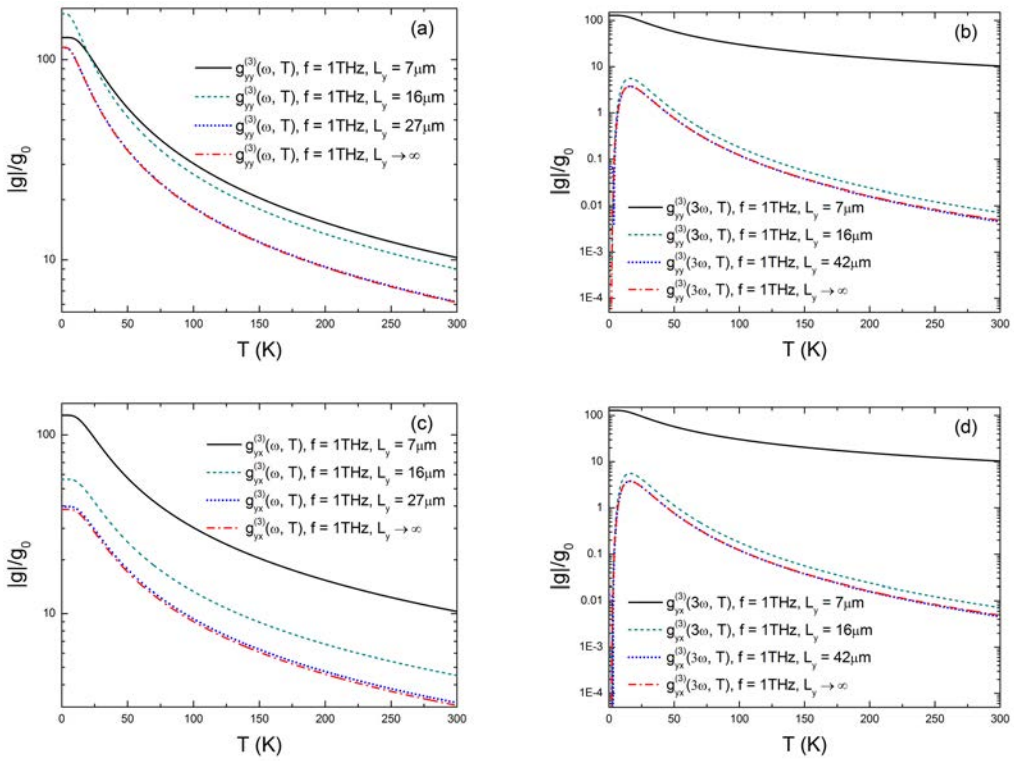

Figure 4.2: Magnitude of the third-order nonlinear conductances in acGNR20 for various nanoribbon lengths as a function of temperature T. a) isotropic Kerr conductance, b) isotropic third-harmonic conductance, c) anisotropic Kerr conductance, and d) anisotropic third-harmonic conductance. For all plots, $f = 1\,\mathrm{THz}$, $E_F = 0$, $L = 0$, and $f_\Gamma = 0.024\,\mathrm{THz}$ ($f_\Gamma \to 0$) for nanoribbons of finite (infinite) length.

the applied field is $f = 1\,\mathrm{THz}$. For the Kerr conductances as shown in Figs. 4.2a and 4.2c: when $L_y = 7\,\mu\mathrm{m}\,(M = 7)$, the conductance is dominated by the $N(\omega)$ term; when $L_y = 16\,\mu\mathrm{m}\,(M = 16)$, both the $N(\omega/2)$ and $N(\omega)$ terms contribute; and when $L_y = 27\,\mu\mathrm{m}$, we arrive at the critical length and the conductance is nearly the same as that for the infinitely-long nanoribbon for $T \geqslant 0\,\mathrm{K}$. For the third-

harmonic conductances as shown in Figs. 4.2b and 4.2d we observe similar behavior: when $L_y = 7\,\mu\text{m}\,(M = 7)$, the conductance is dominated by the $N(\omega)$ term; when $L_y = 16\,\mu\text{m}\,(M = 16)$, the $N(\omega/2)$, $N(\omega)$, and $N(3\omega/2)$ terms contribute; and when $L_y = 42\,\mu\text{m}$, we arrive at the critical length and the conductance is nearly the same as that for the infinitely-long nanoribbon for $T \geqslant 5\,\text{K}$.

It has been shown that the local AC current response depends on the spatial profile of the applied electric field for quasi 1D quantum wires [83–85]. In Fig. 4.3, we plot the isotropic nonlinear conductances as a function of the illumination length L. For the Kerr conductance plotted in Figs. 4.3a and 4.3b we note a series of antiresonances in the magnitude of the conductance. For the intrinsic nanoribbon, these antiresonances occur when the zeros of the illumination factor $S(\omega, L)$ are located at the same frequency as the states coupled by the excitation field of frequency f (those having non-negligible contributions from $N(\omega_y)$). For the Kerr conductance of the intrinsic nanoribbon with $L_y \to \infty$, both the $N(\omega/2)$ and $N(\omega)$ terms contribute to the conductance, resulting in an antiresonance spacing determined by setting the zeros in the illumination factor equal to $\omega/2$. This results in the set of antiresonances at $L = 2\,\mu\text{m}, 4\,\mu\text{m}, \ldots$. For the extrinsic case, there are two mechanisms contributing to the antiresonances: *1)* the zeros in the illumination factor, and *2)* state blocking due to the Fermi level offset. For example, in Fig. 4.3a ($T = 0\,\text{K}$), for the extrinsic nanoribbons transitions at $\omega/2$ are completely blocked, and therefore only the $N(\omega)$ term contributes, resulting in an antiresonance spacing determined by setting the zeros in the illumination factor equal to ω. This results in the set of antiresonances at

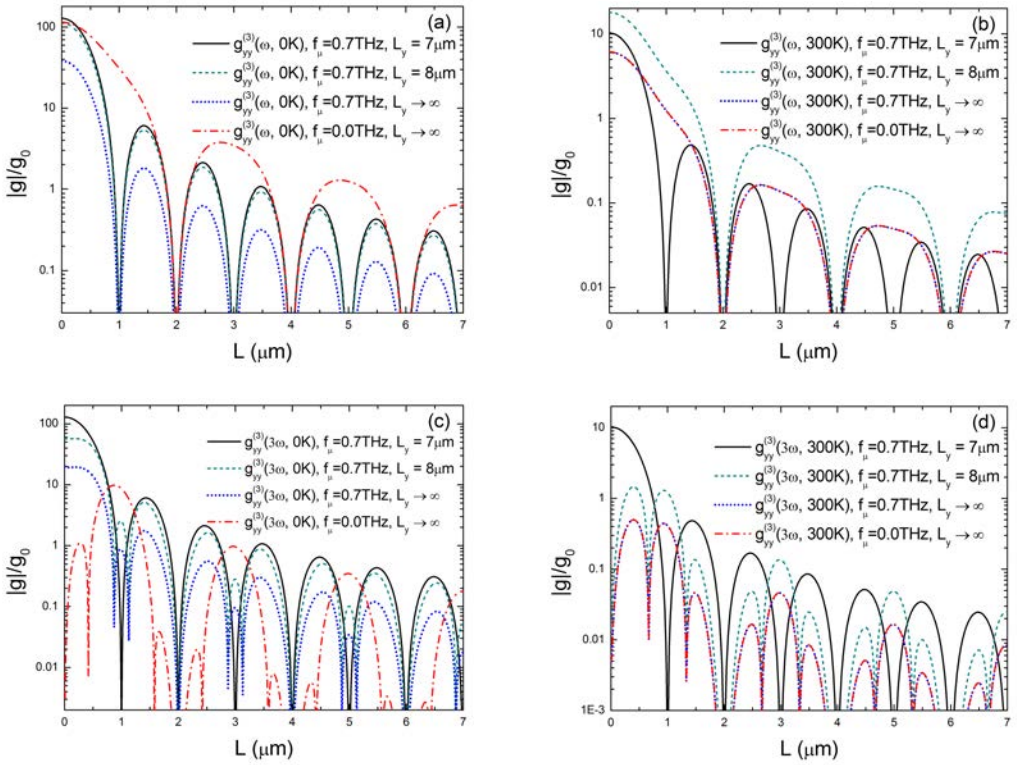

Figure 4.3: Magnitude of the isotropic third-order nonlinear conductances in acGNR20 for various nanoribbon lengths and Fermi levels as a function of illumination length L. a) Kerr conductance at $T = 0\,\mathrm{K}$, b) third-harmonic conductance at $T = 300\,\mathrm{K}$, c) Kerr conductance at $T = 0\,\mathrm{K}$, and d) third-harmonic conductance at $T = 300\,\mathrm{K}$. For all plots, $f = 1\,\mathrm{THz}$ and $f_\Gamma = 0.024\,\mathrm{THz}$ ($f_\Gamma \to 0$) for nanoribbons of finite (infinite) length.

$L = 1\,\mu\mathrm{m}, 2\,\mu\mathrm{m}, \ldots$ for both M even and odd. In contrast, for Fig. 4.3b ($T = 300\,\mathrm{K}$), for the M odd case, the $N(\omega/2)$ contribution is negligible and we obtain a similar result as for the $T = 0\,\mathrm{K}$ case. However, for M even, the $N(\omega/2)$ term is not completely blocked, and as a result (setting the zeros in the illumination factor equal to

$\omega/2$), we obtain antiresonances at $L = 2\,\mu\text{m}, 4\,\mu\text{m}, ...$

For the third-harmonic conductance plotted in Figs. 4.3c and 4.3d, the behavior is even richer than for the Kerr conductance. While the set of primary antiresonances follows the discussion above, a pair of sidelobe resonances surrounding each primary resonance is also observed. These sidelobe resonances result from the fact that the $N(\omega/2)$ and $N(3\omega/2)$ terms in the expression for the conductance (4.10c) have the opposite sign of the $N(\omega)$ term. Thus, for certain non-zero values of the illumination factor $S(\omega, L)$, the positive and negative thermal factor contributions exactly cancel and the sidelobe antiresonances manifest themselves. Because the exact value of the thermal factor functions change with temperature, the locations of these sidelobe antiresonances also shift with temperature. This effect can also be observed in Figs. 4.1b and 4.1d.

We also note here that for $T = 0\,\text{K}$, and $L_y \to \infty$, with a uniform illumination factor $S(\omega, L) = 1$ ($L \to 0$) the third-harmonic conductance is always zero for intrinsic nanoribbons and only non-zero over a limited frequency range for extrinsic nanoribbons ($2|E_F|/3 \leqslant \hbar\omega \leqslant 2|E_F|$) [10]. By extending the illumination range L (and therefore modulating the illumination factor) it is possible to enhance the third-harmonic conductance in these conditions so that for particular illumination lengths L, the third-harmonic conductance becomes of the order of the Kerr conductance magnitude.

In the interest of brevity, we do not plot the anisotropic nonlinear conductances, but simply note that the expression for the Kerr conductance contains only an

$N(\omega)$ term. As a result, the characteristics of the anisotropic Kerr conductance follows closely that of the isotropic Kerr conductance with resonances at $L = 1\,\mu\text{m}, 2\,\mu\text{m}, ...$ as discussed above. On the other hand, the anisotropic third-harmonic conductance contains all of the richness of its isotropic counterpart.

Fig. 4.4 illustrates the overall impact of the various quantum size effects we have discussed above on the magnitude of the third-order Kerr and third-harmonic conductances. In Figs. 4.4a and 4.4b, we plot the isotropic Kerr and third-harmonic conductances for several values of nanoribbon length L_y, temperature, and excitation frequency. The oscillatory nature of these curves highlights the interplay between the thermal factor (and thermal factor cancellation in the case of the third-harmonic conductance), state blocking, and the illumination factor. While the overall envelope of the $L_y = 10\,\mu\text{m}, L = 0.5\,\mu\text{m}$ conductances decay with increasing frequency as expected (generally following the results for the $L_y \to \infty, L = 0.5\,\mu\text{m}$ case), there is clearly a richness in the detailed oscillatory behavior governed by the exact characteristics of the illumination and sample geometries. Similar effects are noted in Figs. 4.4c and 4.4d for the anisotropic nonlinear conductances as well. It is also useful to point out here that it should be possible to modify this dynamical behavior by apodizing [100] the applied THz electric field. For example, by using a Gaussian-apodized profile for the applied electric field, it should be possible to eliminate the antiresonances induced by the illumination factor $S(\omega, L)$. This would significantly reduce the oscillatory character of the results presented in Fig. 4.4.

In summary, the results described above place important constraints on the

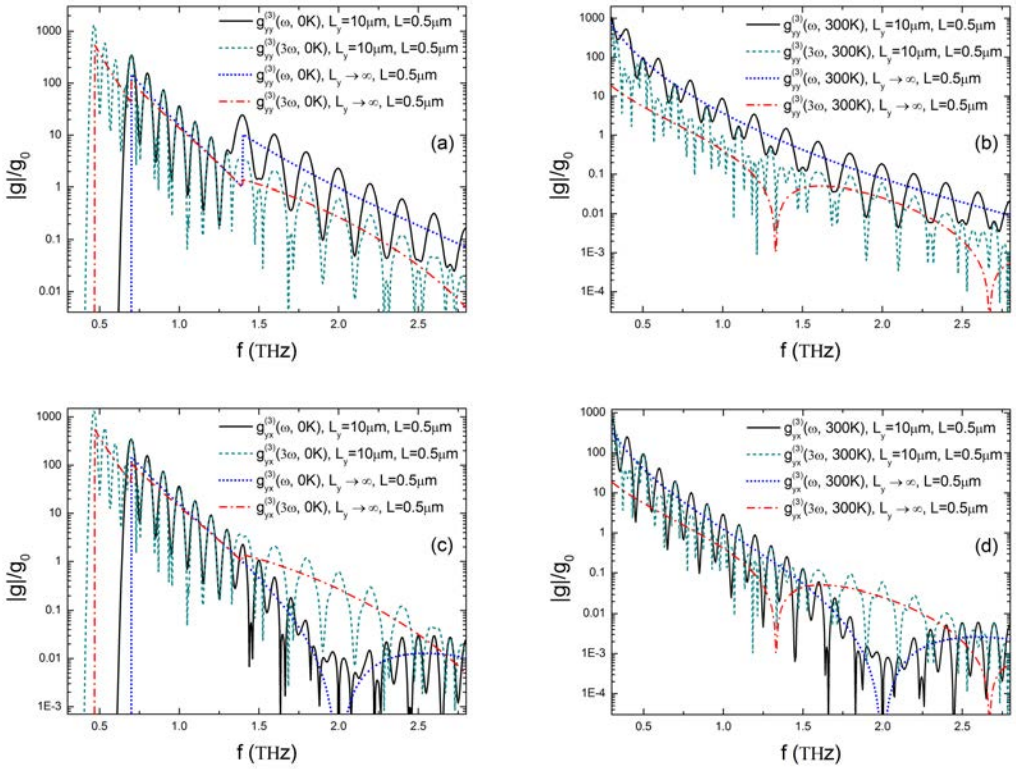

Figure 4.4: Magnitude of the third-order nonlinear conductances in acGNR20 for various nanoribbon and illumination lengths, and temperatures as a function of excitation frequency f. a) isotropic Kerr and third-harmonic conductances at $T = 0\,\mathrm{K}$, b) isotropic Kerr and third-harmonic conductances at $T = 300\,\mathrm{K}$, c) anisotropic Kerr and third-harmonic conductances at $T = 0\,\mathrm{K}$, and d) anisotropic Kerr and third-harmonic conductances at $T = 300\,\mathrm{K}$. For all plots, $E_F/h = 0.7\,\mathrm{THz}$ and $f_\Gamma = 0.024\,\mathrm{THz}$ ($f_\Gamma \to 0$) for nanoribbons of finite (infinite) length.

development of metallic acGNR THz devices. For a fixed excitation field frequency, the nanoribbon length L_y, illumination factor $S(\omega, L)$, intrinsic broadening Γ_ω, and carrier distribution (E_F) will need to be carefully considered based on a particular

device application. For example, by appropriate choice of these parameters, it is possible to use an acGNR to generate third-harmonic radiation at $T = 0\,\mathrm{K}$, whereas for other sets of parameters, the third-harmonic component is zero. While it is beyond the scope of this chapter to delve into such design details, we note that the results presented here will guide the designer toward an optimal design. The efficient THz nonlinear response of acGNR described above provides much promise toward the development of devices such as polarization switches, modulators, and efficient background-free third-harmonic generators.

4.4 Conclusion

In this chapter, we describe the results of detailed calculations of the quantum size effects on the nonlinear third-order conductances of acGNR. We report that novel effects due to both the size and spectral broadening of the nanoribbon, as well as the spatial profile of the excitation field, are important in determining the nonlinear response of acGNR. We compute the THz third-order nonlinearities of a thin, finite-length metallic acGNR. Our calculations show that there is a transition between quantum dot-like behavior for small L_y and quasi-continuum behaviour as L_y increases. The boundary between these two regimes is shown to be a function of the broadening of the Dirac spectrum of the nanoribbon. Additionally, we observe that the nonlinear response in metallic acGNR is strongly dependent on the shape of the spatial profile of the THz excitation field. By carefully choosing the spatial profile, it is possible to optimize the third-order nonlinearities for a particular excitation

frequency. In the results presented above, we present a detailed analysis of the features of the nonlinear spectral response due to these mechanisms.

Finally, we note two recent reports of the synthesis of high quality, ultrathin acGNR with widths $L_x < 10\,\text{nm}$ [48, 49]. The recent advent of this capability to fabricate acGNR underscores the importance of a complete understanding of the underlying nonlinear physics of these structures. AC transport in quasi 1D quantum wires is crucial for high speed quantum wire based integrated circuits [104]. The current work contributes to this understanding by demonstrating that acGNR have large nonlinearities that can be optimized through careful choice of design parameters such as the nanoribbon dimensions and the spatial profile of the excitation field.

CHAPTER 5
TERAHERTZ THIRD ORDER NONLINEAR RESPONSE OF METALLIC ARMCHAIR GRAPHENE NANORIBBON TO AN ELLIPTICALLY-POLARIZED EXCITATION FIELD

[1] In this chapter, we present a theoretical description of the third-order response induced by an elliptically-polarized terahertz beam normally-incident on intrinsic and extrinsic metallic armchair graphene nanoribbons. Our results show that using a straightforward experimental setup, it should be possible to observe novel polarization-dependent nonlinearities at low excitation field strengths of the order of 10^4 V/m. At low temperatures the Kerr nonlinearities in extrinsic nanoribbons persist to significantly higher excitation frequencies than they do for linear polarizations, and at room temperatures, the third-harmonic nonlinearities are enhanced by 2-3 orders of magnitude. Finally, the Fermi-level and temperature dependence of the nonlinear response is characterized.

5.1 Introduction

Graphene is a flat monolayer of carbon atoms tightly packed into a 2D honeycomb lattice. Graphene has emerged to be a very promising candidate for terahertz (THz) applications, and opens up the possibility of graphene based devices for THz optoelectronic and photonic applications [8]. Theoretical and experimental studies show that unique properties of graphene, such as linear dispersion relation near the Dirac point, high electron Fermi velocity, and tunable Fermi level lead to a strong non-

[1]This chapter has been submitted for publication.

linear response in 2D graphene structures and suggest it is a very promising candidate for THz applications [7,8,17–21,34,52,65,68,105]. This work opens up the possibility of graphene based devices for THz optoelectronic and photonic applications [2,8].

Following the first experimental of the study of absorption in the ellipsometric spectrum of graphene [106], the circular AC Hall effect [107–109], chiral edge currents [110,111], helicity-dependent photovoltaic Hall effect [8,107] and electronic chirality and berry phases [112] were observed by using circularly-polarized excitation fields. Higher-order harmonic generation [105,113] in 2D graphene has also been theoretically investigated, showing strong higher-order harmonics exists in graphene with an applied circularly-polarized harmonic electric field. This work shows that elliptically- or circularly-polarized light may be used to probe the unique nature of graphene near the Dirac points, including effects such as harmonic generation, frequency mixing, optical rectification, linear and circular photogalvanic effect, photon drag, photoconductivity, coherently controlled ballistic charge currents, pseudospin, chirality, and symmetry breaking [8,105–109,111,112].

In general, graphene nanoribbons (GNRs) have two types of edges: armchair edges (acGNR) and zigzag edges (zzGNR). Due to the the geometry and boundary conditions [39,41,42], these two types of GNRs show distinct electronic characteristics in the low energy regime. The linear and nonlinear response of GNRs due to a linearly-polarized electric field were studied in [9,10,75,81,82,114,115]. The non-perturbative DC conductance due to an applied circularly-polarized field in zzGNR and acGNR [114,115] was also investigated. However, there has been no investigation of the

nonlinear response in metallic acGNR for an elliptically polarized applied electric field.

In this chapter, we describe new results on the nonlinear response of intrinsic and extrinsic metallic acGNR (mGNR) excited by a normally-incident, *elliptically-polarized* THz electric field. GNR are metallic in the $\mathbf{k} \cdot \mathbf{p}$ approximation when the longitudinal direction ($\hat{y}$) of the nanoribbon is parallel to the armchair edge and the nanoribbon atomic width is $N = (3M - 1)$ with M odd. In this case the lowest sub-bands are linear in k_y, and for sufficiently narrow mGNRs ($L_x < \sim 20\,\text{nm}$), the higher sub-bands are far enough away that their contributions to the THz nonlinear conductance may be neglected. *Most significantly*, we show that at room temperature, the third-order nonlinear conductance at 3ω is enhanced by $2-3$ orders of magnitude using a circularly-polarized (CP) THz field over the same conductance when the excitation field is linearly-polarized (LP) [10]. We also show that the third-order conductances at ω and 3ω exhibit odd symmetry in the polarization state, resulting in current densities of opposite sign for opposite-handed elliptical polarizations. Finally, we analyze the Fermi level and temperature dependence of these nonlinearities and show that by varying the polarization state of the excitation field it is possible to tune the nonlinearities in both sign and amplitude. This novel behavior suggests a variety of applications in optical modulation, polarization switching, and harmonic generation over the THz region of the optical spectrum.

5.2 Model

Our $\mathbf{k}\cdot\mathbf{p}$ model employs Fourier analysis to solve the nonlinear Dirac equation using time-dependent perturbation theory in order to study the *polarization-dependent* nonlinear response in the THz regime. The model is an extension of one first applied by us in the context of graphene nanoribbons for the study of nonlinear effects induced by LP THz fields [10, 81]. However, we emphasize that the work presented below contains new physics as a result of the coupling between the polarization state of the incident field and the chiral mGNR wavefunctions, and is not a simple superposition of the previous description of LP THz excitations (although the previous results do exist as special cases of the current work).

In the following, we analyze nonlinear harmonic generation at THz frequencies induced by an elliptically-polarized beam normally-incident on a mGNR. The polarization ellipse is characterized by major and minor axes that coincide with the longitudinal and transverse axes of the nanoribbon. This polarization state can be achieved experimentally by passing a $\hat{y}$-polarized beam through a cascade of a half-wave plate oriented with its fast axis at an angle $\phi/2$ with respect to the polarization axis of the incident THz beam, and then through a quarter-wave plate oriented with its principle axes parallel to the longitudinal ($\hat{y}$) and transverse ($\hat{x}$) axes of the mGNR. The corresponding electric field may be expressed as $\mathbf{E} = [i\hat{x}E_x + \hat{y}E_y]\exp[-i\omega t] = E_0\left[i\hat{x}\sin(\phi) + \hat{y}\cos(\phi)\right]\exp[-i\omega t]$.

We begin by writing the polarization state of an elliptically-polarized beam with principal axes parallel to $\hat{x}$ and $\hat{y}$. In the Coulomb gauge for a source-free

region of constant scalar potential ($\nabla\varphi = 0$), the time-harmonic electric field turns on adiabatically at $t_0 = -\infty$ and the magnetic vector potential is $\mathbf{A} = \mathbf{E}/(i\omega)$. After making the substitution, $\mathbf{k}(\mathbf{k}') \rightarrow \mathbf{k}(\mathbf{k}') + q\mathbf{A}/\hbar$, we obtain a time and polarization-state dependent Hamiltonian H near the Dirac points of the mGNR [10, 81]. The Fourier expansion of the resulting perturbation wavefunction is written:

$$\psi(\mathbf{r}, t; m) = \sum_{l=0}^{\infty} \psi_0(m, l) \exp\left[i2\pi m y/L_y\right] \exp[-i\omega l t] \exp[-i\epsilon t/\hbar]$$

where m is the quantum number of k_y, l is the harmonic order of the electric field, and $\psi_0(m, l)$ is a spinor of order (m, l). Following Ref. [8,10,34,52,68], we obtain the third order current density in the perturbation limit, with $\omega_y = v_F 2\pi m/L_y$:

$$\begin{aligned}
J_\nu^{(3)}(\phi, t) =& \sum_{\alpha\beta\gamma} \Big[\exp\left[-i\omega t\right] \sigma^{(3)}_{\nu\alpha\beta\gamma}(\omega, -\omega, \omega) E_\alpha E^*_\beta E_\gamma \\
&+ \exp\left[-i\omega t\right] \sigma^{(3)}_{\nu\alpha\beta\gamma}(\omega, \omega, -\omega) E_\alpha E_\beta E^*_\gamma \qquad (5.1a) \\
&+ \exp\left[-i3\omega t\right] \sigma^{(3)}_{\nu\alpha\beta\gamma}(\omega, \omega, \omega) E_\alpha E_\beta E_\gamma \Big] + c.c. \\
=& \mathrm{e}\, \mathrm{g_s}\, \mathrm{g_v} \sum_m \Big[\psi_0(m, 1)^\dagger \frac{\partial H}{\hbar \partial k_\nu} \psi_0(m, 2) \exp[-i\omega t] \qquad (5.1b) \\
&+ \psi_0(m, 0)^\dagger \frac{\partial H}{\hbar \partial k_\nu} \psi_0(m, 3) \exp[-i3\omega t] \Big] N(\omega_y) + c.c. \\
=& \left[g_\nu^{(3)}(\omega, \phi) \exp[-i\omega t] \right. \qquad (5.1c) \\
&\left. + g_\nu^{(3)}(3\omega, \phi) \exp[-i3\omega t] \right] E_0 + c.c.
\end{aligned}$$

with the thermal factor defined as:

$$N(\omega_y) = \frac{\sinh\left(\frac{\hbar|\omega_y|}{k_B T}\right)}{\cosh\left(\frac{E_F}{k_B T}\right) + \cosh\left(\frac{\hbar|\omega_y|}{k_B T}\right)} \qquad (5.2)$$

with $\nu = x, y$ indicating the induced optical current component in the $\hat{\nu}$ direction.

5.3 Results and Discussion

The longitudinal Kerr conductance $g_{\nu}^{(3)}(\omega,\phi)$ and third-harmonic conductance $g_{\nu}^{(3)}(3\omega,\phi)$ for infinitely-long mGNR:

$$g_{y}^{(3)}(\omega,\phi) = g_0\left[f(\phi,-2,-1)N\left(\frac{\omega}{2}\right) + f(\phi,-1,-\frac{3}{2})N(\omega)\right] \tag{5.3a}$$

$$\begin{aligned} g_{y}^{(3)}(3\omega,\phi,\lambda) = g_0\Bigg[&f(\phi,\frac{1}{2},-\frac{1}{24})N\left(\frac{\omega}{2}\right) - f(\phi,1,\frac{5}{6})N(\omega) \\ &+f(\phi,\frac{1}{2},\frac{7}{8})N\left(\frac{3\omega}{2}\right)\Bigg] \end{aligned} \tag{5.3b}$$

and the transverse third-order conductances:

$$g_{x}^{(3)}(\omega,\phi) = g_0\left[f(\phi,1,-\frac{1}{2})N(\omega)\right] \tag{5.4a}$$

$$\begin{aligned} g_{x}^{(3)}(3\omega,\phi,\lambda) = g_0\Bigg[&-f(\phi,\frac{1}{2},-\frac{5}{24})N\left(\frac{\omega}{2}\right) + f(\phi,1,\frac{1}{6})N(\omega) \\ &-f(\phi,\frac{1}{2},\frac{7}{8})N\left(\frac{3\omega}{2}\right)\Bigg] \end{aligned} \tag{5.4b}$$

where $f(\phi,a,b) = \eta\eta_x\cos(\phi)\left[a\cos^2(\phi) + 2b\sin^2(\phi)\right]$, $g_0 = e^2/(4\hbar)$, Fermi level E_F, $\eta_x = (g_s g_v v_F)/(\omega L_x)$, and $\eta = (e^2E_0^2v_F^2)/(\hbar^2\omega^4)$. It is worth noting that for a circularly-polarized excitation field, a symmetry-breaking occurs in 2D SLG that allows second-harmonic generation to occur [8, 34, 105]. We will discuss how this symmetry-breaking affects second-harmonic generation in mGNR in our future work.

In Eqs. (5.3a) and (5.4a), $E_0 f(\phi,a,b)$ may be split into two terms:

$$E_0 f(\phi,a,b) = f_A(\phi,a)|E_y|^2E_y + f_B(\phi,b)P_{circ}E_x,$$

where the radiation helicity $P_{circ} = i\left[E_y(iE_x)^* - iE_xE_y^*\right] = E_0^2\sin(2\phi)$ [110]. $f_A(\phi,a)$ defines the conductivity tensor element $\sigma_{\nu yyy}^{(3)}$ and $f_B(\phi,b)$ defines the sum of conductivity tensor elements $\sum_{yxx}\sigma_{\nu yxx}^{(3)}$, where $\sum_{yxx}$ indicates the sum over the rotation

of indices νyxx, νxyx, and νxxy. We summarize the tensor elements obtained from Eqs. (5.3a) and (5.4a) in Table 5.1.

Table 5.1: Kerr conductivity tensor elements

single-photon $(-\omega/2 \to \omega/2)$ conductivity element(s)	value $(\times g_0\eta\eta_x/E_0^2)$
$\sigma^{(3)}_{yyyy}(\omega,-\omega,\omega)$	-2
$\sigma^{(3)}_{yxxy}(\omega,-\omega,\omega)+\sigma^{(3)}_{yyxx}(\omega,-\omega,\omega)$	-2
$\sigma^{(3)}_{yxyx}(\omega,-\omega,\omega)$	0
$\sigma^{(3)}_{xyyy}(\omega,-\omega,\omega)$	0
$\sigma^{(3)}_{xxxy}(\omega,-\omega,\omega)+\sigma^{(3)}_{xyxx}(\omega,-\omega,\omega)$	$+1$
$\sigma^{(3)}_{xxyx}(\omega,-\omega,\omega)$	-1
two-photon $(-\omega \to \omega)$ conductivity element(s)	value $(\times g_0\eta\eta_x/E_0^2)$
$\sigma^{(3)}_{yyyy}(\omega,\omega,-\omega)$	-1
$\sigma^{(3)}_{yxyx}(\omega,\omega,-\omega)+\sigma^{(3)}_{yyxx}(\omega,\omega,-\omega)$	-2
$\sigma^{(3)}_{yxxy}(\omega,\omega,-\omega)$	-1
$\sigma^{(3)}_{xyyy}(\omega,\omega,-\omega)$	$+1$
$\sigma^{(3)}_{xxyx}(\omega,\omega,-\omega)+\sigma^{(3)}_{xyxx}(\omega,\omega,-\omega)$	-2
$\sigma^{(3)}_{xxxy}(\omega,\omega,-\omega)$	$+1$

For the third-harmonic conductances, the splitting also holds for $E_0 f(\phi,a,b) = f_A(\phi,a)E_y^3 + f_B(\phi,b)E_x^2E_y/2$. We note that $f_A(\phi,a)$ and $f_B(\phi,b)$ are related to the conductivity tensor elements in the same way as above. We summarize the contributions to the third-harmonic conductivity tensor elements from the single-photon, two-photon, and three-photon transitions obtained from Eqs. (5.3b) and (5.4b) in Table 5.2.

Table 5.2: Third-harmonic conductivity tensor contributions

single-photon $(-\omega/2 \to \omega/2)$ conductivity component	value $(\times g_0\eta\eta_x/E_0^2)$
$\sigma^{(3')}_{yyyy}$	$+1/2$
$\sigma^{(3')}_{yxyx}+\sigma^{(3')}_{yyxx}+\sigma^{(3')}_{yxxy}$	$-1/12$
$\sigma^{(3')}_{xyyy}$	$-1/2$
$\sigma^{(3')}_{xxyx}+\sigma^{(3')}_{xyxx}+\sigma^{(3')}_{xxxy}$	$+5/12$
two-photon $(-\omega \to \omega)$ conductivity component	**value $(\times g_0\eta\eta_x/E_0^2)$**
$\sigma^{(3')}_{yyyy}$	-1
$\sigma^{(3')}_{yxyx}+\sigma^{(3')}_{yyxx}+\sigma^{(3')}_{yxxy}$	$-5/3$
$\sigma^{(3')}_{xyyy}$	$+1$
$\sigma^{(3')}_{xxyx}+\sigma^{(3')}_{xyxx}+\sigma^{(3')}_{xxxy}$	$+1/3$
three-photon $(-3\omega/2 \to 3\omega/2)$ conductivity component	**value $(\times g_0\eta\eta_x/E_0^2)$**
$\sigma^{(3')}_{yyyy}$	$+1/2$
$\sigma^{(3')}_{yxyx}+\sigma^{(3')}_{yyxx}+\sigma^{(3')}_{yxxy}$	$+7/4$
$\sigma^{(3')}_{xyyy}$	$-1/2$
$\sigma^{(3')}_{xxyx}+\sigma^{(3')}_{xyxx}+\sigma^{(3')}_{xxxy}$	$-7/4$

Here $\sigma^{(3')}_{\nu\alpha\beta\gamma}$ denotes $\sigma^{(3)}_{\nu\alpha\beta\gamma}(\omega,\omega,\omega)$

To simplify the discussion, in the following we present results for mGNR20, the metallic acGNR $N = 20$ atoms wide, for an applied field strength $E_0 = 10\,\mathrm{kV/m}$. From Eqs. (5.3) and (5.4), we see that illumination of an unbiased, infinitely-long mGNR by a THz harmonic electric field results in a nonlinear response that is strongly dependent on the polarization state of the applied field. Fig. 5.1 illustrates the polarization dependence of the longitudinal and transverse Kerr and third-harmonic nonlinear conductances at $T = 0\,\mathrm{K}$ and $300\,\mathrm{K}$ for intrinsic mGNR20.

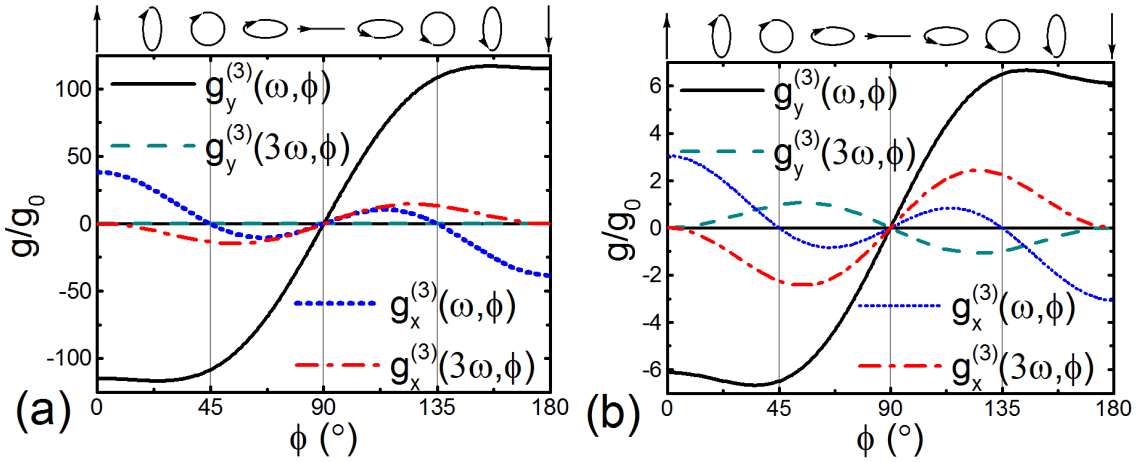

Figure 5.1: Kerr and third-harmonic conductances of mGNR20 as a function of the incident THz electric field polarization state (see top inset) for: (a) $T = 0\,\mathrm{K}$, and (b) $T = 300\,\mathrm{K}$. $f = 1\,\mathrm{THz}$, $E_0 = 10\,\mathrm{kV/m}$.

For CW (σ_+) and CCW (σ_-) CP, *i.e*, $\phi = 45°$ and $135°$, the third-order conductances are antisymmetric. The shape of the conductance is a superposition of the contribution from the E_y and E_x components. The overall dependence of the third order current component $J_\nu^{(3)}(\omega_0)$ is of the form [10, 52],

$$J_\nu^{(3)}(\omega_0) = g_\nu^{(3)}(\omega_0, \phi)E_0 = g_{\nu,A}(\omega_0)E_y + g_{\nu,B}(\omega_0)E_x \tag{5.5}$$

The first term, $g_{\nu,A} \propto e^2E_y^2/(\hbar^2\omega^4)$, and agrees with [8, 34, 52, 68]. The second term, $g_{\nu,B} \propto P_{circ}$ (see *e.g.* [110,111]). Due to the current operator used, there is no analog of left or right handedness for the carriers in mGNR [36]. The direction of the *optically induced third order current* results from the interference between the local current density excited by the elliptical polarization of the field, or the radiation helicity P_{circ}, and the isospin of the carriers [8, 36, 110, 112]. Finally, for the LP cases $\hat{y}$ and $\hat{x}$, ($\phi = 0°$ and $\phi = 90°$) respectively, contribution from the second term vanishes [112]

and we recover the results reported previously [10].

In Fig. 5.2 we compare the longitudinal and transverse Kerr and third-harmonic conductances as a function of the Fermi level E_F at $T = 0\,\mathrm{K}$. For E_F well below the optical phonon energy ($\sim 200\,\mathrm{meV}$), and a 1 THz excitation frequency for a LP field in the $\hat{y}$ direction ($\phi = 0°$) and σ_+ CP ($\phi = 45°$) we see thresholding behavior of the nonlinear conductances for the direct interband transition at low temperature [10]. The three critical frequencies for E_F/h: 0.5 THz, 1 THz and 1.5 THz correspond to turning off the thermal distribution at $\omega/2$, ω and $3\omega/2$ [10]. These frequencies are independent of the polarization states ϕ, and are only functions of $g_{\nu,A}(\omega_0)$ and$g_{\nu,B}(\omega_0)$ in Eq. (5.5).

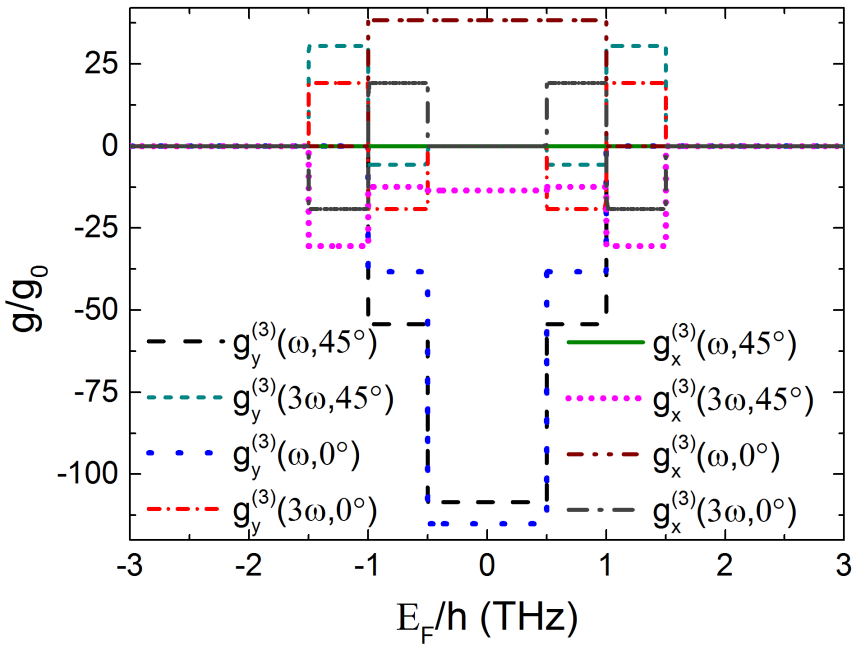

Figure 5.2: Longitudinal and transverse components of the Kerr and third-harmonic conductances for extrinsic mGNR20 as a function of the Fermi level E_F and incident field polarization state. For this plot $f = 1\,\mathrm{THz}$, $E_0 = 10\,\mathrm{kV/m}$, and $T = 0\,\mathrm{K}$.

In the interest of brevity, we note briefly that the overall temperature dependence of all non-zero extrinsic conductances show that the nonlinearity persists even up to room temperature. Further, the curves asymptotically approach the intrinsic mGNR conductance for a given polarization state as the temperature increases. It is also interesting to note that the transverse Kerr conductances are identically zero for CP, independent of the Fermi level and temperature, in qualitative agreement with [115]. This may be understood as the cancellation of the contribution from E_y and P_{circ} in Eq. (5.4a) for CP.

Fig. 5.3 illustrates the excitation-frequency ($2\pi f = \omega$) dependence of the Kerr and third-harmonic conductances for both $\hat{y}$ LP ($\phi = 0°$) and σ_+ CP ($\phi = 45°$) excitation fields in extrinsic mGNR20 ($E_F/h = 0.7\,\mathrm{THz}$). At $T = 0\,\mathrm{K}$ (Figs. 5.3a and 5.3c) both CP Kerr conductance components behave in a manner qualitatively similar to the LP result for the longitudinal component of the conductance while the transverse component of the LP conductance is zero. However the CP third-harmonic conductances behave quite differently from their LP counterparts. Whereas the low-temperature LP conductance components are bandlimited (nonzero over $2E_F/3h < f < 2E_F/h$), the transverse CP conductances *persist to significantly higher frequencies*, reducing to $|g|/g_0 = 0.1$ at approximately 2.7 THz. At $T = 300\,\mathrm{K}$ (Figs. 5.3b and 5.3d), another behavior is noted: while the CP and longitudinal component of the LP Kerr conductance follow a similar decay envelope with increasing excitation frequency, both CP third-harmonic conductance components are *enhanced by nearly three orders of magnitude* over their LP counterparts at $f = 1\,\mathrm{THz}$, and

this enhancement persists to higher frequencies and is still nearly two orders of magnitude at $f = 3\,\mathrm{THz}$. The enhancement for the transverse component of the CP third-harmonic conductance is observed to be slightly stronger than that for the longitudinal component of the CP third-harmonic conductance.

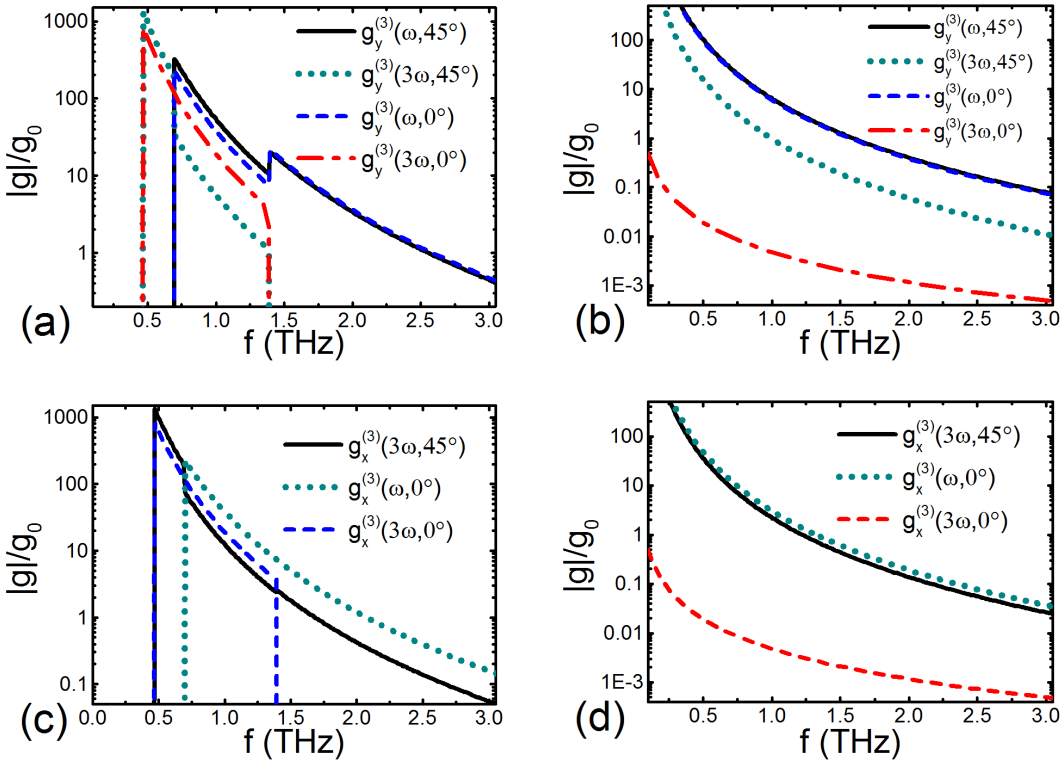

Figure 5.3: Excitation frequency ($2\pi f = \omega$) dependence of the components of nonlinear Kerr and third-harmonic conductances for extrinsic mGNR20 ($E_F/h = 0.7\,\mathrm{THz}$): a) longitudinal conductance at $T = 0\,\mathrm{K}$, b) longitudinal conductance at $T = 300\,\mathrm{K}$, c) transverse conductance at $T = 0\,\mathrm{K}$, and d) transverse conductance at $T = 300\,\mathrm{K}$. For all plots, $E_0 = 10\,\mathrm{kV/m}$. Note that for all temperatures, the CP transverse Kerr conductance is identically zero.

5.4 Conclusions

In conclusion, we report calculations describing the third-order nonlinear response of both intrinsic and extrinsic mGNR to an elliptically-polarized THz electric field. We show that the resulting Kerr conductances for extrinsic mGNR persist to significantly higher excitation frequencies at low temperature, and at room temperature, the CP third-harmonic conductances are enhanced by 2-3 orders of magnitude over their counterparts excited with only LP. Further, we describe the Fermi-level and temperature dependence of these nonlinearities. The enhancement in spectral range and magnitude for these nonlinearities suggests that they may exhibit wide applicability in THz devices excited with elliptically-polarized THz electric fields.

The recent synthesis of ultrathin mGNR with widths $L_x < 10\,\text{nm}$ [48, 49], coupled with the proposed experimental setup described in this chapter, suggest that experimental measurement of the THz nonlinear response in thin mGNR should be possible at relatively low excitation field strengths. Notably, the enhancement of the third-order third-harmonic nonlinearity with small changes in Fermi level and applied CP excitation field at room temperature indicates that mGNR may provide the basis for developing a sensitive graphene-based detector, broadband modulator, or source over a wide range of temperatures.

CHAPTER 6
TERAHERTZ THIRD ORDER NONLINEAR RESPONSE OF GAPPED ARMCHAIR GRAPHENE NANORIBBON

[1] In this chapter, we use time dependent perturbation theory to study the terahertz nonlinear response of *gapped* intrinsic and extrinsic nearly-metallic armchair graphene nanoribbons of finite length under an applied electric field. Generally, the nonlinear conductances exhibit contributions due to single-photon, two-photon, and three-photon processes. The interference between each of these processes results in remarkably complex behavior for the third-order conductances, including quantum dot signatures that should be measurable with a relatively simple experimental configuration. Notably, we observe sharp resonances in the isotropic third-order response due to the Van Hove singularities in the density of states at one-, two-, and three-photon resonances. However, these resonances are absent in the anisotropic third-order response; a result of the overall symmetry of the system.

6.1 Introduction

Graphene is a flat monolayer of carbon atoms arranged in a 2D honeycomb lattice. Unique properties of graphene, such as a linear dispersion relation near the Dirac point, high electron Fermi velocity, and tunable Fermi level lead to strong nonlinear response in various 2D graphene structures [6–8, 16–21, 32, 33, 52, 57, 63–65]. These studies suggest that graphene is a very promising candidate for graphene based

[1] This chapter has been submitted for publication.

terahertz (THz) optoelectronic and photonic applications [2, 8].

In general, graphene nanoribbons (GNRs) have two different edge states: armchair GNR (acGNR), where the armchair edge is parallel to the longitudinal axis of the nanoribbon, and zigzag GNR (zzGNR) where the zigzag edge is parallel to the longitudinal axis of the nanoribbon. Theses two types of GNR show distinct electronic properties [39–42]. Thin (sub-20 nm) GNR may be treated as quasi-1D quantum wires [22]. All experimental reports on thin high quality GNR show that they have an energy gap, including acGNR that are metallic in the ideal $\mathbf{k} \cdot \mathbf{p}$ approximation [5, 44–49] (in what follows, we label ideal gapless metallic acGNR as mGNR and gapped nearly-metallic acGNR as m*GNR). The energy gap of these m*GNR is inversely proportional to their width [44–47]. Several theoretical models have predicted the energy gap based on different edge terminations and calculation methods [23–29].

Recently, the linear and nonlinear response of GNR due to an applied linearly-polarized time-harmonic excitation electric have been studied [9, 10, 75, 76, 81, 82, 114, 115]. However to this point, there has been no report on the nonlinear THz response of m*GNR. Refs. [32–34] suggest that nonlinearities may increase in gapped 2D graphene with small band gap openings and thus it is important to study the effect of a gap on the THz nonlinear response in thin m*GNR.

In this chapter, we describe new results on the nonlinear THz response of intrinsic and extrinsic thin m*GNR excited by a normally-incident, linearly-polarized THz electric field. acGNR are metallic in the ideal $\mathbf{k} \cdot \mathbf{p}$ approximation when the longitudinal direction of the nanoribbon is parallel to the armchair edge and the

nanoribbon atomic width is $N = (3M - 1)$, with M odd. In this case the lowest sub-bands are linear in the longitudinal axis k_y, and for sufficiently narrow m*GNR ($L_x < \sim 20\,\mu m$), the higher sub-bands are far enough away that their contribution to the THz nonlinear conductance may be neglected. *Most significantly*, we show that the isotropic third-order nonlinear conductance is enhanced in m*GNR over the same conductance in mGNR when the excitation field is linearly-polarized (LP) [10, 81] for frequencies above the energy gap resonance. We also show that the anisotropic third-order conductances exhibit different behaviour than the isotropic results. Finally, we analyze the Fermi level and temperature dependence of these nonlinearities. This novel behavior suggests a variety of applications over the THz region of the optical spectrum.

6.2 Model

Nearly-metallic acGNR are predicted to have a small band gap inversely proportional to their width L_x [25, 26]. However, the energy gaps reported in [5, 23–29, 44–49] are functions of the different fabrication techniques, edge terminations and calculation methods used in these studies. We use the energy gap reported in [25] for thin m*GNR, as this band gap, induced by the asymmetry in the edge states, creates an onset energy offset $\mp E_g/2$ in the A, B sublattice respectively in the low energy regime [32–34]. This choice of energy gap has also been used to simulate the behavior of thin acGNR-based FETs as well [116–118], and agrees with the non-parabolic quantum-based simulation of thin acGNR FETs as well [117]. An electric

field strength of the order 1 GV/m has been predicted to modulate the energy gap E_g. The critical field strength derived from our previous work [10] for ideal thin mGNR, is of the order of $10-100\,\mathrm{kV/m}$, much smaller than $1\,\mathrm{GV/m}$ [25]. As a result, we do not expect the excitation field to induce a significant change in the thin m*GNR gap due to the small potential variation along the zigzag edge ($\hat{x}$ direction), while at the same time, we expect the excitation field to induce strong THz nonlinearities.

Thus, we model the bandgap versus width $L_x = Na_0/2$ for m*GNR in the presence of an applied electric field as $E_g = 0.04\,\mathrm{eV}/L_x(\mathrm{nm})$ [25]. Defining $E_{\mathrm{gap}} = 2\hbar\Omega_g = 2\hbar v_F k_\Delta$, we obtain $\Omega_g = v_F k_\Delta = 39.325\,\mathrm{THz}/N$ where N is the nanoribbon atomic width. Following the $\mathbf{k}\cdot\mathbf{p}$ model for gapped 2D SLG [32, 33], and GNR [41, 42], the time-independent unperturbed Hamiltonian for m*GNR in the absence of intravalley and intervalley scattering may be written:

$$H_0 = \hbar v_F \begin{pmatrix} \boldsymbol{\sigma}\cdot\mathbf{k} - k_\Delta\sigma_z & 0 \\ 0 & \boldsymbol{\sigma}\cdot\mathbf{k}' - k_\Delta\sigma_z \end{pmatrix} \tag{6.1}$$

with $\boldsymbol{\sigma} = \sigma_x\hat{\mathbf{x}} + \sigma_y\hat{\mathbf{y}}$, $\mathbf{k}(\mathbf{k}') = k_n(-k_n)\hat{\mathbf{x}} + k_y\hat{\mathbf{y}}$, $k(k') = \left(k_n^2 + k_y^2\right)^{1/2}$, $k_0 = \left(k^2 + k_\Delta^2\right)^{1/2}$ and $\theta_n = \tan^{-1}(k_n/k_y)$. The wavefunction for the unperturbed Hamiltonian H_0 of m*GNR becomes:

$$\psi_{n,s} = \frac{A}{k}\exp(ik_y y)\begin{pmatrix} \exp\left[i\left(k_n x - \theta_n\right)\right]\left(k_0 - sk_\Delta\right) \\ s\,k\exp(ik_n x) \\ -\exp\left[\text{-}i\left(k_x x + \theta_n\right)\right]\left(k_0 - sk_\Delta\right) \\ s\,k\exp(\text{-}ik_n x) \end{pmatrix} \tag{6.2}$$

Normalizing the wavefunction over the entire nanoribbon [41, 42], we obtain:

$$A = \left(2L_x L_y\right)^{-1/2}\left[1 + \left(k_0 - sk_\Delta\right)^2/k^2\right]^{-1/2} \tag{6.3}$$

We note that where the gap $E_g \to 0$, Eq. (6.2) reduces to the Brey-Fertig wavefunction used in Ref. [41, 42].

In m*GNR, when $k_{x,n} = 0$, the energy spectrum is $\epsilon = s\hbar\omega_0$, with $\omega_0 = \left[\omega_y^2 + \Omega_g^2\right]^{1/2}$, $\omega_{y_0} = 2\pi v_F/L_y$ and $\omega_y = v_F k_y = m\omega_{y0}$. In the Coulomb gauge for a region of constant potential ($\nabla\varphi = 0$), an electric field $\mathbf{E} = \hat{y}E_y \exp(-i\omega t)$ that turns on adiabatically at $t = -\infty$ gives rise to a vector potential $\mathbf{A} = \mathbf{E}/(i\omega)$. After making the Peierls substitution, $\mathbf{k}(\mathbf{k}') \rightarrow \mathbf{k}(\mathbf{k}') + e\mathbf{A}/\hbar$ into Eq. (6.1), we obtain a time dependent Hamiltonian H near the Dirac points of the m*GNR [10, 81]. The Fourier expansion of the resulting perturbation wavefunction is written:

$$\psi(\mathbf{r}, t; m) = \sum_{l=0}^{\infty} \psi_0(m, l) \exp[i \frac{\omega_y y}{v_F}] \exp[-i (\frac{\epsilon}{\hbar} + \omega l) t] \tag{6.4}$$

where m is the quantum number of k_y, l is the harmonic order of the electric field, and $\psi_0(m, l)$ is a spinor of order (m, l). Following the model of gapped 2D SLG [32] and our previous studies of ideal mGNR [10, 81], the THz third-order nonlinear conductance of finite-length, thin m*GNR, with an applied $\hat{y}$ linearly-polarized electric field, in the relaxation-free approximation, and no coupling to the spatial profile of the applied electric field, can be expanded as:

$$g_{y\nu}^{(3)}(\omega) = \sum_{l=1}^{2} \sum_{m} f_{y\nu}^{(\omega)}(\omega_0, \frac{\omega l}{2}) N_\Theta(\omega_0) \delta(\omega_0 - \frac{\omega l}{2}) \omega_{y0} \tag{6.5a}$$

$$g_{y\nu}^{(3)}(3\omega) = \sum_{l=1}^{3} \sum_{m} f_{y\nu}^{(3\omega)}(\omega_0, \frac{\omega l}{2}) N_\Theta(\omega_0) \delta(\omega_0 - \frac{\omega l}{2}) \omega_{y0} \tag{6.5b}$$

with the thermal factor in the presence of the gap Ω_g:

$$N_\Theta(\omega_0) = \frac{\sinh\left(\frac{\hbar v_F \omega_0}{k_B T}\right)}{\cosh\left(\frac{\hbar\Omega}{k_B T}\right) + \cosh\left(\frac{\hbar v_F \omega_0}{k_B T}\right)} \Theta(\omega_0 - \Omega_g) \tag{6.6}$$

where the Fermi level $E_F = \hbar\Omega$, $\nu = x$, y is the direction of the current component, and $f_{y\nu}^{(\omega_s)}(\omega_0, \frac{\omega l}{2})$ is the coefficient associated with the corresponding $\delta(\omega_0 - \frac{\omega l}{2})$ term in

the expansion of the expression for third-order conductance, and $\Theta(\omega)$ is the Heaviside step function.

After some algebra, the isotropic third-order conductances for infinitely long m*GNR from Eq. (6.5) are obtained:

$$\begin{aligned} g_{yy}^{(3)}(\omega) =& G\left(16,-4,-2\right)\left(1-4\gamma^2\right)^{-1/2} N_\Theta(\frac{\omega}{2}) \\ &+ G\left(0,-4,-1\right)\left(1-\gamma^2\right)^{1/2} N_\Theta(\omega) \end{aligned} \tag{6.7a}$$

$$\begin{aligned} g_{yy}^{(3)}(3\omega) =& G\left(-\frac{4}{3},\frac{1}{3},\frac{1}{2}\right)\left(1-4\gamma^2\right)^{-1/2} N_\Theta(\frac{\omega}{2}) \\ &+ G\left(0,-\frac{4}{3},-1\right)\left(1-\gamma^2\right)^{1/2} N_\Theta(\omega) \\ &+ G\left(-\frac{4}{3},\frac{5}{3},\frac{3}{2}\right)\left(9-4\gamma^2\right)^{-1/2} N_\Theta(\frac{3\omega}{2}) \end{aligned} \tag{6.7b}$$

where $G(z_2,z_1,z_0) = g_0\eta\eta_x\left(z_2\gamma^4+z_1\gamma^2+z_0\right)$, $g_0 = e^2/(4\hbar)$, $\eta_x = \left(g_s g_v v_F\right)/\left(\omega L_x\right)$, $\eta = \left(e^2E_0^2v_F^2\right)/(\hbar^2\omega^4)$ and $\gamma = \Omega_g/\omega$. Here $g_s = 2$ ($g_v = 2$) is the spin (valley) degeneracy. We note that in Eq. (6.7), the expression for the isotropic Kerr conductance contains terms due to both single-photon ($N_\Theta(\omega/2)$) and two-photon ($N_\Theta(\omega)$) transitions, and the expression for the isotropic third-harmonic conductance contains terms due to single-photon, two-photon, and three-photon ($N_\Theta(3\omega/2)$) transitions.

Similarly, the anisotropic third-order conductances for infinitely long m*GNR from Eq. (6.5) are expressed as:

$$g_{yx}^{(3)}(\omega) = G\left(0,0,1\right)\left(1-\gamma^2\right)^{1/2} N_\Theta(\omega) \tag{6.8a}$$

$$
\begin{aligned}
g_{yx}^{(3)}(3\omega) =& G\left(0, \frac{1}{3}, -\frac{1}{2}\right)\left(1-4\gamma^2\right)^{1/2} N_\Theta(\frac{\omega}{2}) \\
&+ G\left(0, -\frac{4}{3}, 1\right)\left(1-\gamma^2\right)^{1/2} N_\Theta(\omega) \\
&+ G\left(0, \frac{1}{3}, -\frac{1}{6}\right)\left(9-4\gamma^2\right)^{1/2} N_\Theta(\frac{3\omega}{2})
\end{aligned} \tag{6.8b}
$$

In Eq. (6.8), the expression for the anisotropic Kerr conductance contains only a term due to the two-photon ($N_\Theta(\omega)$) transition because the single-photon transition is not allowed due to the symmetry of the wavefunctions. However, the expression for the anisotropic third-harmonic conductance contains single-photon, two-photon, and three-photon terms.

Following Ref. [81,101–103], we employ a Gaussian broadening model to study the impact on the nonlinear conductance due to spectral broadening of m*GNR in the THz regime. We use the relaxation time $\tau = 25\,\text{ps}$ [88] for m*GNR, with the assumption τ remains a constant in the THz regime, invariant of the temperature and the applied field strength. We also introduce the illumination length L, characterizing the coupling between the spatial profile of the applied electric field and the energy spectrum [81] of the m*GNR. We use the Gaussian kernel, $Z_g(\omega_0, \omega) = \left(\sqrt{\pi}\,\Gamma_\omega\right)^{-1} \exp\left[-(\omega_0-\omega)^2/\Gamma_\omega^2\right]$, where $\Gamma_\omega = 2\pi\left(2\tau\sqrt{\ln 2}\right)^{-1}$ and $f_\Gamma = \Gamma_\omega/(2\pi) = 0.024\,\text{THz}$, to replace the Dirac delta function in Eq. (6.5). Using this framework, the third-order conductances for finite-length m*GNR are expressed as:

$$
\tilde{g}_{y\nu}^{(3)}(\omega, L_y, L, \Gamma_\omega) = \sum_{l=1}^{2}\sum_{m} \tilde{f}_{y\nu}^{(\omega)}(\omega_0, \frac{\omega l}{2}) Z_g(\omega_0, \frac{\omega l}{2})\omega_{y0} \tag{6.9a}
$$

$$
\tilde{g}_{y\nu}^{(3)}(3\omega, L_y, L, \Gamma_\omega) = \sum_{l=1}^{3}\sum_{m} \tilde{f}_{y\nu}^{(3\omega)}(\omega_0, \frac{\omega l}{2}) Z_g(\omega_0, \frac{\omega l}{2})\omega_{y0} \tag{6.9b}
$$

where $\tilde{f}_{y\nu}^{(\omega_0)}(\omega_0, \frac{\omega l}{2}) = f_{y\nu}^{(\omega)}(\omega_0, \frac{\omega l}{2}) N_\Theta(\omega_0) \operatorname{sinc}^2\left(\frac{\omega_0 L}{2v_F}\right)$. Our previous result reported in [81] exists as a special case of the current work with the assumption $\Omega_g \to 0$. Furthermore, when $f_\Gamma \to 0$, due to the local current density operator $qv_F\sigma_{x,y}\delta(\mathbf{r}-\mathbf{r_{op}})$ [10,32,52,81] used in this work, we assume graphene carriers at $\mathbf{r_{op}}$ interact only with the incoming photon field at $\mathbf{r_{op}}$. In this case, the third-order conductances calculated from Eq. (6.9) reduce to Eq. (6.5).

6.3 Results and Discussion

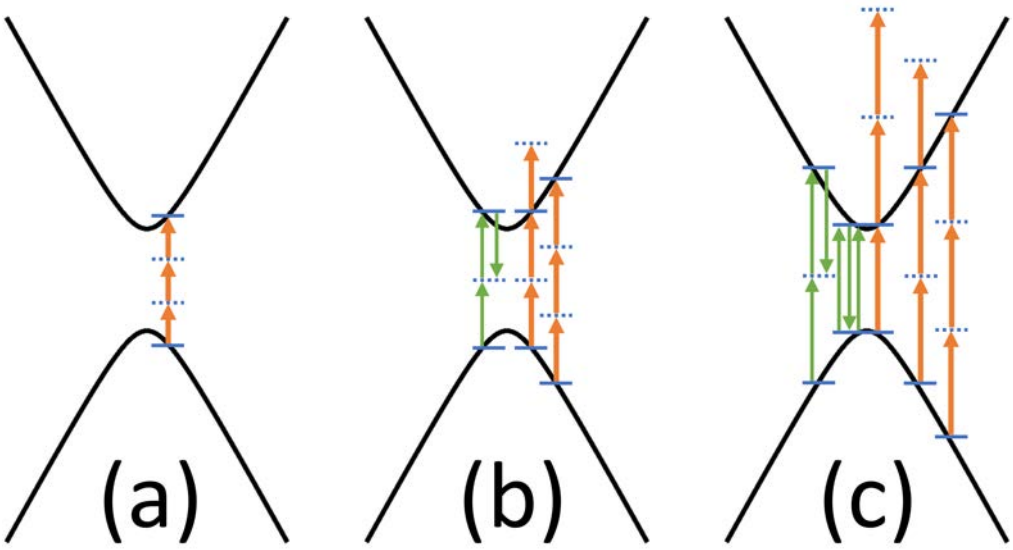

Figure 6.1: Direct interband transition for energetically-allowed third-order processes in intrinsic m*GNR: a) only the third-harmonic three-photon transition is allowed ($\Omega_g > \omega \geq 2\Omega_g/3$); b) third-harmonic two-photon and three-photon transitions are allowed and Kerr two-photon transition is allowed ($2\Omega_g > \omega \geq \Omega_g$); and c) third-harmonic single-photon, two photon, and three-photon transitions are allowed and Kerr single-photon and two-photon transitions are allowed ($\omega \geq 2\Omega_g$).

To simplify the discussion, we present results for m*GNR20 (acGNR of atomic width $N = 20$), and we neglect the effects of the spatial profile of the applied field on the nonlinear response ($L \to 0$), although the effect of the illumination length is multiplicative with the conductance, and so can be easily incorporated into our model if desired [81].

For all calculations, we assume an applied field strength $E_y = 50\,\mathrm{kV/m}$ and broadening parameter $f_\Gamma = 0.024\,\mathrm{THz}$ ($f_\Gamma \to 0$) for finite (infinite) length m*GNR. Further, we use the terms Kerr (third-harmonic) conductance to describe a conductance at ω (3ω) respectively and the terms isotropic (anisotropic) to describe a conductance parallel (orthogonal) to the direction of the applied THz electric field. In what follows, we summarize the characteristics of the nonlinear conductances for all combinations of the ribbon length L_y and Fermi level E_F, given in (6.9).

Fig. 6.1 illustrates the energetically-allowed transitions for various excitation frequency ranges [34] of infinite-length intrinsic m*GNR. For frequencies below the three-photon transition ($\omega < 2\Omega_g/3$), all third-order transitions are energetically prohibited. For frequencies above the three-photon transition but below the two-photon transition ($\Omega_g > \omega \geq 2\Omega_g/3$), Fig. 6.1a shows that only the three-photon component contributes to the third-harmonic conductance. Contributions to the Kerr conductance are energetically disallowed in this frequency range. For frequencies above the two-photon transition ($2\Omega_g > \omega \geq \Omega_g$), Fig. 6.1b shows that both two-photon and three-photon components contribute to the third-harmonic conductance, whereas for the Kerr conductance, only the two-photon component contributes. And finally, for

frequencies above the single-photon transition threshold ($\omega \geq 2\Omega_g$), single-photon, two-photon, and three-photon components contribute to the third-harmonic conductance, and two-photon and single-photon components contribute to the Kerr conductance. We emphasize here that although these components may be energetically allowed, some transitions are blocked due to the symmetry of the wavefunctions and therefore, do not contribute to the conductances (see Eqs. (6.7) and (6.8)). We discuss this point in more detail below.

Fig. 6.2 compares the isotropic and anisotropic third-order conductances for infinitely-long intrinsic mGNR20 and m*GNR20 as a function of excitation frequency. In contrast to mGNR, where electrons near the Dirac points behave like massless Dirac fermions, in m*GNR, particles in the low energy regime behave like massive Dirac fermions where the non-zero k_Δ term in Eq. (6.1) is the origin of the mass term in the energy spectrum.

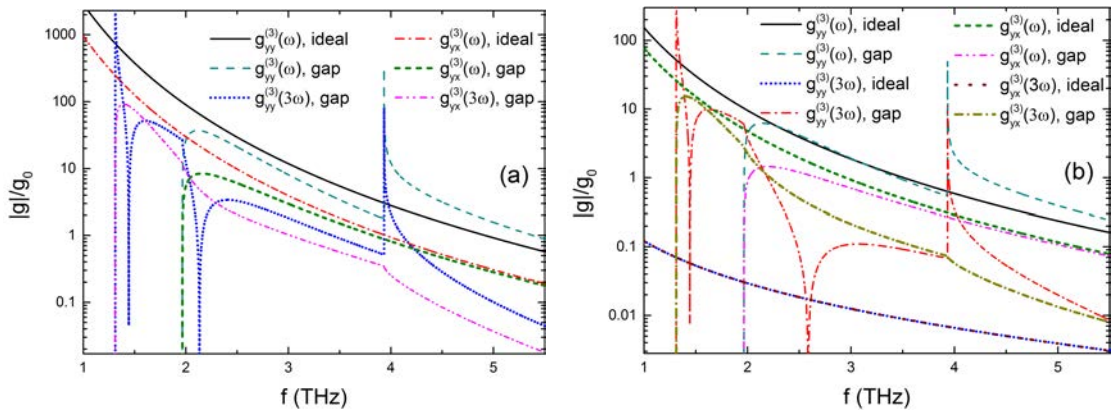

Figure 6.2: Magnitude of the isotropic and anisotropic third-order nonlinear conductances for infinitely-long intrinsic mGNR20 and m*GNR20 as a function of excitation frequency $f = \omega/(2\pi)$. a) $T = 0\,\mathrm{K}$; and b) $T = 300\,\mathrm{K}$. For all plots, the broadening parameter $f_\Gamma = 0$.

In Fig. 6.2a we plot the nonlinear conductances for $T = 0\,\mathrm{K}$. The gapped Kerr conductances are zero for $\omega < \Omega_g$ by virtue of energy conservation, as the two-photon transition is prohibited. Above this threshold, the gapped Kerr conductances are always smaller than their ideal counterparts. However, as the excitation increases further, we observe a second threshold with a sharp resonance in the isotropic Kerr conductance exactly at the gap energy $\omega = 2\Omega_g$. This is a result of the Van Hove singularity in the density of states at $2\Omega_g$. The anisotropic Kerr conductance does not exhibit a similar resonance. This difference in behavior is a result of the chiral nature of the m*GNR wavefunction. For excitation frequencies above the second threshold, the gapped Kerr conductances asymptotically approach their ideal counterparts for $\omega \gg 2\Omega_g$. Fig. 6.2b illustrates the behavior of the nonlinear conductances at room temperature where for the gapped Kerr conductances, qualitatively similar behavior to the $T = 0\,\mathrm{K}$ results is observed.

For the gapped third-harmonic conductances plotted in Fig. 6.2, the behavior is quite different from the Kerr conductances. The gapped third-harmonic conductances are zero for $\omega < 2\Omega_g/3$ due to energy conservation, as the three-photon transition is prohibited below this threshold. For $\omega \geq 2\Omega_g/3$, there are sharp resonances in the isotropic third-harmonic nonlinearity at $\omega = 2\Omega_g/2$ (three-photon resonance) and at $\omega = 2\Omega$ (single-photon resonance), again due to the Van Hove singularity at the band edge. As with the Kerr case discussed above, these resonances do not exist in the gapped anisotropic third-harmonic conductance curves as a result of the chirality. We also observe two antiresonances in the region above the three-photon threshold for the

gapped isotropic third-harmonic conductance. These antiresonances exist at both low and room temperatures. The antiresonance at $\sim 1.45\,\mathrm{THz}$ is a result of a zero-crossing in the $G(-4/3, 5/3, 3/2)$ polynomial of Eq. (6.7b) and is independent of temperature, whereas the antiresonance above $2\,\mathrm{THz}$ is a result of the (temperature dependent) cancellation of the $3\omega/2$ and ω terms in Eq. (6.7b). Finally, we observe that generally, the gapped third-harmonic conductances are significantly enhanced in magnitude when compared with their ideal counterparts. A similar enhancement of the isotropic third-order nonlinearity has also been predicted in gapped 2D graphene [32, 33].

In Fig. 6.3 we plot the magnitude of the isotropic and anisotropic third-order conductances for m*GNR as a function of nanoribbon length L_y and excitation frequency ω at $T = 0\,\mathrm{K}$. Figs. 6.3a and 6.3b show the gapped isotropic and anisotropic Kerr conductances respectively. The single-photon and two-photon resonances with the bandgap are clearly observable for the isotropic conductance. These resonances arise due to the state at $k_y = 0$ which does not change energy, and are absent in the anisotropic conductances due to wavefunction symmetry. For both isotropic and anisotropic Kerr conductances above the two-photon resonance ($\omega/\Omega_g \geq 1$), a series of peaks are observed as a function of L_y. These peaks correspond to the excitation frequency ω coming into and out of resonance with the quantized $k_y = 2\pi m/L_y$ states as the length of the nanoribbon varies. For values of ω quite close to the two-photon resonance, the period of the peaks as a function of L_y is large, due to the hyperbolic character of the energy spectrum near the band edge. As the excitation frequency increases, the period of the peaks in L_y decreases. Above the single-photon resonance

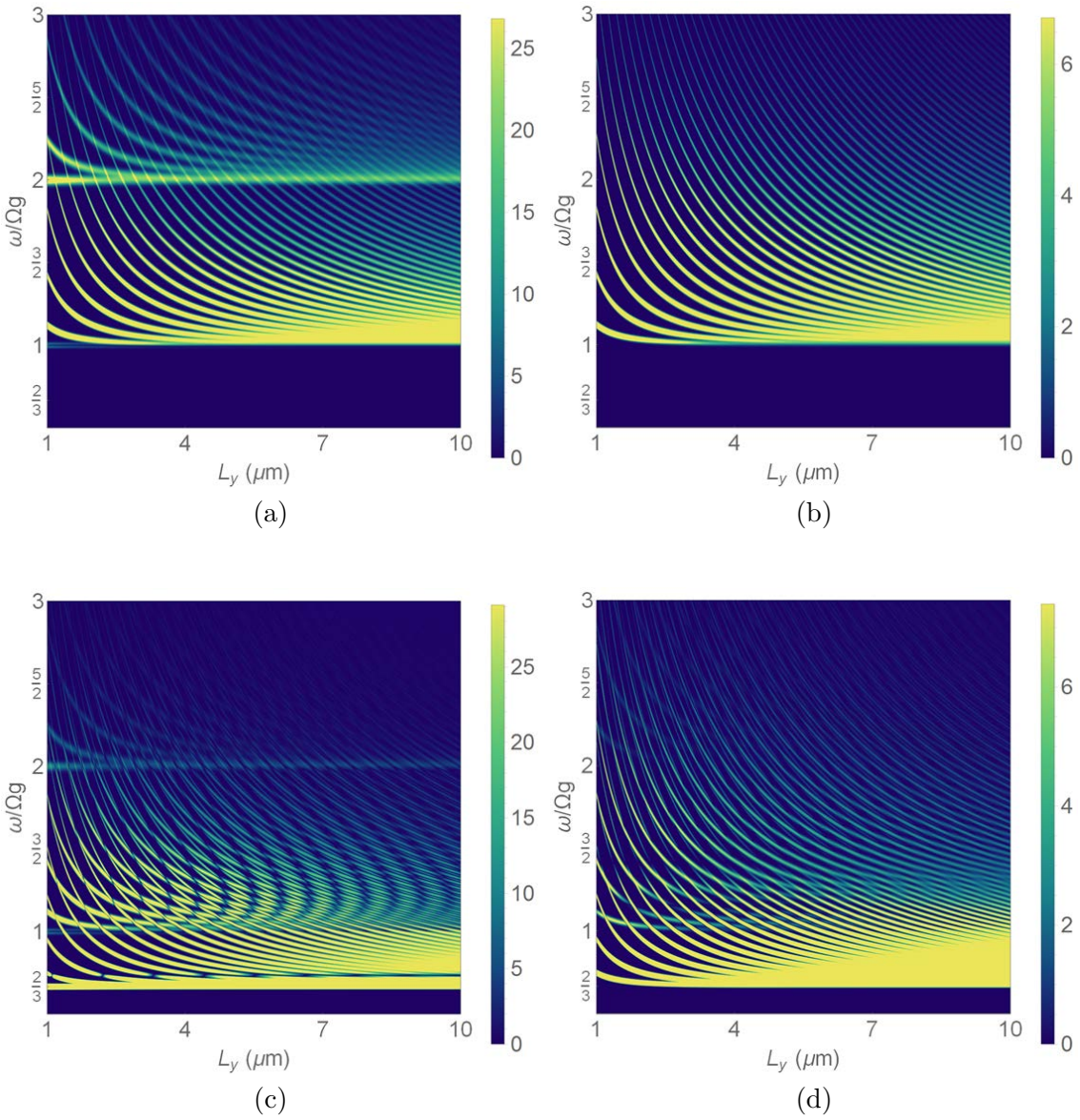

Figure 6.3: Amplitude of the isotropic and anisotropic third-order nonlinear conductances in intrinsic m*GNR as a function of the nanoribbon length L_y and the normalized excitation frequency ω/Ω_g: a) isotropic Kerr conductance; b) anisotropic Kerr conductance; c) isotropic third-harmonic conductance; and d) anisotropic third-harmonic conductance. For all plots, the broadening parameter $f_\Gamma = 0.024\,\mathrm{THz}$.

at $\omega/\Omega_g \geq 2$, the gapped isotropic conductance displays peaks with both large and small periods in L_y due to the presence of both single-photon and two-photon terms in the expression for the conductance. The isotropic conductance peaks display a more complex behavior due the fact that both resonances contribute to the conductance peaks through the $\omega/2$ and ω terms in the expression for the conductance. The anisotropic Kerr conductance exhibits a response due only to the two-photon transition. Due to the symmetry of the wavefunctions, the contribution from the single-photon transition is three orders of magnitude or more below the contribution from the two-photon transition when broadening is included in the model, and is not allowed in the relaxation-free approximation. As a result, only the two-photon transition contributes significantly to the conductance. Finally, as $L_y \to \infty$, the peak period shortens and the conductance converges to a smooth curve as the quantized k_y states form a continuum.

Figs. 6.3c and 6.3d illustrate similar behavior for the third-harmonic conductances, with single-photon, two-photon, and three-photon resonances visible for the gapped isotropic conductance and a superposition of various peak periods due in general to contributions from each of the resonances for the conductances as a function of L_y for a particular frequency. The universal antiresonance discussed above for the isotropic third-harmonic conductance is clearly-observable in this plot as well.

In Fig. 6.4 we plot the Fermi-level dependence of the ideal ($L_y \to \infty$) extrinsic gapped third-order conductances at $T = 0\,\mathrm{K}$. As the magnitude of the Fermi level increases, the nonlinear conductances exhibit a thresholding behavior that results from

state blocking. Fig. 6.4a shows the contributions from the $\omega/2$ and ω terms for the gapped isotropic Kerr conductance; Fig. 6.4b shows that for the gapped anisotropic Kerr conductance, only the ω term contributes; Figs. 6.4c and 6.4d show that for the gapped isotropic and anisotropic third-harmonic conductances, the $\omega/2$, ω, and $3\omega/2$ terms all contribute.

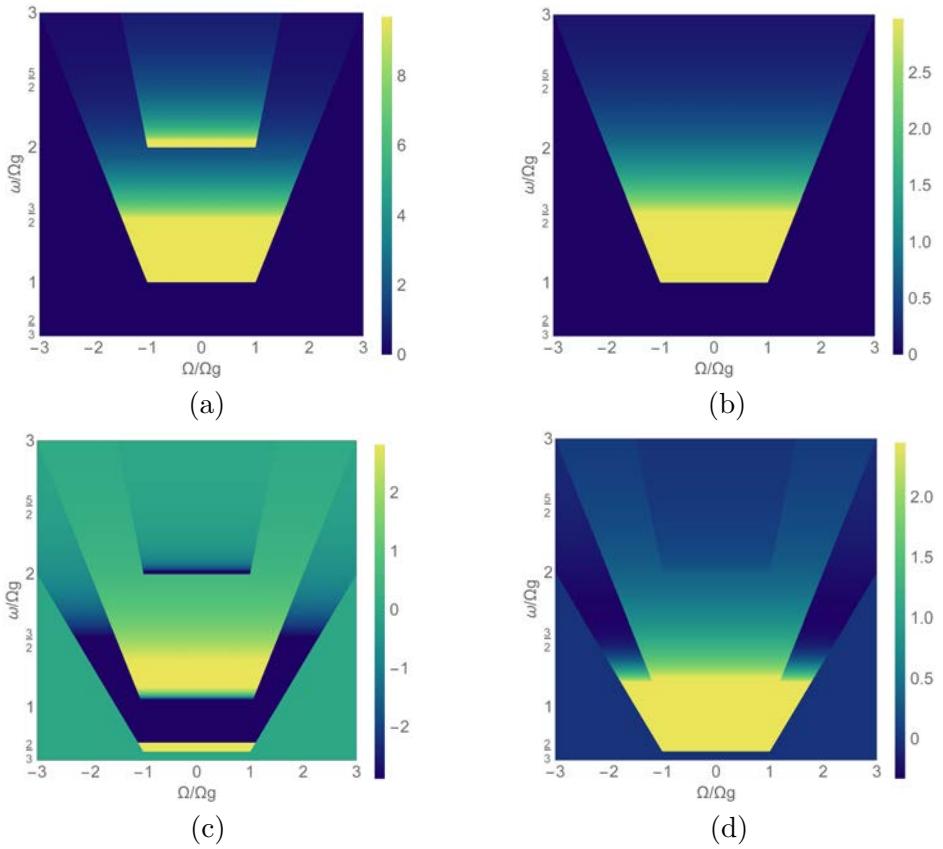

Figure 6.4: Amplitude of the third-order conductances (A.U.) of m*GNR at $T = 0\,\mathrm{K}$ as a function of the normalized Fermi level Ω/Ω_g and normalized frequency ω/Ω_g: a) isotropic Kerr conductance; b) anisotropic Kerr conductance; c) isotropic third-harmonic conductance; and d) anisotropic third-harmonic conductance. For all plots, $L = 0$ and $\Gamma_\omega = 0$.

These thresholds may be determined using the following expression:

$$\frac{\omega}{\Omega_g}\Theta\left(\frac{\omega}{\Omega_g}-\frac{2}{l}\right)=\frac{2}{l}\left|\frac{\Omega}{\Omega_g}\right| \tag{6.10}$$

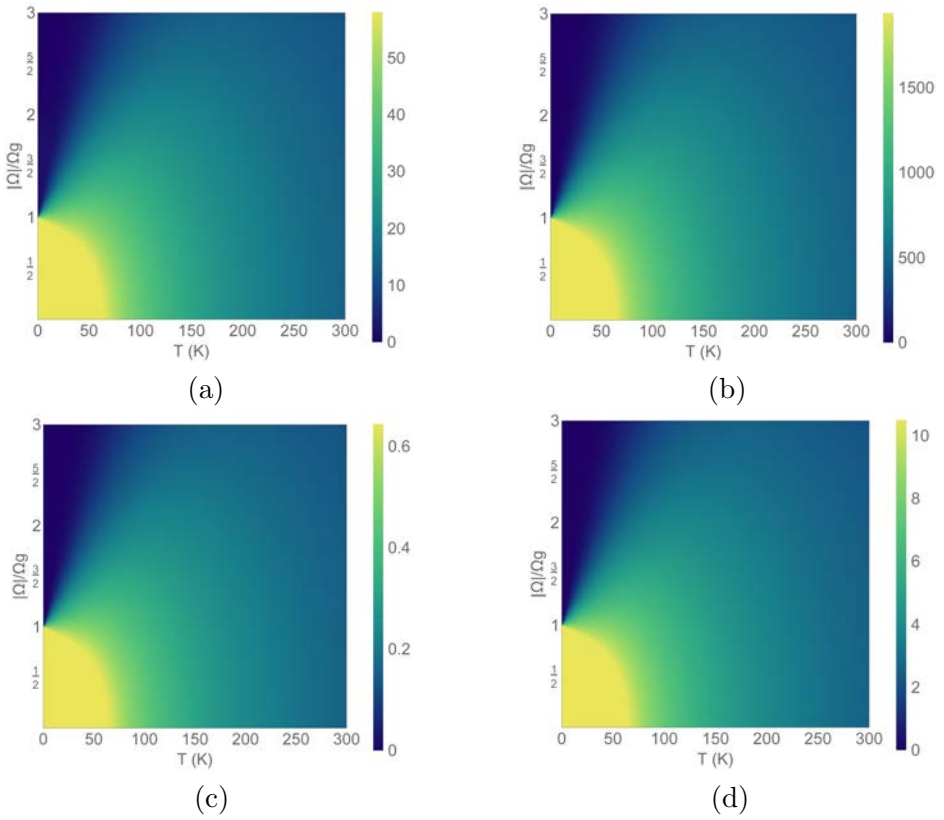

Figure 6.5: Density plot of of the third-order conductance of gapped mGNR as a function of Ω and T. The magnitude are A.U. a) $-g_{yy}^{(3)}(2\Omega_g)$, b) $-g_{yy}^{(3)}(2\Omega_g/3)$, c) $g_{yx}^{(3)}(\Omega_g)$, and d) $g_{yx}^{(3)}(2\Omega_g/3)$. For all plots, $L=0$, and $\Gamma_\omega \to 0$.

In order to optimize the nonlinear conductance enhancement for the third-order conductance for gapped mGNR under all temperature, we plot the temperature and Fermi level dependences on the gapped mGNR for various pumping frequency in Fig. 6.5. In the interest of brevity, we only show the following pump

frequencies for third-order conductance, $\omega = 2\Omega_g(\Omega_g)$ for the isotropic (anisotropic) Kerr-conductance, and $\omega = 3\Omega_g/2$ for the isotropic (anisotropic) third-harmonic conductance. The following features can be observed: (i) hot spots for $\Omega < \Omega_g$ at low temperature; (ii) cold belts for $\Omega > \Omega_g$ at low temperature; and (iii) a diffusive region for all Ω at high temperature. For feature (i), the hot spots are a direct consequence of the low temperature enhancement of the gapped nonlinear conductance at the resonance frequency of the energy gap. Such a feature is also observed in Figs. 6.2 and 6.4 and agrees with Ref. [32, 33] for the interband transition of gapped 2D SLG. For feature (ii), the cold belts are in the forbidden region as indicated in Fig. 6.4 since there is no allowed state that can make the direct interband transition in the belts region. For feature (iii), the diffusive region is the direct result of the behavior of the thermal factor at higher temperature. Deeper charge carriers can be involved in the optical absorption in the forbidden region $\Omega \geq \Omega_g$ at 0 K due to the availability of higher thermally evacuated states [32]. Thus for higher temperature, we see the conductance increases for $\Omega \geq \Omega_g$. Furthermore, at high temperature, due to the thermal broadening for the massive Dirac fermions near the conduction and valence band edges, the Van Hove singularity at low temperature becomes weaker [10,32], and we see the conductance declines for $\Omega \leq \Omega_g$ at higher temperature. In summary, from Fig. 6.5, we propose that the optimum choice of Fermi level is for $\Omega = E_F/\hbar \leq \ \Omega_g$.

Fig. 6.6 illustrates the overall impact of the effects we have discussed above on the magnitude of the third-order Kerr and third-harmonic conductances. In Figs. 6.5a ($T = 0\,\mathrm{K}$) and 6.6b ($T = 300\,\mathrm{K}$), we plot the isotropic Kerr and third-harmonic

conductances for several values of nanoribbon length L_y as a function of excitation frequency. The curves exhibit signatures that depend strongly on the allowed transitions and polynomial amplitudes that contribute to each conductance component.

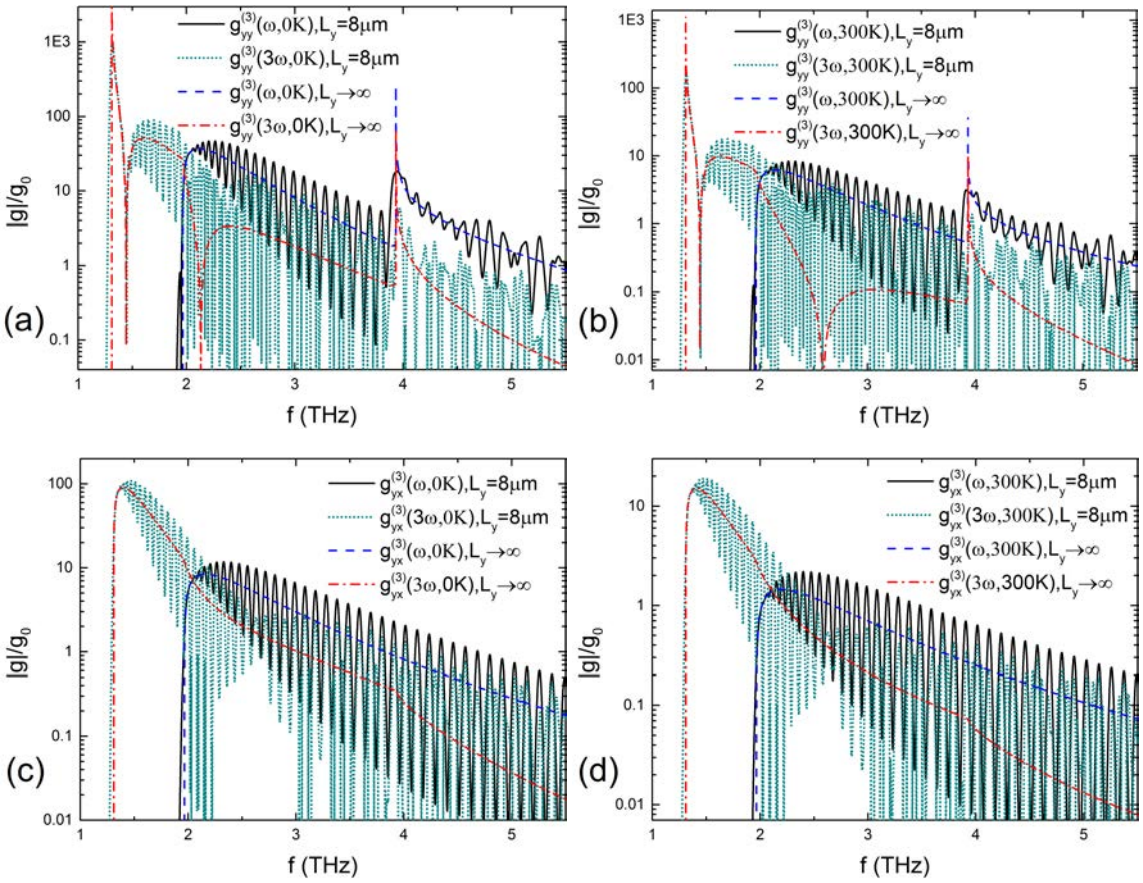

Figure 6.6: Magnitude of the third-order nonlinear conductances in m*GNR20 for various ribbon length and temperatures as a function of excitation frequency $f = \omega/2\pi$: a) isotropic Kerr and third-harmonic conductances at $T = 0\,\mathrm{K}$; b) isotropic Kerr and third-harmonic conductances at $T = 300\,\mathrm{K}$; c) anisotropic Kerr and third-harmonic conductances at $T = 0\,\mathrm{K}$; and d) anisotropic Kerr and third-harmonic conductances at $T = 300\,\mathrm{K}$. For all plots, the Fermi level $\Omega/2\pi = 1\,\mathrm{THz}$ and broadening parameter $f_\Gamma = 0.024\,\mathrm{THz}$ ($f_\Gamma = 0$) for finite (infinite) length m*GNR20.

For example, the antiresonance at $f = \omega/2\pi = 1.465\,\mathrm{THz}$ in the third-harmonic conductance results from the zero in the polynomial $G(-4/3, 5/3.3/2)$ that appears in the expression for the three-photon term in the third-harmonic conductance Eq. (6.7b). This antiresonance is universal (not temperature or length dependent) and can also be observed in Figs. 6.2 and 6.3c. There is also a second antiresonance that exists in the $L_y \to \infty$ third-harmonic conductance above the two-photon threshold that is temperature dependent. This antiresonance is a result of the exact cancellation of the two-photon and three-photon terms in Eq. (6.7b), and is temperature-dependent due to the different thermal factors present in each term. For finite L_y the exact cancellation does not occur, and we do not observe this antiresonance in the third-harmonic conductance.

The oscillations present in both the Kerr and third-harmonic conductances as a function of L_y result from the discrete states in $k_y = 2\pi m/L_y$ moving in and out of resonance with the excitation frequency $f = \omega/2\pi$ as the length changes. For excitation frequencies above the three-photon threshold but below the two-photon threshold ($\Omega_g > \omega \geq 2\Omega_g/3$), the oscillation period lengthens smoothly as a function of excitation frequency in a manner consistent with the results presented in Fig. 6.3c. Above the two-photon threshold ($2\Omega_g > \omega \geq \Omega_g$), the oscillations in the third-harmonic conductance are more complex, resulting from the interference due to the superposition of both the three-photon and two-photon conductance components. Above the single-photon threshold ($\omega \geq 2\Omega_g$), the third-harmonic conductance oscillations are even more complex, resulting from interference between the three-photon,

two-photon, and single-photon components of the conductance. Such behavior is also consistent with the results presented in Fig. 6.3c.

Oscillatory behavior similar to that described above is observed in all four third-order conductance components. The anisotropic third-harmonic conductance component exhibits the same three qualitatively distinct regimes as does the isotropic third-harmonic conductance. The isotropic Kerr conductance exhibits two oscillation regimes for frequencies above the two-photon and single-photon thresholds. However, due to the chiral symmetry of the wavefunctions, for the anisotropic Kerr conductance, the contribution from the single-photon transition is at least three orders of magnitude below the contribution from the two-photon transition when broadening is included in the model, and is not allowed in the relaxation-free approximation. As a result, only the two-photon transition contributes significantly to the conductance in this case as well.

It is also useful to point out here that, for a given excitation frequency, it should be possible to engineer the band gap and Fermi level, together with the applied field spatial profile to shift away the antiresonances in the third-harmonic conductance [81]. The band gap may also be tuned by changing terminations or by slightly twisting the ribbon [28].

6.4 Conclusion

In conclusion, we have calculated the third-order THz conductances in gapped extrinsic and intrinsic m*GNR using a time-dependent perturbation analysis of the

$\mathbf{k} \cdot \mathbf{p}$ model. Generally, the nonlinear conductances exhibit contributions due to single-photon, two-photon, and three-photon processes. The interference between each of these processes results in remarkably complex behavior for the third-order conductances, including quantum dot signatures that should be measurable with a relatively simple experimental configuration. Notably, we observe sharp resonances in the isotropic third-order response of m*GNR with infinite length due to the Van Hove singularities in the density of states at one-, two-, and three-photon resonances, and similar resonances for m*GNR of finite length due to the fixed state at $k_y = 0$. However, these resonances are absent in the anisotropic third-order response; a result of the overall symmetry of the system. We also map the amplitude of the third-order conductances as a function of Fermi level and bandgap, and determine a general expression for their existence thresholds in the presence of state blocking.

The successful synthesis of ultrathin acGNR with widths $L_x < 10\,\text{nm}$ [48, 49] suggest that experimental measurement of the THz nonlinear response in thin m*GNR in the ballistic and quasi-ballistic regimes should be possible at relatively low excitation field strengths with response in some cases greater than that predicted for ideal mGNR. Our results indicate that m*GNR may provide the basis for developing a variety of useful THz devices over a wide range of temperatures and that by careful design of the gap energy (which is a function of m*GNR width), the nonlinear response may be optimized for a particular desired excitation frequency range.

CHAPTER 7
NONLINEAR THZ RESPONSE OF METALLIC ARMCHAIR GRAPHENE SUPERLATTICES

[1] In this chapter, we study third-order THz nonlinear response of metallic armchair graphene nanoribbon superlattices in the presence of an elliptically-polarized excitation field using time dependent perturbation theory. For a one-dimensional Kronig-Penney potential of infinite length, the nonlinear response can be described perturbatively by a low energy $\mathbf{k}\cdot\mathbf{p}$ N-photon coupling model. Remarkably, as shown by Burset *et.al.* [35], the energy dispersion of the metallic band in the direction parallel to the superlattice wavevector is independent of the applied superlattice potential while the energy dispersion in the direction perpendicular to the superlattice wavevector depends strongly on the superlattice parameters. As a result, we predict novel behavior for the nonlinear response of single layer metallic acGNR superlattices to an applied elliptically-polarized electric field. Our work shows that the superlattice potential, periodicity, Fermi level, excitation field polarization state, and temperature all play a significant role in the resulting THz nonlinear conductances.

7.1 Introduction

Graphene is a 2D honeycomb lattice arrangement of tightly packed carbon atoms. The unique properties of the quasiparticles near the Dirac points are governed by a massless Dirac Hamiltonian. The Dirac fermions near the Dirac points have very

[1]This chapter has been submitted for publication.

interesting properties, such as linear band dispersion, traveling with a high isotropic Fermi velocity and an easily tunable Fermi level, lead to the strong THz nonlinear response in 2D graphene structures [6–8, 17–21, 52, 65, 68, 69, 73].

Graphene superlattices may be fabricated via a variety of methods [119–124]. Design of graphene superlattice structures permit tailoring the graphene band structure and transport properties [35,125,126], leading to novel features, *e.g.* the effective group velocity parallel to the 1D cosine or Kronig-Penney (KP) potential can be distorted [35, 125–128], new Dirac points and lines may emerge [35, 124–128], Landau level splitting may occur [124], and finally group velocity modification due to a finite superlattice potential [128] and ratchet effects [122] may occur.

In general, graphene nanoribbons (GNR) have two different types of edges: armchair GNR (acGNR) and zigzag GNR (zzGNR). Theses two types of GNR show distinct electronic properties near the Dirac points [39, 41, 42]. The linear and nonlinear response of GNR due to a variety of elliptically-polarized excitation fields were investigated [9, 10, 75, 76, 81, 82, 114, 115]. Prior to the current work, only the nonlinear optical response of 2D graphene superlattices to a linearly-polarized excitation field have been investigated [51, 129] and there has been no investigation of the THz nonlinear response in metallic acGNR superlattice (mGNRsl) structures.

Most recently, thin (sub-20 µm) GNRs fabricated experimentally exhibit ultra smooth edges (not dominated by defects), high mobility, and ballistic transport [4, 22, 48, 49], and as a result may be treated as quasi-1D quantum wires. Further, graphene based nonlinear superlattice detectors are among the fastest detectors for excitation

frequencies ranging from THz up through ultraviolet. They are suitable for detection of intense sources and exhibit the attractive combination of sensitivity and speed up to room temperature [130]. Thus it is natural to investigate the nonlinear response of of thin mGNRsl structures to THz excitation fields.

In this chapterz, we describe new results on the nonlinear response of infinitely-long intrinsic and extrinsic thin mGNRsl excited by a normally-incident, elliptically-polarized THz electric field. We limit our work to superlattices with wavevectors parallel to the longitudinal axis of the nanoribbon, as well as THz photon energies and superlattice parameters that do not result in the creation of additional Dirac points [35]. In this limit, the band structure for the lowest metallic subbands in thin mGNRsl are independent of the superlattice parameters [35], which is quite different than the anisotropic band structure in 2D single layer graphene superlattice. *Most significantly*, we show that for the superlattice, Fermi level, polarization state and temperature all play an important role in determine the THz nonlinear response in infinitely-long mGNRsl.

7.2 Model

We consider mGNR with an applied 1D Kronig-Penney potential potential $V_(y) = V(y+d)$, and $V(y) = V_0 \mathrm{sgn}(y - d/2)|$ for $|y| < d$. According to [35], the transport near the Dirac point may be quantitatively described in the $\mathbf{k} \cdot \mathbf{p}$ approximation by the effective group velocity $v_x = \lambda v_F$ and $v_y = v_F$ where:

$$\lambda = \mathrm{sinc}(\tilde{V}) = \mathrm{sinc}\left[V_0 d / \left(2\hbar v_F\right)\right] \tag{7.1}$$

However, when $\tilde{V} \geqslant \pi$, new Dirac points emerge in the energy spectrum and the $\mathbf{k}\cdot\mathbf{p}$ model is no longer quantitatively valid [35]. As a result, in this chapterz we focus on the $\tilde{V} < \pi$ regime.

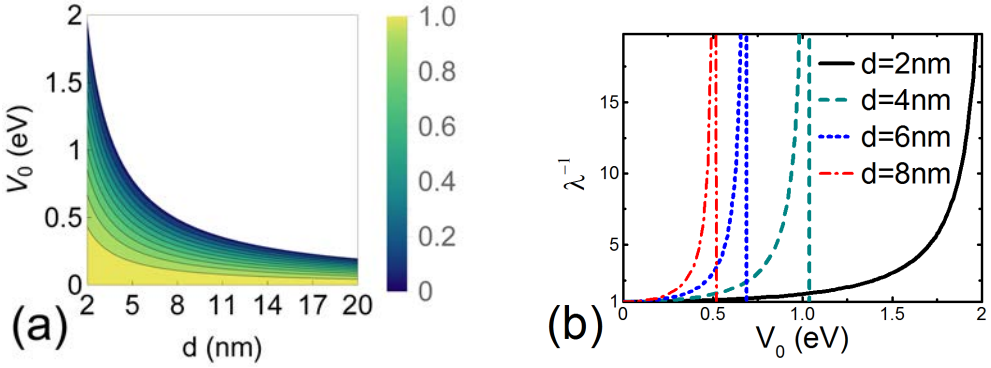

Figure 7.1: Design limits imposed by requiring that $\tilde{V} \leq 3$; a) relationship between d and V_0, and b) relationship between V_0 and λ^{-1}.

We begin with the unperturbed Hamiltonian for the mGNRsl in the form [35,41,42]:

$$H_0 = \hbar \begin{pmatrix} \boldsymbol{v_g}\cdot\mathbf{k} & 0 \\ 0 & \boldsymbol{v_g}\cdot\mathbf{k}' \end{pmatrix} \tag{7.2}$$

with $\boldsymbol{v_g} = v_x\sigma_x\hat{\mathbf{x}} + v_y\sigma_y\hat{\mathbf{y}}$, $\mathbf{k}(\mathbf{k}') = k_n(-k_n)\hat{\mathbf{x}} + k_y\hat{\mathbf{y}}$, $k(k') = \left(k_n^2 + k_y^2\right)^{1/2}$, and $\theta_n = \tan^{-1}(k_n/k_y)$. The energy dispersion is $\epsilon = s\hbar\left[v_y^2k_y^2 + v_x^2k_n^2\right]^{1/2}$. With $p_g = v_yk_y - iv_xk_n$, the wavefunction of mGNRsl is written:

$$\psi_{n,s} = \frac{\exp(ik_yy)}{(4L_xL_y)^{1/2}} \begin{pmatrix} \exp\left(ik_nx\right)p_g/|\epsilon| \\ s\,k\exp(ik_nx) \\ -\exp\left[\text{-}i\left(k_nx\right)\right]p_g/|\epsilon| \\ s\,k\exp(\text{-}ik_nx) \end{pmatrix} \tag{7.3}$$

We note that Eq. (7.3) reduces to the wavefunction for acGNR in the absence of the superlattice potential ($\lambda = 1$). We consider excitation frequencies well below the optical phonon energy in graphene ($\omega/2\pi \leqslant 6.67\,\text{THz}$) and assume the contributions

from the direct interband transition to the linear and nonlinear response are solely from the lowest band $k_{x,n} = 0$ for thin ($L_x \lesssim 20\,\text{nm}$) mGNRsl. Fig. 7.1 illustrates the design limits obtained by requiring that $\tilde{V} \leqslant 3$, or equivalently $1 \leqslant \lambda^{-1} \leqslant 20$ for $L_x = 20a_0/2$ wide mGNRsl (mGNRsl20).

The THz elliptically-polarized pump field incident on the mGNRsl may be generated by passing a THz $\hat{y}$-polarized electric harmonic field through a cascade of a half-wave plate, with its fast axis at an angle ϕ with respect to the $\hat{y}$ axis, and a quarter-wave plate oriented with its principle axes parallel and perpendicular to the Kronig-Penney potential. We assume the THz elliptically-polarized field is switched on adiabatically at $t_0 = -\infty$. In the Coulomb gauge for a source-free region ($\nabla\varphi = 0$), the THz elliptically-polarized field may be written in the Jones representation as $\mathbf{E} = E_0\left[i\hat{x}\sin(\phi) + \hat{y}\cos(\phi)\right]\exp(-i\omega t)$, giving rise to a magnetic vector potential $\mathbf{A} = \mathbf{E}/(i\omega)$. Following the N-photon coupling perturbation approach [10, 51, 52, 81] and making the substitution $\mathbf{k}(\mathbf{k}') \rightarrow \mathbf{k}(\mathbf{k}') + q\mathbf{A}/\hbar$, we obtain a time and polarization-state dependent Hamiltonian H near the Dirac points of the mGNRsl. The perturbed wavefunction is written:

$$\Psi(\mathbf{r}, t; m) = \sum_{l=0}^{\infty} \psi(m, l)\exp[i\frac{2m\pi}{L_y}y]\exp[-i(\frac{\epsilon}{\hbar} + \omega l)t] \tag{7.4}$$

where m is the quantum number of k_y, l is the harmonic order of the electric field, and $\psi(m, l)$ is a spinor of order (m, l). In mGNRsl, for $k_{x,n} = 0$, the dispersion of the energy spectrum is written $\epsilon = s\hbar|\omega_y|$. With $\omega_{y_0} = 2\pi v_y/L_y$, $\omega_y = m\omega_{y0}$ and the superlattice response function $f(\phi, \alpha, \beta, \lambda) = 2\cos(\phi)\left[\alpha\cos^2(\phi) - \lambda\beta\sin^2(\phi)\right]$, in the relaxation free approximation with no coupling to the spatial profile of the

applied THz excitation field, the longitudinal Kerr and third-harmonic conductances in infinitely-long mGNRsl become:

$$\frac{g_y^{(3)}(\omega,\phi,\lambda)}{-g_0\eta\eta_x} = f(\phi,1,-1,\lambda)N\left(\frac{\omega}{2}\right) + \frac{1}{2}f(\phi,1,-3,\lambda)N(\omega) \tag{7.5a}$$

$$\frac{g_y^{(3)}(3\omega,\phi,\lambda)}{g_0\eta\eta_x} = \frac{1}{24}f(\phi,6,1,\lambda)N\left(\frac{\omega}{2}\right) - \frac{1}{6}f(\phi,3,-5,\lambda)N(\omega) + \frac{1}{8}f(\phi,2,-7,\lambda)N\left(\frac{3\omega}{2}\right) \tag{7.5b}$$

and the transverse third-order conductances are:

$$\frac{g_x^{(3)}(\omega,\phi,\lambda)}{g_0\eta\eta_x} = \frac{\lambda}{2}f(\phi,1,1,\lambda)N(\omega) \tag{7.6a}$$

$$\frac{g_x^{(3)}(3\omega,\phi,\lambda)}{-g_0\eta\eta_x} = \frac{\lambda}{24}f(\phi,6,5,\lambda)N\left(\frac{\omega}{2}\right) - \frac{\lambda}{6}f(\phi,3,-1,\lambda)N(\omega) + \frac{\lambda}{8}f(\phi,2,-7,\lambda)N\left(\frac{3\omega}{2}\right) \tag{7.6b}$$

with the thermal factor defined as:

$$N(\omega_y) = \frac{\sinh\left(\frac{\hbar|\omega_y|}{k_BT}\right)}{\cosh\left(\frac{E_F}{k_BT}\right)+\cosh\left(\frac{\hbar|\omega_y|}{k_BT}\right)} \tag{7.7}$$

and with quantum conductance $g_0 = e^2/(4\hbar)$, Fermi level $E_F = \hbar\Omega$, gain factor $\eta_x = (g_s g_v v_F)/(\omega L_x)$, and coupling strength $\eta = (e^2E_0^2v_F^2)/(\hbar^2\omega^4)$. Finally, we note that the even-order conductances are zero due to the symmetry inherent in mGNRsl.

7.3 Results and Discussion

To simplify the discussion, we choose an applied field strength $E_0 = 10\,\mathrm{kV/m}$. Further, we use the relaxation free approximation for mGNRsl20 of infinite length and we neglect the effects of the spatial profile of the applied field on the nonlinear response [81]. From Eqs. (7.5) and (7.6), we see that illumination of an intrinsic, infinitely-long mGNRsl by a THz harmonic electric field results in a nonlinear response that is strongly dependent on the polarization state of the applied field.

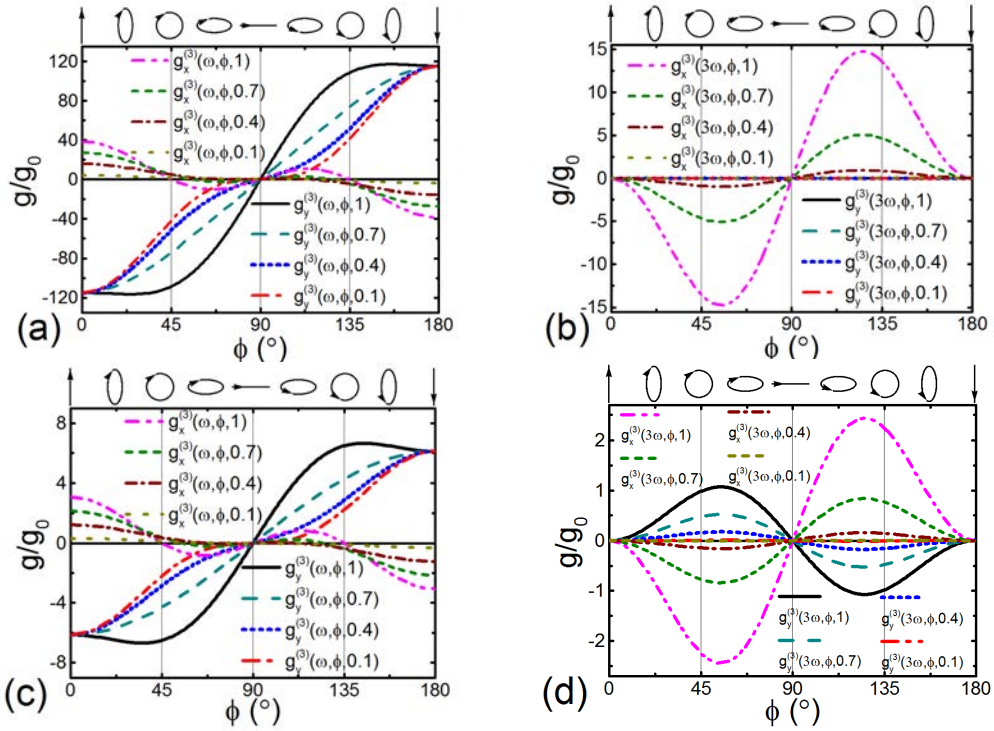

Figure 7.2: Magnitude of the third-order conductances at $f = \omega/2\pi = 1\,\mathrm{THz}$ for intrinsic mGNRsl20 for various values of λ as a function of the polarization ellipse angle ϕ; a) longitudinal Kerr conductance at $T = 0\,\mathrm{K}$, b) longitudinal third-harmonic conductance at $T = 0\,\mathrm{K}$, c) transverse Kerr conductance at $T = 300\,\mathrm{K}$, and d) transverse third-harmonic conductance at $T = 300\,\mathrm{K}$. For all plots $E_0 = 10\,\mathrm{kV/m}$.

Fig. 7.2 illustrates the polarization dependence of the longitudinal and transverse third-order nonlinear conductances at $T = 0\,\mathrm{K}$ and $300\,\mathrm{K}$ for intrinsic infinitely-long mGNRsl20 with varying λ. For the linearly polarized case, we have $g_x^{(3)}(\omega_0, 0, \lambda) = \lambda g_x^{(3)}(\omega_0, 0, 1)$. On the other hand, due to the fact that for the lowest metallic band, the energy dispersion $\epsilon = s\hbar|\omega_y|$ is independent of the superlattice parameter λ and has an effective group velocity $v_y = v_F$, the longitudinal third-order conductance $g_y^{(3)}(\omega_0, 0, \lambda)$ does not change from the non-superlattice result. In summary, due to the effective group velocity scaling $v_x = \lambda v_F$, $g_x^{(3)}(\omega_0, 0, \lambda)$ scales with λ as discussed above and is in agreement with the analysis of Ref. [35] for acGNR superlattices. For a general elliptically-polarized field ($\phi \neq 0°$, $90°$), we see that the longitudinal third-order conductance $g_y^{(3)}(\omega_0, \phi, \lambda)$ depends on the superlattice parameter only through the superlattice response function $f(\phi, \alpha, \beta, \lambda)$, and the transverse third-order conductance $g_x^{(3)}(\omega_0, \phi, \lambda)$ depends on λ through both the coefficients multiplying each term in the expression for the conductance as well as the superlattice response function $f(\phi, \alpha, \beta, \lambda)$.

Fig. 7.3 illustrates the dependence of the longitudinal and transverse third-order conductances on temperature and superlattice parameter λ for the set of three Fermi levels $\Omega/2\pi = 0.2\,\mathrm{THz}$, $0.7\,\mathrm{THz}$, and $1.2\,\mathrm{THz}$. Generally, the lowest Fermi level in this set allows single-, two-, and three-photon transitions at low temperature if present in Eqs. (7.5) and (7.6), the intermediate Fermi level blocks the single-photon transition at low temperature, and the high Fermi level blocks both single- and two-photon transitions at low temperature. For the longitudinal Kerr conductance (Figs.

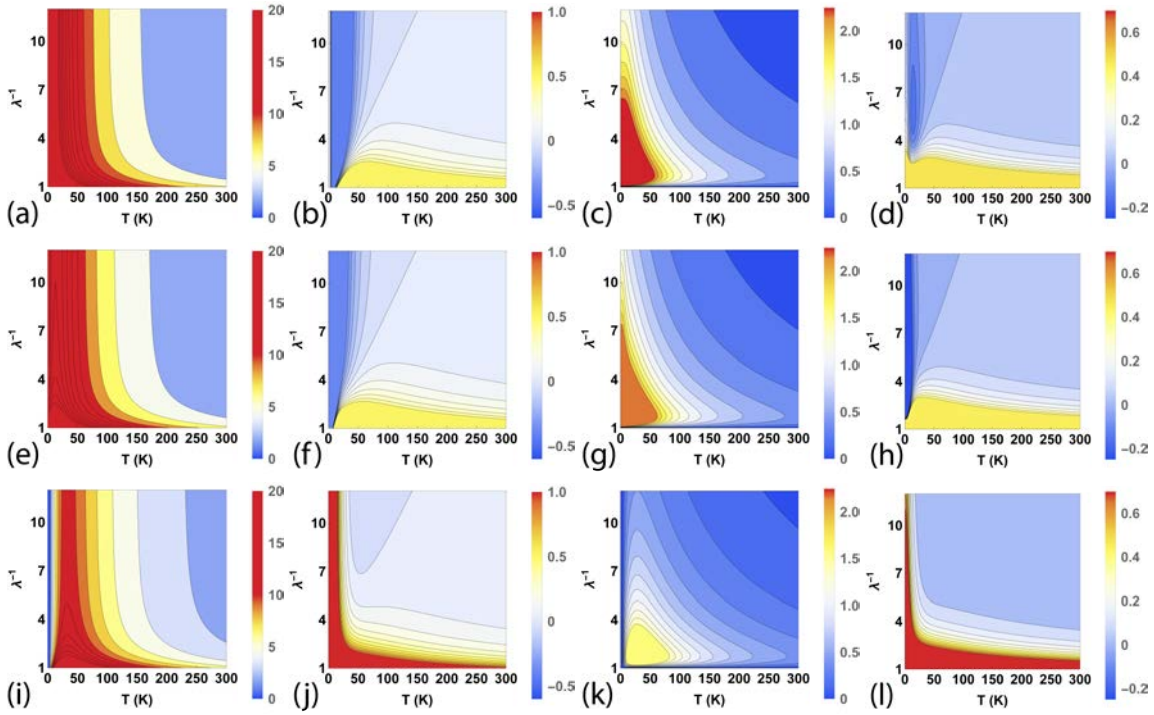

Figure 7.3: Amplitude of the third-order conductances excited with a circularly-polarized field as a function of temperature and superlattice parameter λ for various values of the Fermi level; a-d) $\Omega/2\pi = 0.2\,\mathrm{THz}$, e-h) $\Omega/2\pi = 0.7\,\mathrm{THz}$, and i-l) $\Omega/2\pi = 1.2\,\mathrm{THz}$. Panels a), e) , and i) show the longitudinal Kerr conductance, $-g_y^{(3)}(\omega, 45°, \lambda)$; panels b), f), and j) show the longitudinal third-harmonic conductance, $g_y^{(3)}(3\omega, 45°, \lambda)$; panels c), g), and k) show the transverse Kerr conductance, $g_x^{(3)}(\omega, 45°, \lambda)$; and panels d), h), and l) show the transverse third-harmonic conductance, $-g_x^{(3)}(3\omega, 45°, \lambda)$. $E_0 = 10\,\mathrm{kV/m}$ and $f = \omega/2\pi = 1\,\mathrm{THz}$ for all plots.

7.3a, 7.3e and 7.3i), we note that for a fixed superlattice parameter λ, the peak of the nonlinearity shifts to higher temperature as the Fermi level is increased and that the nonlinearity decays with temperature as expected. For the longitudinal third-harmonic nonlinearity, the single-photon term in Eq. (7.5b) is small relative

to the two-photon term, and as a result there is not a significant change between Figs. 7.3b and 7.3f. Blocking the two-photon term (Fig. 7.3j) eliminates the sign change that is manifest at lower Fermi levels. Eq. (7.6a) contains only a two-photon term and as a result, there are only minor differences between Figs. 7.3c and 7.3g. Interestingly, blocking the two-photon term yields a zero conductivity for $T = 0\,\mathrm{K}$ and for $\lambda = 1$, and a nonzero conductivity for intermediate values (Fig. 7.3k). The nonzero conductivity arises due to the fact that the two-photon transition is not completely blocked at elevated temperatures. Finally, the behavior of the transverse third-harmonic conductance (Figs. 7.3d, 7.3h and 7.3l) follows very closely that of the longitudinal third-harmonic conductance.

In Fig. 7.4 we plot the third-order conductances as a function of excitation frequency for two different values of the superlattice parameter λ with linearly and circularly-polarized excitation fields. The longitudinal conductances illustrated in Figs. 7.4a and 7.4b depend on λ solely through the superlattice response function $f(\phi, \alpha, \beta, \lambda)$. This suggests that direct experimental measurement of the superlattice response function should be possible. Conversely, the strong dependence of the transverse conductances on λ through both the superlattice response function and the coefficients for each term in the conductance expressions is readily observed at both $T = 0\,\mathrm{K}$ and $300\,\mathrm{K}$. Further, at room temperature, a sharp null in the the third-harmonic conductances is observed, *e.g.* at approximately $f = \omega/2\pi = 2.4\,\mathrm{THz}$ for the longitudinal conductance and at approximately $f = \omega/2\pi = 3.1\,\mathrm{THz}$. This null is a result of the destructive interference between the different terms in the expressions

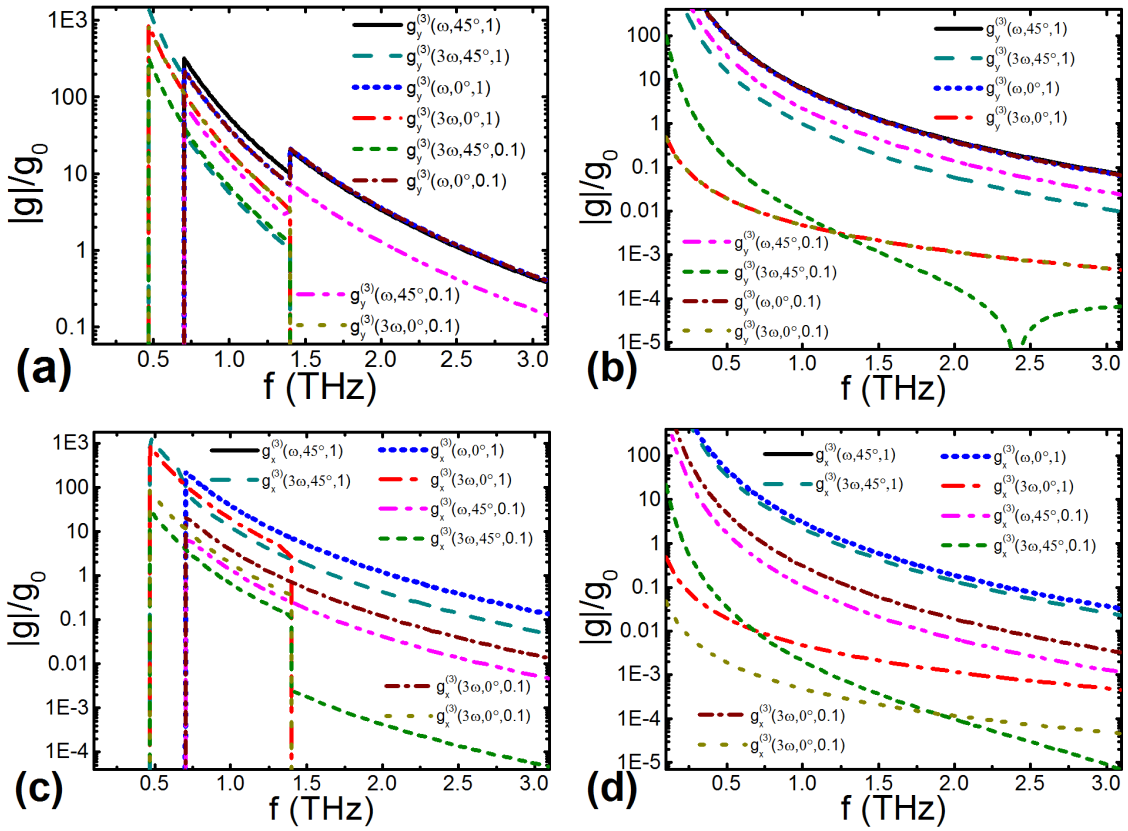

Figure 7.4: Magnitude of the third-order conductances for extrinsic mGNRsl20 ($\Omega/2\pi = 0.7\,\mathrm{THz}$) as a function of excitation frequency $f = \omega/2\pi$ for various values of polarization angle ϕ and superlattice parameter λ; a) longitudinal conductances at $T = 0\,\mathrm{K}$, b) longitudinal conductances at $T = 300\,\mathrm{K}$, c) transverse conductances at $T = 0\,\mathrm{K}$, and d) transverse conductances at $T = 300\,\mathrm{K}$. $E_0 = 10\,\mathrm{kV/m}$ for all plots.

for the conductances, Eqs. (7.5) and (7.6).

We study the temperature-dependence of this interference phenomenon in more detail in Fig. 7.5. The location of the null increases in frequency as temperature increases. This behavior results from the overall cancellation of the product of the superlattice response function and the thermal factor with increasing temperature,

and agrees with the discussion of Fig. 7.3. For excitation frequencies $\omega > 2\Omega$, there is also a second zero at low temperature due to this overall cancellation that can be seen in Fig. 7.5 as well.

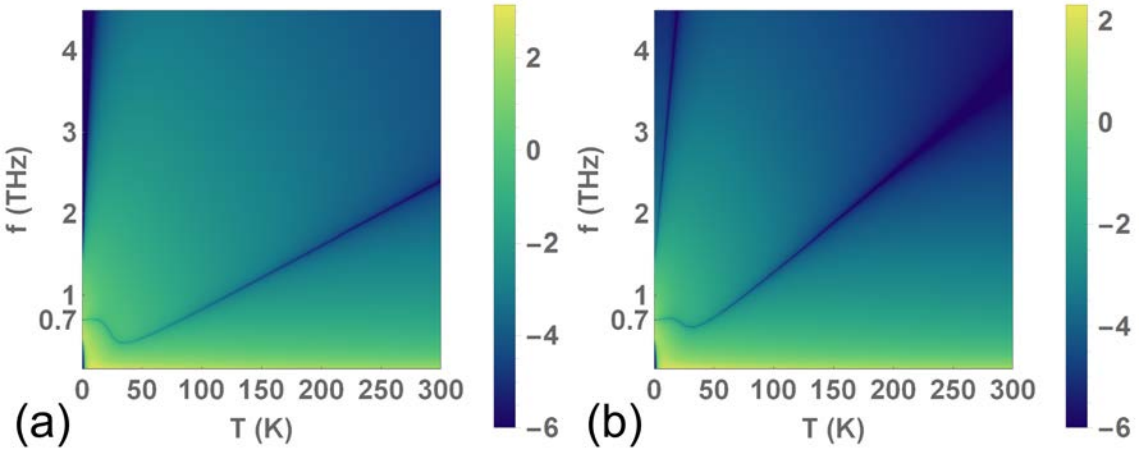

Figure 7.5: Magnitude of the third-harmonic conductances for extrinsic mGNRsl20 ($\Omega/2\pi = 0.7\,\mathrm{THz}$) as a function of temperature and the excitation frequency $f = \omega/2\pi$; a) $\log(|g_y^{(3)}(3\omega, 45°, 0.1)|/g_0)$, and b) $\log(|g_x^{(3)}(3\omega, 45°, 0.1)|/g_0)$. For all plots, $E_0 = 10\,\mathrm{kV/m}$.

7.4 Conclusions

In conclusion, we have studied the third-order nonlinear conductance in metallic armchair graphene nanoribbon superlattices using time-dependent perturbation theory and a simple $\mathbf{k}\cdot\mathbf{p}$ model for an elliptically-polarized excitation field at normal incidence. Our results predict several novel features. The most important of these is that by varying the superlattice parameter λ, it is possible to tune the sign and

magnitude of the nonlinear response. Secondly, through experimental measurement of the longitudinal third-order conductances, it should be possible to directly evaluate the superlattice response function. Finally, by varying λ through its dependence on the applied superlattice potential V_0, it is possible to switch the transverse Kerr conductance between ON and OFF states over a wide range of temperatures.

Active control of THz polarization spectroscopy is vital for optical material characterization and various applications in communication technology. Unlike conventional semiconductors, graphene nanoribbon superlattices can be easily tuned electrically in the THz range. Therefore, THz spectroscopy using graphene nanoribbons could lead to ultrathin THz polarization modulators.

CHAPTER 8
CONCLUSIONS AND OUTLOOK

8.1 Conclusions

In this thesis, we have systematically studied the terahertz nonlinear optical response of armchair graphene nanoribbons and several sister structures. These structures can generate strong nonlinear currents when optically stimulated by moderately-strong terahertz fields and exhibit nonlinearities unmatched by any other conventional semiconductor materials. Additionally, a model based on the $\mathbf{k} \cdot \mathbf{p}$ time dependent perturbation theory is developed. Unlike the tight-binding and other sophisticated methods that require much more computational effort, the $\mathbf{k} \cdot \mathbf{p}$ model is simple, effective, and requires less computation time.

In the discussion of the results in this thesis, we demonstrated there are many ways to tune the terahertz nonlinear response of metallic armchair graphene nanoribbon based structures. Such easy tunability can be achieved via the change of Fermi level, the size of the metallic graphene nanoribbon structures, the spatial profile of the applied terahertz radiation field, the polarization of the applied terahertz radiation field, engineering of the band gap, and the application of a periodic superlattice potential. These findings mean that thin metallic graphene nanoribbon based structures may enable novel nonlinear optical, electronic, and photonic devices working in the terahertz spectral range, with extremely high speed, strong response, low required external excitation field strength, and a much more compact size than conventional

semiconductor, as well as 2D single layer graphene based structures.

High quality thin armchair graphene nanoribbons were only first reported in 2015, but until now there has been no theoretical investigation into the terahertz nonlinear response of these nanoribbons. The versatility of the tunability shown in this thesis regarding the strong terahertz nonlinear optical response of metallic graphene nanoribbons, in connection with the state of art of the thin armchair graphene nanoribbon synthesis, provide new advances in fundamental understanding of these nanoribbons, and will set the stage for the development of nonlinear terahertz armchair nanoribbon opto-electronic and photonic technology. All of the work shown in this thesis fits well in the timeline for the next generation of terahertz graphene electronics (see Fig. 8.1).

8.2 Outlook

8.2.1 Luttinger Liquid

Quasi 1D structures exhibit fascinating quantum phenomena, the Luttinger Liquid state, which is a low-dimensional state characterized by strong particle-particle interactions. The behaviour of the metallic states of electrons in 2D and 3D are like weakly interacting fermions, and can be described by a Fermi liquid, in which the excitations carry a charge e, and a spin 1/2. In 1D, charge carriers no longer behave like a Fermi liquid. Instead, spin and charge excitations behave like bosonic particles and propagate at different velocities [131].

The Luttinger Liquid (LL) model is appropriate to describe transport proper-

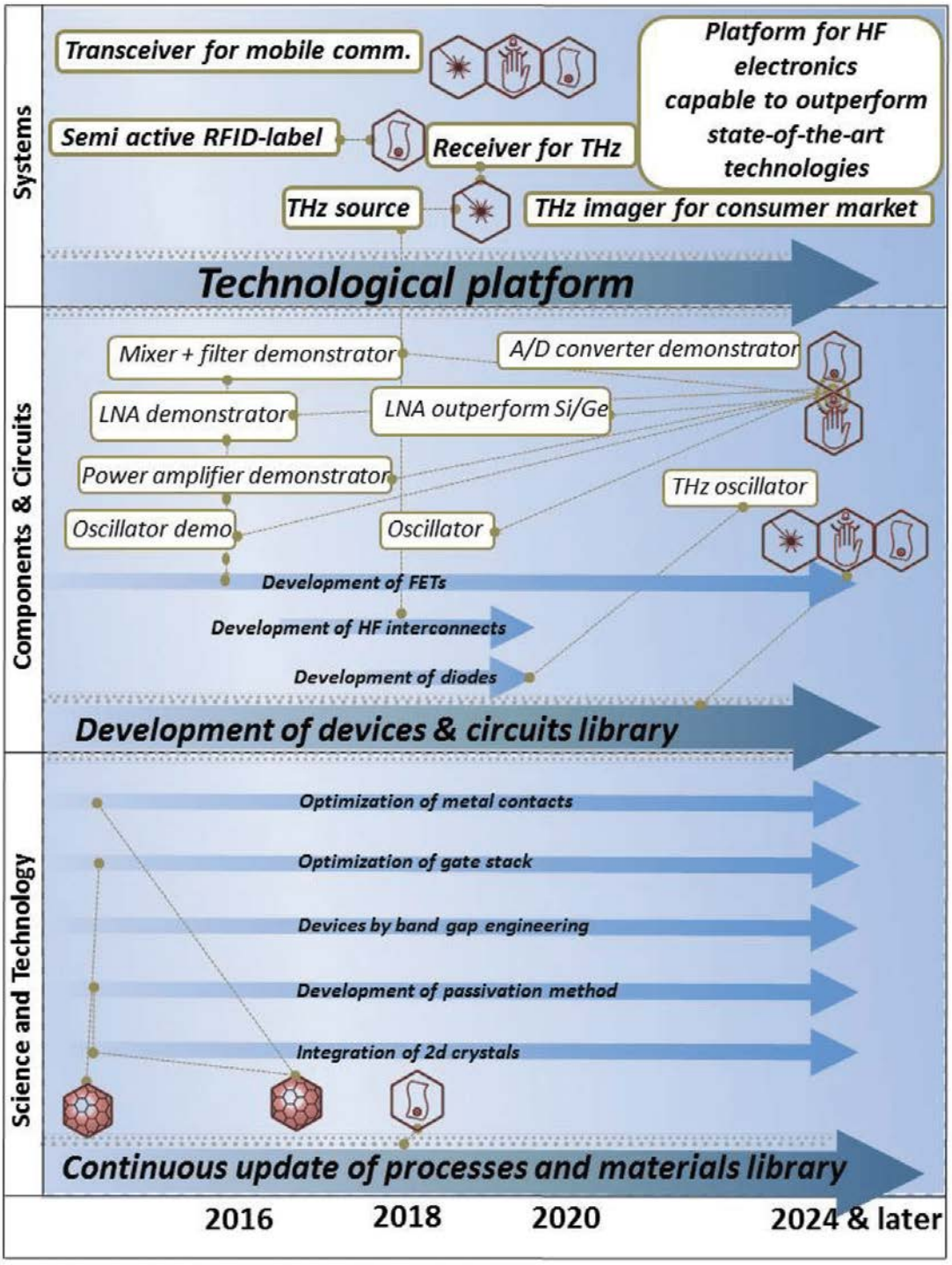

Figure 8.1: Timeline for high frequency (including THz) graphene electronics. This figure is obtained from [1].

ties of quasi 1D system with electron-electron interactions. The LL system has two types. One is the chiral LL: its right and left moving branches are spatially separated [132], such as carbon nanotubes [133]. The other LL is the non-chiral type whose right and left movers interact in the same channel [134], such as a narrow quantum wire formed in conventional semiconductor heterostructures.

Edge states in graphene nanoribbon are predicted to be a LL [6]. High quality nanoribbons should have 1D square root singularities in their density of states [6]. In the LL model, a quantum capacitance and quantum inductance can be defined for the Luttinger wire [135]. This implies that the AC transport behaviour of the Luttinger wire can be converted to a classical transmission line circuit model. Furthermore, Burke has developed a transmission line model for the 1D spinless electron system of single wall carbon nanotube (SWCNT) [136]. Naeemi and Meindl have proposed a linear circuit model for graphene nanoribbons [137]. Imambekov has developed a universal nonlinear LL theory [138] which addresses the nonlinear part of the LL model. In his theory, he shows that one needs to take the nonlinearity of the generic spectrum into consideration, and that the nonlinearity leads to a qualitative change in the spectral function.

As a result, it is essential to investigate the modified nonlinear LL model of metallic acGNR, find the nonlinear conductance correction terms (the equivalent quantum conductance and inductance), and propose an effective nonlinear transmission line model. A nonlinear circuit model is crucial to further development of graphene nanoribbon integrated circuits, as that would make it easier for engineers to

design various graphene nanoribbon based integrated circuits with standard circuit technique.

8.2.2 Effect of symmetry breaking

Bandgap opening, the presense of a magnetic field, elliptically polarized radiation, oblique incidence *et. al.* break the symmetry of the graphene, and thus lead to second harmonic generation in 2D single layer graphene [8]. It will be crucial to investigate the effect of symmetry breaking in the second order nonlinear response.

Effects, such as the presence of multiple quantum well potential, and the application of magnetic field *et. al.*, all change the properties of the spin and valley of graphene nanoribbons, and they show quantum qubits [12–15]. The interband optical response of metallic armchair graphene nanoribon structures calculated in this thesis is indistinguishable from $\mathbf{K}$ and $\mathbf{K}'$ valley. However, in the presence of a staggered magnetice field, which is positive near the center of each hexagon and negative near the edges, it introduces a complex phase shift $e^{i\phi}$ for the next nearest neighbor hopping t_1. As a result, the band gap opening will be $E_g/2 \mp 3\sqrt{3}t_1 \sin(\phi)$ for the $\mathbf{K}(\mathbf{K}')$ valley [30], thus introducing asymmetries of the valley. The chiral vector potential formed [31] via kink, twisting *et. al.* [31] can also introduce asymmetries in the band gap opening as well. It will be interesting to see if a nonlinear valley-current can be generated in these configurations.

8.2.3 Fully quantum model

The model discussed in this thesis is not a complete quantum description of the problem. The consideration of intraband transition, heavy doping, higher frequencies, various scattering mechanism, defects are crucial to a fully quantum model of the nonlinear response of armchair graphene nanoribbons. Since a complete quantum description of the nonlinear response of 2D single layer graphene has not been developed due to the complexity of the problem [68]. It may be difficult to develop a fully quantum description of the nonlinear terahertz response of armchair graphene nanoribbons as well. However, further development of the current model adopted in this thesis, based on combinations of several independent quantum models of 2D single layer graphene [34,52,68,71,73], may lead to a fully quantum description of the terahertz nonlinear response of armchair graphene nanoribbons.

8.2.4 Characterization of terahertz nonlinear response of stacked armchair graphene nanoribbons

Until now, there's no available low energy $\mathbf{k} \cdot \mathbf{p}$ models for bilayer and multilayer graphene nanoribbons. Bilayer and multilayer graphene exhibit a different nonlinear optical response than the single layer graphene [8], and as a result, it will be crucial to study terahertz nonlinearities in bilayer and multilayer graphene nanoribbons.

Similarly to bilayer graphene nanoribbons, it will be interesting to study the spatially stacked graphene nanoribbons. Due to the interplay between intralayer

and interlayer coupling of these stacked multiple graphene nanoribbons systems, prediction shows such stacking could have a major influence on both their electronic structure and magnetic states [131], and may offer vast opportunities for device applications of structures formed by stacked nanoribbons [1].

Calculations of the linear plasmon dispersion in single as well as spatially stacked double metallic graphene nanoribbon were performed [39, 40, 139, 140]. Recently, studies show that nonlinear surface plasmon polaritons in the graphene layer exhibit optical bistability [141]. Furthermore, coherent nonlinear Rabi oscillations and Rashba spin-orbit interactions may be useful barometers for studying the low-energy electronic structure of bilayer and multi-layer graphene systems [142, 143]. It would be useful to characterize the terahertz nonlinear response of stacked graphene nanoribbons.

8.2.5 Energy conversion and storage applications of stacked armchair graphene nanoribbons

Chemically functionalized stacked armchair graphene nanoribbons can improve storage and diffusion of ionic species and electric charge in batteries and supercapacitors, thus enabling the realization of ultrathin-film photovoltaic devices or systems for reliable and environmentally friendly production of energy-storage systems [1, 144].

APPENDIX A
VECTOR POTENTIAL DERIVATION

[1] In the Coulomb gauge, for a constant scalar potential ($\nabla\varphi = 0$), the relationship between the vector potential and the electric field is $E(t) = -\partial A(t)/\partial t$. Thus, for an electric field $E(t) = E_0 e^{-i\omega t}$ that is turned on at time t_0, the vector potential is written:

$$A(t) = -\int_{t_0}^{t} E(t_1)\, dt_1 = -E_0 \int_{t_0}^{t} e^{-i\omega t_1}\, dt_1 \tag{A.1}$$

Considering a time-harmonic field turned on at $t_0 \to -\infty$, we write the integral in Eq. (A.1):

$$\begin{aligned} I =& \int_{-\infty}^{t} e^{-i\omega t_1}\, dt_1 \\ =& \int_{-\infty}^{0} e^{-i\omega t_1}\, dt_1 + \int_{0}^{t} e^{-i\omega t_1}\, dt_1 \\ =& I_1 + I_2 \end{aligned} \tag{A.2}$$

In order to evaluate the integral I_1, we introduce an infinitesimally small positive parameter τ, which corresponds to the field turning on at $t_0 \to -\infty$ adiabatically [53, 54]. With $t' = -t_1$:

$$\begin{aligned} I_1 &= \lim_{\tau\to 0} \int_{-\infty}^{0} e^{(\tau - i\omega)t_1}\, dt_1 \\ &= \lim_{\tau\to 0} \int_{0}^{\infty} e^{-(\tau - i\omega)t'}\, dt' \end{aligned} \tag{A.3}$$

We have the following formula [145]. For $\mathrm{Re}[p] > 0$,

$$\int_{0}^{\infty} e^{-px}\, dx = \frac{1}{p} \tag{A.4}$$

[1] This Appendix A is based on the Appendix A of *Phy. Rev. B.* **93**, 235430 (2016) [10]

With $p = \tau - i\omega$, the condition $\mathrm{Re}\,[\tau - i\omega] = \tau > 0$ is satisfied. So Eq. (A.4) is:

$$\begin{aligned} I_1 &= \lim_{\tau\to 0} \int_0^\infty e^{-(\tau - i\omega)t'}\, dt' \\ &= \lim_{\tau\to 0} \int_0^\infty e^{-px}\, dx \\ &= \lim_{\tau\to 0} \frac{1}{p} = \lim_{\tau\to 0} \frac{1}{\tau - i\omega} \\ &= \frac{1}{-i\omega} \end{aligned} \tag{A.5}$$

Evaluating the integral I_2, we obtain:

$$\begin{aligned} I_2 &= \int_0^t e^{-i\omega t}\, dt_1 \\ &= \frac{e^{-i\omega t} - 1}{-i\omega} \end{aligned} \tag{A.6}$$

The total integral I is obtained by summing I_1 and I_2:

$$I = I_1 + I_2 = \frac{1}{-i\omega} + \frac{e^{-i\omega t} - 1}{-i\omega} = \frac{e^{-i\omega t}}{-i\omega} \tag{A.7}$$

and the vector potential in the Coulomb gauge for a time-harmonic electric field that turns on adiabatically at $t_0 \to -\infty$ becomes:

$$A(t) = -E_0 I = \frac{-E_0 e^{-i\omega t}}{-i\omega} = \frac{E(t)}{i\omega} \tag{A.8}$$

Similarly, for the electric field of the form $E_1(t) = E_1 e^{i\omega t}$ turned on adiabatically at $t_0 \to -\infty$ under the Coulomb gauge, the magnetic vector potential is

$$A_1(t) = -\int_{t_0}^t E_1(t_1)\, dt_1 = -E_1 \int_{t_0}^t e^{i\omega t_1}\, dt_1 = -E_1 \frac{e^{i\omega t}}{i\omega} = -\frac{E_1(t)}{i\omega} \tag{A.9}$$

And we recover the magnetic vector potential used in Ref. [32, 51, 52, 55, 57].

APPENDIX B
DERIVATION OF THE THIRD ORDER CONDUCTANCE IN 2D SINGLE LAYER GRAPHENE

[1] A.R. Wright *et.al.* [52], proposed a model to analyze the nonlinear response of two-dimensional single-layer graphene (2D SLG) in the THz regime. Similar results were also reviewed by Ang *et.al* [146] where a correction was made to the expression for the third-order third-harmonic nonlinear conductance (see Ref. [52, eq. 9] and Ref. [55, eq. 71]). We have used this model as a starting point in our study of the THz nonlinearity in metallic graphene nanoribbons. One of our goals was to follow the model proposed in that paper and verify the 2D SLG result so that we could compare it with our nanoribbon results.

In the following, we outline our independent replication of the calculation as it appeared in Ref. [52]. We find errors in Ref. [52,55] in the expressions for third-order Kerr conductance.

We begin with the model of Ref. [52] for intrinsic 2D SLG that includes an applied linearly-polarized electric field in the x direction, $\mathbf{E}(t) = \hat{x}E_x e^{i\omega t}$. The interaction Hamiltonian for such a system is $H = v_F \boldsymbol{\sigma} \cdot (\mathbf{p} + q\mathbf{A})$. From the equation $\mathbf{E} = -\frac{\partial \mathbf{A}}{\partial t} = -i\omega\mathbf{A} = \hat{x}E_x e^{i\omega t}$, and $q = -e$, we get $q\mathbf{A} = \hat{x}\frac{eE_x}{i\omega}e^{i\omega t}$. So the interaction Hamiltonian can be written as:

$$H = v_F \begin{pmatrix} 0 & p_x - ip_y + \frac{eE_x}{i\omega}e^{i\omega t} \\ p_x + ip_y + \frac{eE_x}{i\omega}e^{i\omega t} & 0 \end{pmatrix} \tag{B.1}$$

[1]This Appendix B is based on the Appendix B of *Phy. Rev. B.* **93**, 235430 (2016) [10]

The wavefunction $\psi(\mathbf{r},t)$ solution to Eq. 1 can be expressed in a Fourier series form:

$$\psi(\mathbf{r},t)=\sum_{n=0}^{\infty}\phi_n(\mathbf{p})e^{i(k_xx+k_yy)}e^{in\omega t}e^{-i\epsilon t/\hbar} \tag{B.2}$$

where $\epsilon = sv_Fp$, $p_x = p\cos(\theta)$, $p_y = p\sin(\theta)$ and $\tan(\theta) = p_y/p_x$, with $s = \pm 1$ the band index. The total energy $\epsilon - n\hbar\omega$ with applied field $\hat{x}E_xe^{i\omega t}$ implies that the carriers lose energy $n\hbar\omega$. This describes the process where an electron in the conduction band loses energy $n\hbar\omega$ and makes an interband transition to the valence band. So we choose $s = 1$ for this case. As a result, the spinor $\phi_n(\mathbf{p})$ can be expressed as $\phi_n(\mathbf{p}) = [a_n(p,\theta), b_n(p,\theta)]^T$, and we rewrite the wavefunction in the following form:

$$\psi(\mathbf{r},t)=\sum_{n=0}^{\infty}\begin{bmatrix}a_n(p,\theta)\\ b_n(p,\theta)\end{bmatrix}e^{ip[\cos(\theta)x+\sin(\theta)y]/\hbar}e^{in\omega t}e^{-iv_Fpt/\hbar} \tag{B.3}$$

The wavefunction $\psi(\mathbf{r},t)$ satisfies the Schrödinger equation $H\psi(\mathbf{r},t) = i\hbar\frac{\partial\psi(\mathbf{r},t)}{\partial t}$. After some algebra and using the orthogonal properties of the basis sets $\{e^{i\omega t}\}$, we arrive at a set of recursion relations, which give the coupling between the $n-1$ and n state:

$$\begin{aligned}(v_Fp-n\hbar\omega)\,a_n &= v_Fp\,[\cos(\theta)-i\sin(\theta)]\,b_n+\frac{eE_xv_F}{i\omega}b_{n-1}\\ (v_Fp-n\hbar\omega)\,b_n &= v_Fp\,[\cos(\theta)+i\sin(\theta)]\,a_n+\frac{eE_xv_F}{i\omega}a_{n-1}\end{aligned} \tag{B.4}$$

The intial condition $\begin{pmatrix}a_0\\ b_0\end{pmatrix}$ is the initial state of the electron in the conduction band without the applied electric field, or $n = 0$:

$$\begin{pmatrix}\phi_0(\mathbf{p})=a_0\\ b_0\end{pmatrix}=\frac{1}{\sqrt{2}}\begin{pmatrix}1\\ e^{i\theta}\end{pmatrix} \tag{B.5}$$

and the first four spinors obtained from the recursion relations are the following:

$$a_0(p,\theta) = \frac{1}{\sqrt{2}} \tag{B.6}$$

$$b_0(p,\theta) = \frac{e^{i\theta}}{\sqrt{2}} \tag{B.7}$$

$$a_1(p,\theta) = \frac{ieE_x v_F \left[(2pv_F - \hbar\omega)\cos(\theta) - i\hbar\omega\sin(\theta)\right]}{\sqrt{2}\hbar\omega^2(2pv_F - \hbar\omega)} \tag{B.8}$$

$$b_1(p,\theta) = \frac{ieE_x v_F \left[(1+e^{2i\theta})pv_F - \hbar\omega\right]}{\sqrt{2}\hbar\omega^2(2pv_F - \hbar\omega)} \tag{B.9}$$

$$a_2(p,\theta) = \frac{e^2E_x^2v_F^2\left[-(pv_F - \hbar\omega)(pv_F - \hbar\omega + pv_F\cos(2\theta)) + ipv_F\hbar\omega\sin(2\theta)\right]}{2\sqrt{2}\hbar^2\omega^4(2pv_F - \hbar\omega)(pv_F - \hbar\omega)} \tag{B.10}$$

$$b_2(p,\theta) = \frac{e^2E_x^2v_F^2e^{-i\theta}\left[-e^{4i\theta}p^2v_F^2 - 2e^{2i\theta}(pv_F - \hbar\omega)^2 - pv_F(pv_F - 2\hbar\omega)\right]}{4\sqrt{2}\hbar^2\omega^4(2pv_F - \hbar\omega)(pv_F - \hbar\omega)} \tag{B.11}$$

$$\begin{aligned} a_3(p,\theta) = &- \frac{ie^3E_x^3v_F^3e^{-3i\theta}[(1+e^{2i\theta})^3p^3v_F^3 - 3e^{2i\theta}(3+4e^{2i\theta}+e^{4i\theta})p^2v_F^2\hbar\omega]}{12\sqrt{2}\hbar^3\omega^6(2pv_F - \hbar\omega)(pv_F - \hbar\omega)(2pv_F - 3\hbar\omega)} \\ &- \frac{ie^3E_x^3v_F^3e^{-3i\theta}[2e^{2i\theta}(4+7e^{2i\theta})pv_F\hbar^2\omega^2 - 6e^{4i\theta}\hbar^3\omega^3]}{12\sqrt{2}\hbar^3\omega^6(2pv_F - \hbar\omega)(pv_F - \hbar\omega)(2pv_F - 3\hbar\omega)} \end{aligned} \tag{B.12}$$

$$\begin{aligned} b_3(p,\theta) = &- \frac{ie^3E_x^3v_F^3e^{-2i\theta}[(1+e^{2i\theta})^3p^3v_F^3 - 3(1+4e^{2i\theta}+3e^{4i\theta})p^2v_F^2\hbar\omega]}{12\sqrt{2}\hbar^3\omega^6(2pv_F - \hbar\omega)(pv_F - \hbar\omega)(2pv_F - 3\hbar\omega)} \\ &- \frac{ie^3E_x^3v_F^3e^{-2i\theta}[2e^{2i\theta}(7+4e^{2i\theta})pv_F\hbar^2\omega^2 - 6e^{2i\theta}\hbar^3\omega^3]}{12\sqrt{2}\hbar^3\omega^6(2pv_F - \hbar\omega)(pv_F - \hbar\omega)(2pv_F - 3\hbar\omega)} \end{aligned} \tag{B.13}$$

By introducing $\omega = \omega + i\Gamma$, where $\Gamma \to 0$ in the first order poles of the denominator in the spinor, we arrive at:

$$a_0(p,\theta,\Gamma) = \frac{1}{\sqrt{2}} \tag{B.14}$$

$$b_0(p,\theta,\Gamma) = \frac{e^{i\theta}}{\sqrt{2}} \tag{B.15}$$

$$a_1(p,\theta,\Gamma) = \frac{ieE_x v_F \left[(2pv_F - \hbar\omega)\cos(\theta) - i\hbar\omega\sin(\theta)\right]}{\sqrt{2}\hbar\omega^2(2pv_F - \hbar(\omega+i\Gamma))} \tag{B.16}$$

$$b_1(p,\theta,\Gamma) = \frac{ieE_x v_F \left[(1+e^{2i\theta})pv_F - \hbar\omega\right]}{\sqrt{2}\hbar\omega^2(2pv_F - \hbar(\omega+i\Gamma))} \tag{B.17}$$

$$a_2(p,\theta,\Gamma) = \frac{e^2E_x^2v_F^2\left[-(pv_F - \hbar\omega)(pv_F - \hbar\omega + pv_F\cos(2\theta)) + ipv_F\hbar\omega\sin(2\theta)\right]}{2\sqrt{2}\hbar^2\omega^4(2pv_F - \hbar(\omega+i\Gamma))(pv_F - \hbar(\omega+i\Gamma))} \tag{B.18}$$

$$b_2(p,\theta,\Gamma) = \frac{e^2E_x^2v_F^2e^{-i\theta}\left[-e^{4i\theta}p^2v_F^2 - 2e^{2i\theta}(pv_F-\hbar\omega)^2 - pv_F(pv_F-2\hbar\omega)\right]}{4\sqrt{2}\hbar^2\omega^4(2pv_F-\hbar(\omega+i\Gamma))(pv_F-\hbar(\omega+i\Gamma))} \tag{B.19}$$

$$\begin{aligned} a_3(p,\theta,\Gamma) = &- \frac{ie^3E_x^3v_F^3e^{-3i\theta}[(1+e^{2i\theta})^3p^3v_F^3 - 3e^{2i\theta}(3+4e^{2i\theta}+e^{4i\theta})p^2v_F^2\hbar\omega]}{12\sqrt{2}\hbar^3\omega^6(2pv_F-\hbar(\omega+i\Gamma))(pv_F-\hbar(\omega+i\Gamma))(2pv_F-3\hbar(\omega+i\Gamma))} \\ &- \frac{ie^3E_x^3v_F^3e^{-3i\theta}[2e^{2i\theta}(4+7e^{2i\theta})pv_F\hbar^2\omega^2 - 6e^{4i\theta}\hbar^3\omega^3]}{12\sqrt{2}\hbar^3\omega^6(2pv_F-\hbar(\omega+i\Gamma))(pv_F-\hbar(\omega+i\Gamma))(2pv_F-3\hbar(\omega+i\Gamma))} \end{aligned} \tag{B.20}$$

$$\begin{aligned} b_3(p,\theta,\Gamma) = &- \frac{ie^3E_x^3v_F^3e^{-2i\theta}[(1+e^{2i\theta})^3p^3v_F^3 - 3(1+4e^{2i\theta}+3e^{4i\theta})p^2v_F^2\hbar\omega]}{12\sqrt{2}\hbar^3\omega^6(2pv_F-\hbar(\omega+i\Gamma))(pv_F-\hbar(\omega+i\Gamma))(2pv_F-3\hbar(\omega+i\Gamma))} \\ &- \frac{ie^3E_x^3v_F^3e^{-2i\theta}[2e^{2i\theta}(7+4e^{2i\theta})pv_F\hbar^2\omega^2 - 6e^{2i\theta}\hbar^3\omega^3]}{12\sqrt{2}\hbar^3\omega^6(2pv_F-\hbar(\omega+i\Gamma))(pv_F-\hbar(\omega+i\Gamma))(2pv_F-3\hbar(\omega+i\Gamma))} \end{aligned} \tag{B.21}$$

The current operator for the x component of the $(n+m)$th order current is

$$j_x^{n+m}((n-m)\omega) = -ev_F\phi_m^\dagger(p,\theta)\sigma_x\phi_n(p,\theta) = -ev_F\left[a_nb_m^* + a_m^*b_n\right] \tag{B.22}$$

The spinor is a function of p, θ and Γ. Thus the total current density is written:

$$J_x^{n-m} = \lim_{\Gamma\to 0}\frac{-g_sg_vev_F}{(2\pi\hbar)^2}\int_0^{2\pi}d\theta\int_0^\infty \Re\left\{\left[a_nb_m^* + a_m^*b_n\right]N(p)p\right\}dp \tag{B.23}$$

Since $\int_0^{2\pi}\cos(2\theta)d\theta = \int_0^{2\pi}\sin(2\theta)d\theta = \int_0^{2\pi}\cos(4\theta)d\theta = \int_0^{2\pi}\sin(4\theta)d\theta = 0$,

$$\begin{aligned} J_3^x(\omega) = &\lim_{\Gamma\to 0}\frac{g_sg_v}{(2\pi\hbar)^2}g_0\eta\int_0^{2\pi}d\theta\int_0^\infty dp \\ &\times\Re\left\{i\frac{-v_F^2(3p^3v_F^3 - 8\hbar p^2v_F^2\hbar\omega + 6pv_F\hbar^2\omega^2 - 2\hbar^3\omega^3)N(p)p}{\omega^2[2pv_F-\hbar(\omega+i\Gamma)][2pv_F-\hbar(\omega-i\Gamma)][pv_F-\hbar(\omega+i\Gamma)]}\right\} \end{aligned} \tag{B.24a}$$

$$\begin{aligned} J_3^x(3\omega) = &\lim_{\Gamma\to 0}\frac{g_sg_v}{(2\pi\hbar)^2}g_0\eta\int_0^{2\pi}d\theta\int_0^\infty dp \\ &\times\Re\left\{i\frac{v_F^2(3p^3v_F^3 - 12\hbar p^2v_F^2\hbar\omega + 14pv_F\hbar^2\omega^2 - 6\hbar^3\omega^3)N(p)p}{3\omega^2[2pv_F-\hbar(\omega+i\Gamma)][pv_F-\hbar(\omega+i\Gamma)][2pv_F-3\hbar(\omega+i\Gamma)]}\right\} \end{aligned} \tag{B.24b}$$

with g_s, $g_v = 2$, $g_0 = \frac{e^2}{4\hbar}$, $\eta = \frac{e^2E_x^2v_F^2}{\hbar^2\omega^4}$, and $N(p) = \tanh(\frac{pv_F}{2k_BT})$. In these expressions, the integrands are of the form:

$$i_1(x) = f_1(x)\Re\left[i\frac{1}{(2x - x_0 - i\Gamma)(2x - x_0 + i\Gamma)(x - x_0 - i\Gamma)}\right] \tag{B.25}$$

$$i_3(x) = f_3(x)\Re\left[i\frac{1}{(2x - x_0 - i\Gamma)(x - x_0 - i\Gamma)(2x - 3x_0 - i3\Gamma)}\right] \tag{B.26}$$

for the Kerr and third-order currents respectively, with $f_1(x)$, $f_3(x)$, x_0, Γ real. the integrands for the third order conductances become:

$$i_1(x) = f_1(x)\frac{\pi}{x\,(3x - 2x_0)}\left[\frac{1}{\pi}\frac{\Gamma}{(2x - x_0)^2 + \Gamma^2} - \frac{1}{\pi}\frac{\Gamma}{(x - x_0)^2 + \Gamma^2}\right] \tag{B.27a}$$

$$i_3(x) = f_3(x)\frac{\pi}{x^2}\left[-\frac{1}{4}\frac{1}{\pi}\frac{\Gamma}{(2x - x_0)^2 + \Gamma^2} + \frac{1}{\pi}\frac{\Gamma}{(x - x_0)^2 + \Gamma^2} - \frac{9}{4}\frac{1}{\pi}\frac{3\Gamma}{(2x - 3x_0)^2 + 9\Gamma^2}\right] \tag{B.27b}$$

As a result, the expressions for the current density in Eq. (B.24) above may be expanded as a set of integrals of the form:

$$Z_1 = \lim_{\Gamma\to 0}\int_a^b \Re\left[\frac{iz(x)}{x - x_0 \mp i\Gamma}\right]dx = \lim_{\Gamma\to 0}\int_a^b \Re\left[z_1(x, x_0, \Gamma)\right]dx \tag{B.28}$$

with $z(x)$, x, x_0, $\Gamma > 0$ real. Using the property:

$$\lim_{\Gamma\to 0}\frac{1}{\pi}\frac{\Gamma}{(x - x_0)^2 + \Gamma^2} = \delta(x - x_0) \tag{B.29}$$

we arrive at $Z_1 = \pi f(x_0)$. Several example problems involving this type of kernel may be found in Refs. [147–150]. So the problem reduces to the evaluations of the following:

$$\begin{aligned}\lim_{\Gamma\to 0}\frac{\hbar\Gamma}{4p^2v_F^2 - 4pv_F\hbar\omega + \hbar^2\omega^2 + \hbar^2\Gamma^2} &= \lim_{\hbar\Gamma\to 0}\frac{\hbar\Gamma}{(2pv_F - \hbar\omega)^2 + (\hbar\Gamma)^2}\\ &= \pi\delta(2pv_F - \hbar\omega)\\ &= \frac{\pi}{2v_F}\delta(p - \frac{\hbar\omega}{2v_F})\end{aligned}$$

$$\lim_{\Gamma\to 0}\frac{\hbar\Gamma}{p^2v_F^2-2pv_F\hbar\omega+\hbar^2\omega^2+\hbar^2\Gamma^2}=\lim_{\hbar\Gamma\to 0}\frac{\hbar\Gamma}{(pv_F-\hbar\omega)^2+(\hbar\Gamma)^2}$$
$$=\pi\delta(pv_F-\hbar\omega)$$
$$=\frac{\pi}{v_F}\delta(p-\frac{\hbar\omega}{v_F})$$
$$\lim_{\Gamma\to 0}\frac{\hbar\Gamma}{4p^2v_F^2-12pv_F\hbar\omega+9\hbar^2\omega^2+9\hbar^2\Gamma^2}=\lim_{\hbar\Gamma\to 0}\frac{1}{3}\frac{3\hbar\Gamma}{(2pv_F-3\hbar\omega)^2+(3\hbar\Gamma)^2}$$
$$=\frac{\pi}{3}\delta(2pv_F-3\hbar\omega)$$
$$=\frac{\pi}{6v_F}\delta(p-\frac{3\hbar\omega}{2v_F})$$

Alternatively, we may use the Cauchy Principal Value theorem to solve this problem. Separating the real and imaginary parts of the integrand $z_1(x,x_0,\Gamma)$, we obtain:

$$\Re\left[z_1(x,x_0,\Gamma)\right]=\mp\pi\frac{1}{\pi}\frac{\Gamma}{(x-x_0)^2+\Gamma^2}z(x) \tag{B.30}$$

$$\Im\left[z_1(x,x_0,\Gamma)\right]=\frac{1}{(x-x_0)+\Gamma^2/(x-x_0)}z(x) \tag{B.31}$$

The Sokhotsky-Plemelj theorem on the real interval $[a,b]$ states [151]:

$$\lim_{\Gamma\to 0}\int_a^b\frac{g(x)}{x-x_0\mp i\Gamma}dx=\mathbb{P}\int_a^b\frac{g(x)}{x-x_0}dx\pm i\pi g(x_0) \tag{B.32}$$

where $\mathbb{P}\int_a^b g(x)dx$ denotes the Cauchy principal integral of $g(x)$. For $g(x)=iz(x)$ with $z(x)$ real, the real and imaginary parts become:

$$\Re\left[\lim_{\Gamma\to 0}\int_a^b\frac{iz(x)}{x-x_0\mp i\Gamma}\,dx\right]=\mp\pi z(x_0) \tag{B.33}$$

$$\Im\left[\lim_{\Gamma\to 0}\int_a^b\frac{iz(x)}{x-x_0\mp i\Gamma}\,dx\right]=\mathbb{P}\int_a^b\frac{z(x)}{x-x_0}dx \tag{B.34}$$

which is the same result as in Eq. (B.29).

An analysis of the interband transition using the Kubo formula has appeared in Ref. [77]. Eq. (A1) of that reference further confirms our result for 2D SLG. Based

on the above analysis, in the limit as $\Gamma \to 0$, the integrands in Eq. (B.27) reduce to:

$$\lim_{\Gamma\to 0} i_1(x) = \frac{\pi f_1(x)}{x(3x-2x_0)}\left[\frac{\delta(x-\frac{x_0}{2})}{2} - \delta(x-x_0)\right]$$
$$= -\frac{\pi f_1(x)}{x_0^2}\left[2\delta(x-\frac{x_0}{2}) + \delta(x-x_0)\right] \tag{B.35}$$

$$\lim_{\Gamma\to 0} i_3(x) = \frac{\pi f_3(x)}{x^2}\left[-\frac{1}{4}\frac{\delta(x-\frac{x_0}{2})}{2} + \delta(x-x_0) - \frac{9}{4}\frac{\delta(x-\frac{3x_0}{2})}{2}\right] \tag{B.36}$$

and the integrals reduce to:

$$I_1 = -\frac{\pi}{x_0^2}[2f_1(\frac{x_0}{2}) + f_1(x_0)] \tag{B.37}$$

$$I_3 = -\frac{\pi}{2x_0^2}\left[f_3(\frac{x_0}{2}) - 2f_3(x_0) + f_3(\frac{3x_0}{2})\right] \tag{B.38}$$

The total third-order nonlinear current densities are:

$$J_x^3(\omega) = -g_0\eta\left[\frac{5}{4}N(\frac{\omega}{2}) + 2N(\omega)\right] \tag{B.39}$$

$$J_x^3(3\omega) = g_0\eta\left[\frac{13}{48}N(\frac{\omega}{2}) - \frac{2}{3}N(\omega) + \frac{45}{48}N(\frac{3\omega}{2})\right] \tag{B.40}$$

resulting in the Kerr conductance:

$$g_{xx}^{(3)}(\omega)_{2D} = -g_0\frac{e^2E_0^2v_F^2}{\hbar^2\omega^4}\left[\frac{5}{4}\tanh(\frac{\hbar\omega}{4k_BT}) + 2\tanh(\frac{\hbar\omega}{2k_BT})\right] \tag{B.41}$$

and the third-harmonic conductance:

$$g_{xx}^{(3)}(3\omega)_{2D} = g_0\frac{e^2E_0^2v_F^2}{\hbar^2\omega^4}\left[\frac{13}{48}\tanh(\frac{\hbar\omega}{4k_BT}) - \frac{2}{3}\tanh(\frac{\hbar\omega}{2k_BT}) + \frac{45}{48}\tanh(\frac{3\hbar\omega}{4k_BT})\right] \tag{B.42}$$

Similarly, for a $\hat{y}$-polarized electric field of the form $\hat{y}E_0e^{i\omega t}$, we arrive at an identical result for the third-order Kerr current in the $\hat{y}$ direction, or equivalently $g_{xx}^{(3)}(\omega) = g_{yy}^{(3)}(\omega)$ and $g_{xx}^{(3)}(3\omega) = g_{yy}^{(3)}(3\omega)$ for 2D SLG.

From Eq. (B.41), we see that $J_x^3(\omega)$ is a superposition of 2 processes:

1. for electrons with initial energy $\epsilon = -\hbar\omega/2$, the absorption-emission-absorption of a photon with energy $\hbar\omega$
2. for electrons with initial energy $\epsilon = -\hbar\omega$, the absorption-absorption-emission of a photon with energy $\hbar\omega$.

The results from Eqs. 70, 71 of Ref. [55] are:

$$g_x^3(\omega) = -g_0 \frac{e^2 E_x^2 v_F^2}{\hbar^2\omega^4} \left[2\tanh(\frac{\hbar\omega}{2k_B T}) \right] \tag{B.43}$$

$$g_x^3(3\omega) = g_0 \frac{e^2 E_x^2 v_F^2}{\hbar^2\omega^4} \left[\frac{13}{48}\tanh(\frac{\hbar\omega}{4k_B T}) - \frac{2}{3}\tanh(\frac{\hbar\omega}{2k_B T}) + \frac{45}{48}\tanh(\frac{3\hbar\omega}{4k_B T}) \right] \tag{B.44}$$

The difference between Eq. (B.41) and Eq. (B.43) is due to the presence of the $\frac{5}{8}\tanh(\frac{\hbar\omega}{4k_B T})$ term in Eq. B.41.

From our derivation, it is clear that there should be an $\epsilon = \hbar\omega/2$ term in the $J_x^3(\omega)$ nonlinear process. Our disagreement with Refs. [52,55] may stem from the fact that they did not correctly calculate the integrand in Eq. (B.24a). They may have assumed that:

$$\begin{aligned} i_1(x) =& -f_1(x) \frac{\Gamma}{[(2x - x_0)^2 + \Gamma^2]\,[(x - x_0)^2 + \Gamma^2]} \\ =& -f_1(x) \left[\frac{1}{(2x - x_0)^2 + \Gamma^2} \right] \cdot \left[\frac{\Gamma}{(x - x_0)^2 + \Gamma^2} \right] \end{aligned}$$

and in the limit as $\Gamma \to 0$ (with a possible erroneously assumption $\Gamma^2 = 0$ in the denominator of the first factor):

$$\lim_{\Gamma\to 0} i_1(x) = -\pi f_1(x) \frac{1}{(2x - x_0)^2} \delta(x - x_0)$$

If this was their approach, they have ignored the contribution to the integral from the 2nd order pole at $x = x_0/2$. That this approach is problematic can be seen by

considering the following limit:

$$\begin{aligned} i_1(x) &= -\, f_1(x) \frac{\Gamma}{[(x-x_0)^2+\Gamma^2]\,[(2x-x_0)^2+\Gamma^2]} \\ &= -\, f_1(x) \left[\frac{\Gamma}{(2x-x_0)^2+\Gamma^2}\right] \cdot \left[\frac{1}{(x-x_0)^2+\Gamma^2}\right] \end{aligned}$$

and in the limit as $\Gamma \to 0$ (with a possible erroneously assumption $\Gamma^2 = 0$ in the denominator of the second factor):

$$\begin{aligned} \lim_{\Gamma\to 0} i_1(x) &= -\,\pi f_1(x) \frac{1}{(x-x_0)^2} \delta(2x-x_0) \\ &= -\,\frac{\pi f_1(x)}{2} \frac{1}{(x-x_0)^2} \delta(x-\frac{x_0}{2}) \end{aligned}$$

Although the starting point is the same, in this case a completely different result is obtained. So we argue that both $\delta(x-x_0/2)$ and $\delta(x-x_0)$ terms should appear in the $\lim_{\Gamma\to 0} i_1(x)$ expression, as we have established with our calculation.

To further amplify our point that there are two terms in the expression for the third-order Kerr nonlinear conductance, we note that Eq. 33 may also be written as:

$$\begin{aligned} i_1(x) &= f_1(x) \Re \left[i \frac{1}{(2x-x_0-i\Gamma)(2x-x_0+i\Gamma)(x-x_0-i\Gamma)} \right] \\ &= -f_1(x) \left[\frac{1}{(2x-x_0)^2+\Gamma^2}\right] \left[\frac{\Gamma}{(x-x_0)^2+\Gamma^2}\right] \\ &= -\frac{f_1(x)\Gamma}{4} \left[\frac{1}{(x-a_1x_0)^2+(a_1\Gamma)^2}\right] \left[\frac{1}{(x-a_2x_0)^2+(a_2\Gamma)^2}\right] \end{aligned} \tag{B.45}$$

with $a_1 = 1/2, a_2 = 1$. Eq. (B.45) is symmetric in (a_1, a_2), and therefore the integral I_1 must also be symmetric in (a_1, a_2). Thus, both $\omega/2$ and ω terms must appear in the expression for the Kerr conductance, Eq. (B.41).

A comparison of Eqs. (B.41) and (B.43) for intrinsic 2D SLG with $E_0 = 10\,\mathrm{kV/m}$ at $T = 0\,\mathrm{K}$ and $300\,\mathrm{K}$ is plotted in Fig. B.1. This shows that while small, the correction due to the $\omega/2$ resonant term is certainly not negligible.

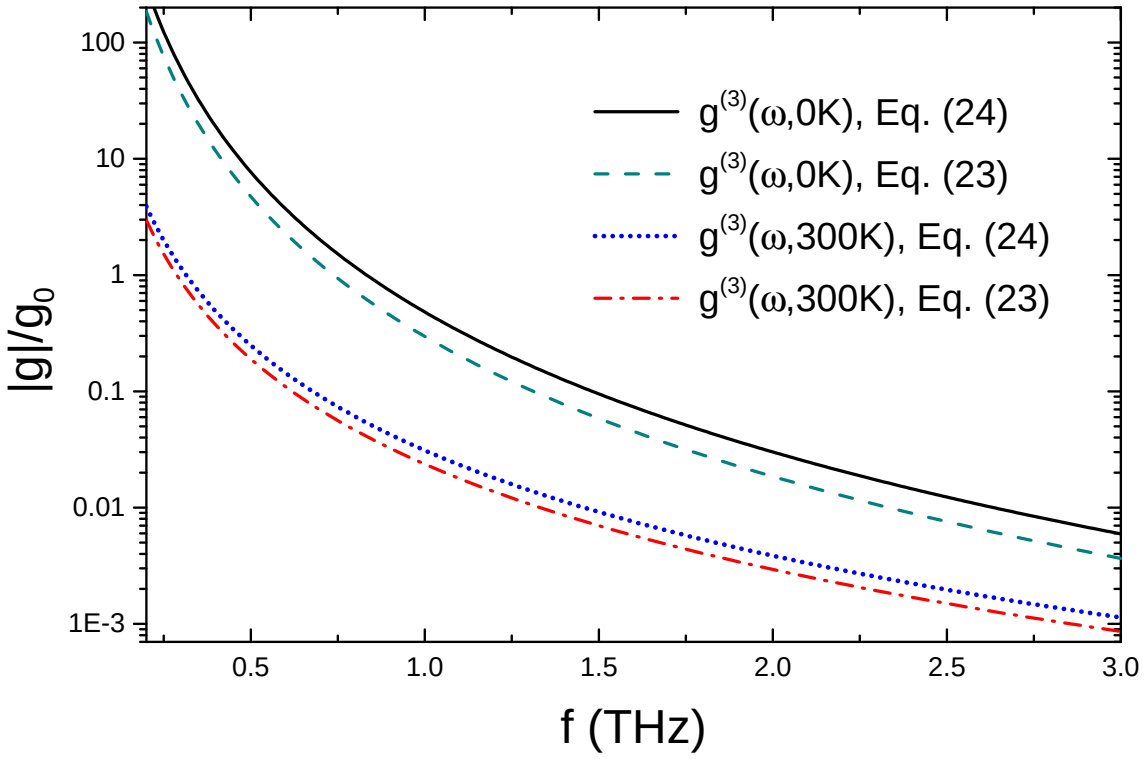

Figure B.1: Comparison of the third-order nonlinear conductance of for intrinsic 2D SLG from Ref. [10, eq. (23-24)] (Eqs. (B.41) and (B.43) in this thesis) at $T = 0\,\mathrm{K}$ and $300\,\mathrm{K}$. The field strength used in all calculations is $E_0 = 10\,\mathrm{kV/m}$ and the excitation frequency $f = \omega/(2\pi)$. This figure is obtained from [10].

In conclusion, we have replicated the calculation reported in Ref. [52, 55] for the third-order Kerr and third-harmonic current densities of 2D SLG. We find that the Ref. [52,55] result for the Kerr current density omits a contribution to the total current density from the resonance at $\epsilon = \pm\hbar\omega/2$. We also identify possible mechanisms by which these errors came to be in Ref. [52, 55].

REFERENCES

1. Ferrari, A. C.; Bonaccorso, F.; Fal'ko, V.; Novoselov, K. S.; Roche, S.; Boggild, P.; Borini, S.; Koppens, F. H. L.; Palermo, V.; Pugno, N.; Garrido, J. A.; Sordan, R.; Bianco, A.; Ballerini, L.; Prato, M.; Lidorikis, E.; Kivioja, J.; Marinelli, C.; Ryhanen, T.; Morpurgo, A.; Coleman, J. N.; Nicolosi, V.; Colombo, L.; Fert, A.; Garcia-Hernandez, M.; Bachtold, A.; Schneider, G. F.; Guinea, F.; Dekker, C.; Barbone, M.; Sun, Z.; Galiotis, C.; Grigorenko, A. N.; Konstantatos, G.; Kis, A.; Katsnelson, M.; Vandersypen, L.; Loiseau, A.; Morandi, V.; Neumaier, D.; Treossi, E.; Pellegrini, V.; Polini, M.; Tredicucci, A.; Williams, G. M.; Hee Hong, B.; Ahn, J.-H.; Min Kim, J.; Zirath, H.; van Wees, B. J.; van der Zant, H.; Occhipinti, L.; Di Matteo, A.; Kinloch, I. A.; Seyller, T.; Quesnel, E.; Feng, X.; Teo, K.; Rupesinghe, N.; Hakonen, P.; Neil, S. R. T.; Tannock, Q.; Lofwander, T.; Kinaret, J. Science and technology roadmap for graphene, related two-dimensional crystals, and hybrid systems. *Nanoscale*, **2015**, 7, 4598–4810.

2. Abergel, D. S. L.; Apalkov, V.; Berashevich, J.; Ziegler, K.; Chakraborty, T. Properties of graphene: a theoretical perspective. *Advances in Physics*, **2010**, 59(*4*), 261–482.

3. Kroemer, H. Nobel lecture: Quasielectric fields and band offsets: teaching electrons new tricks. *Reviews of Modern Physics*, **2001**, 73(*3*), 783.

4. Shen, H.; Shi, Y.; Wang, X. Synthesis, charge transport and device applications of graphene nanoribbons. *Synthetic Metals*, **2015**, 210, 109–122.

5. Xu, W.; Lee, T.-W. Recent progress in fabrication techniques of graphene nanoribbons. *Materials Horizons*, **2016**, 3(*3*), 186–207.

6. Castro Neto, A. H.; Guinea, F.; Peres, N. M. R.; Novoselov, K. S.; Geim, A. K. The electronic properties of graphene. *Reviews of Modern Physics*, **2009**, 81(*1*), 109–162.

7. Das Sarma, S.; Adam, S.; Hwang, E. H.; Rossi, E. Electronic transport in two-dimensional graphene. *Reviews of Modern Physics*, **2011**, 83(*2*), 407.

8. Glazov, M. M.; Ganichev, S. D. High frequency electric field induced nonlinear effects in graphene. *Physics Reports*, **2014**, 535(*3*), 101–138.

9. Duan, Z.; Liao, W.; Zhou, G. Infrared optical response of metallic graphene nanoribbons. *Advances in Condensed Matter Physics*, **2010**, 2010, 258019.

10. Wang, Y.; Andersen, D. R. First-principles study of the terahertz third-order nonlinear response of metallic armchair graphene nanoribbons. *Physical Review B*, **2016**, 93(*23*), 235430.

11. Joachim, C.; Renaud, N.; Hliwa, M. The different designs of molecule logic gates. *Advanced Materials*, **2012**, 24(*2*), 312–317.

12. Trauzettel, B.; Bulaev, D. V.; Loss, D.; Burkard, G. Spin qubits in graphene quantum dots. *Nature Physics*, **2007**, 3(*3*), 192–196.

13. Rycerz, A.; Tworzydło, J.; Beenakker, C. Valley filter and valley valve in graphene. *Nature Physics*, **2007**, 3(*3*), 172–175.

14. Guo, G.-P.; Lin, Z.-R.; Tu, T.; Cao, G.; Li, X.-P.; Guo, G.-C. Quantum computation with graphene nanoribbon. *New Journal of Physics*, **2009**, 11(*12*), 123005.

15. Chen, C.-C.; Chang, Y.-C. Theoretical studies of graphene nanoribbon quantum dot qubits. *Physical Review B*, **2015**, 92(*24*), 245406.

16. Mikhailov, S. A. Non-linear electromagnetic response of graphene. *Europhysics Letters*, **2007**, 79(*2*), 27002.

17. Hendry, E.; Hale, P. J.; Moger, J.; Savchenko, A. K.; Mikhailov, S. A. Coherent nonlinear optical response of graphene. *Physical Review Letters*, **2010**, 105(*9*), 097401.

18. Gu, T.; Petrone, N.; McMillan, J. F.; van der Zande, A.; Yu, M.; Lo, G.-Q.; Kwong, D.-L.; Hone, J.; Wong, C. W. Regenerative oscillation and four-wave mixing in graphene optoelectronics. *Nature Photonics*, **2012**, 6(*8*), 554–559.

19. Kumar, N.; Kumar, J.; Gerstenkorn, C.; Wang, R.; Chiu, H.-Y.; Smirl, A. L.; Zhao, H. Third harmonic generation in graphene and few-layer graphite films. *Physical Review B*, **2013**, 87(*12*), 121406.

20. Maeng, I.; Lim, S.; Chae, S. J.; Lee, Y. H.; Choi, H.; Son, J.-H. Gate-controlled nonlinear conductivity of dirac fermion in graphene field-effect transistors measured by terahertz time-domain spectroscopy. *Nano Letters*, **2012**, 12(*2*), 551–555.

21. Hafez, H. A.; Al-Naib, I.; Dignam, M. M.; Sekine, Y.; Oguri, K.; Blanchard, F.; Cooke, D. G.; Tanaka, S.; Komori, F.; Hibino, H.; Ozaki, T. Nonlinear terahertz field-induced carrier dynamics in photoexcited epitaxial monolayer graphene. *Physical Review B*, **2015**, 91(*3*), 035422.

22. Wang, X.; Ouyang, Y.; Jiao, L.; Wang, H.; Xie, L.; Wu, J.; Guo, J.; Dai, H. Graphene nanoribbons with smooth edges behave as quantum wires. *Nature Nanotechnology*, **2011**, 6(*9*), 563–567.

23. Son, Y.-W.; Cohen, M. L.; Louie, S. G. Energy gaps in graphene nanoribbons. *Physical Review Letters*, **2006**, 97(*21*), 216803.

24. Yang, L.; Park, C.-H.; Son, Y.-W.; Cohen, M. L.; Louie, S. G. Quasiparticle energies and band gaps in graphene nanoribbons. *Physical Review Letters*, **2007**, 99(*18*), 186801.

25. Raza, H.; Kan, E. C. Armchair graphene nanoribbons: Electronic structure and electric-field modulation. *Physical Review B*, **2008**, 77(*24*), 245434.

26. Akhmerov, A. R.; Beenakker, C. W. J. Boundary conditions for dirac fermions on a terminated honeycomb lattice. *Physical Review B*, **2008**, 77(*8*), 085423.

27. Evaldsson, M.; Zozoulenko, I. V.; Xu, H.; Heinzel, T. Edge-disorder-induced anderson localization and conduction gap in graphene nanoribbons. *Physical Review B*, **2008**, 78(*16*), 161407.

28. Gunlycke, D.; Li, J.; Mintmire, J. W.; White, C. T. Edges bring new dimension to graphene nanoribbons. *Nano Letters*, **2010**, 10(*9*), 3638–3642.

29. Li, X.; Zhang, T.-Y.; Su, Y. J. Periodically modulated size-dependent elastic properties of armchair graphene nanoribbons. *Nano Letters*, **2015**, 15(*8*), 4883–4888.

30. Shen, S.-Q. *Topological Insulators: Dirac Equation in Condensed Matters*, volume 174; Springer Heidelberg: New York, 2012.

31. Jeong, Y. H.; Kim, S. C.; Yang, S.-R. E. Topological gap states of semiconducting armchair graphene ribbons. *Physical Review B*, **2015**, 91(*20*), 205441.

32. Ang, Y. S.; Zhang, C. Subgap optical conductivity in semihydrogenated graphene. *Applied Physics Letters*, **2011**, 98(*4*), 042107.

33. Ang, Y. S.; Sultan, S.; Tawfiq, A.; Cao, J.; Zhang, C. Terahertz photon mixing effect in gapped graphene. *Journal of Infrared, Millimeter and Terahertz Waves*, **2012**, 33(*8*), 816–824.

34. Cheng, J. L.; Vermeulen, N.; Sipe, J. E. Numerical study of the optical nonlinearity of doped and gapped graphene: From weak to strong field excitation. *Physical Review B*, **2015**, 92(*23*), 235307.

35. Burset, P.; Yeyati, A. L.; Brey, L.; Fertig, H. A. Transport in superlattices on single-layer graphene. *Physical Review B*, **2011**, 83(*19*), 195434.

36. Beenakker, C. W. J. Colloquium: Andreev reflection and klein tunneling in graphene. *Reviews of Modern Physics*, **2008**, 80(*4*), 1337.

37. Raza, H. *Graphene nanoelectronics: Metrology, synthesis, properties and applications*, 1st ed.; Springer-Verlag: Berlin, 2012.

38. Akkermans, E.; Montambaux, G. *Mesoscopic physics of electrons and photons*, 1st ed.; Cambridge University Press: Cambridge, 2007.

39. Andersen, D. R.; Raza, H. Plasmon dispersion in semimetallic armchair graphene nanoribbons. *Physical Review B*, **2012**, 85(*7*), 075425.

40. Andersen, D. R.; Raza, H. Collective modes of massive dirac fermions in armchair graphene nanoribbons. *Journal of Physics: Condensed Matter*, **2013**, 25(*4*), 045303.

41. Brey, L.; Fertig, H. A. Electronic states of graphene nanoribbons studied with the dirac equation. *Physical Review B*, **2006**, 73(*23*), 235411.

42. Brey, L.; Fertig, H. A. Elementary electronic excitations in graphene nanoribbons. *Physical Review B*, **2007**, 75(*12*), 125434.

43. Zheng, H.; Wang, Z. F.; Luo, T.; Shi, Q. W.; Chen, J. Analytical study of electronic structure in armchair graphene nanoribbons. *Physical Review B*, **2007**, 75(*16*), 165414.

44. Han, M. Y.; Özyilmaz, B.; Zhang, Y.; Kim, P. Energy band-gap engineering of graphene nanoribbons. *Physical Review Letters*, **2007**, 98(*20*), 206805.

45. Li, X.; Wang, X.; Zhang, L.; Lee, S.; Dai, H. Chemically derived, ultrasmooth graphene nanoribbon semiconductors. *Science*, **2008**, 319(*5867*), 1229–1232.

46. Jiao, L.; Wang, X.; Diankov, G.; Wang, H.; Dai, H. Facile synthesis of high-quality graphene nanoribbons. *Nature Nanotechnology*, **2010**, 5(*5*), 321–325.

47. Safron, N. S.; Kim, M.; Gopalan, P.; Arnold, M. S. Barrier-guided growth of micro-and nano-structured graphene. *Advanced Materials*, **2012**, 24(*8*), 1041–1045.

48. Kimouche, A.; Ervasti, M. M.; Drost, R.; Halonen, S.; Harju, A.; Joensuu, P. M.; Sainio, J.; Liljeroth, P. Ultra-narrow metallic armchair graphene nanoribbons. *Nature Communications*, **2015**, 6, 10177.

49. Jacobberger, R. M.; Kiraly, B.; Fortin-Deschenes, M.; Levesque, P. L.; McElhinny, K. M.; Brady, G. J.; Delgado, R. R.; Roy, S. S.; Mannix, A.; Lagally, M. G.; Evans, P. G.; Desjardins, P.; Martel, R.; Hersam, M. C.; Guisinger, N. P.; Arnold, M. S. Direct oriented growth of armchair graphene nanoribbons on germanium. *Nature Communications*, **2015**, 6, 8006.

50. Park, C.-H.; Son, Y.-W.; Yang, L.; Cohen, M. L.; Louie, S. G. Electron beam supercollimation in graphene superlattices. *Nano Letters*, **2008**, 8(*9*), 2920–2924.

51. Ang, Y. S.; Zhang, C. Enhanced optical conductance in graphene superlattice due to anisotropic band dispersion. *Journal of Physics D: Applied Physics*, **2012**, 45(*39*), 395303.

52. Wright, A. R.; Xu, X. G.; Cao, J. C.; Zhang, C. Strong nonlinear optical response of graphene in the terahertz regime. *Applied Physics Letters*, **2009**, 95(*7*), 072101.

53. Mahan, G. D. *Many-Particle Physics*, 3rd ed.; Springer Science & Business Media: New York, 2000.

54. Ryu, S.; Mudry, C.; Furusaki, A.; Ludwig, A. W. W. Landauer conductance and twisted boundary conditions for dirac fermions in two space dimensions. *Physical Review B*, **2007**, 75(*20*), 205344.

55. Ang, Y. S.; Chen, Q.; Zhang, C. Nonlinear optical response of graphene in terahertz and near-infrared frequency regime. *Frontiers of Optoelectronics*, **2015**, 8(*1*), 3–26.

56. Lopez-Rodriguez, F. J.; Naumis, G. G. Analytic solution for electrons and holes in graphene under electromagnetic waves: gap appearance and nonlinear effects. *Physical Review B*, **2008**, 78(*20*), 201406.

57. Ang, Y. S.; Sultan, S.; Zhang, C. Nonlinear optical spectrum of bilayer graphene in the terahertz regime. *Applied Physics Letters*, **2010**, 97(*24*), 243110.

58. Zhou, Y.; Wu, M. W. Optical response of graphene under intense terahertz fields. *Physical Review B*, **2011**, 83(*24*), 245436.

59. Ando, T.; Nakanishi, T.; Saito, R. Berry's phase and absence of back scattering in carbon nanotubes. *Journal of the Physical Society of Japan*, **1998**, 67(*8*), 2857–2862.

60. Arons, M. E.; Han, M. Y.; Sudarshan, E. C. G. Finite quantum electrodynamics: A field theory using an indefinite metric. *Physical Review*, **1965**, 137(*4B*), B1085–B1104.

61. Tworzydło, J.; Trauzettel, B.; Titov, M.; Rycerz, A.; Beenakker, C. W. J. Sub-poissonian shot noise in graphene. *Physical Review Letters*, **2006**, 96(*24*), 246802.

62. Nair, R. R.; Blake, P.; Grigorenko, A. N.; Novoselov, K. S.; Booth, T. J.; Stauber, T.; Peres, N. M. R.; Geim, A. K. Fine structure constant defines visual transparency of graphene. *Science*, **2008**, 320(*5881*), 1308–1308.

63. Mikhailov, S. A.; Ziegler, K. Nonlinear electromagnetic response of graphene: frequency multiplication and the self-consistent-field effects. *Journal of Physics: Condensed Matter*, **2008**, 20(*38*), 384204.

64. Mikhailov, S. A. Theory of the nonlinear optical frequency mixing effect in graphene. *Physica E: Low-dimensional Systems and Nanostructures*, **2012**, 44(*6*), 924–927.

65. Gullans, M.; Chang, D. E.; Koppens, F. H. L.; Javier García de Abajo, F.; Lukin, M. D. Single-photon nonlinear optics with graphene plasmons. *Physical Review Letters*, **2013**, 111(*24*), 247401.

66. Mikhailov, S. A. Quantum theory of third-harmonic generation in graphene. *Physical Review B*, **2014**, 90(*24*), 241301(R).

67. Mikhailov, S. A. Erratum: Quantum theory of third-harmonic generation in graphene [Phys. Rev. B **90** , 241301(R) (2014)]. *Physical Review B*, **2015**, 91, 039904(E).

68. Mikhailov, S. A. Quantum theory of the third-order nonlinear electrodynamic effects of graphene. *Physical Review B*, **2016**, 93(*8*), 085403.

69. Cheng, J. L.; Vermeulen, N.; Sipe, J. E. Third order optical nonlinearity of graphene. *New Journal of Physics*, **2014**, 16(*5*), 053014.

70. Cheng, J. L.; Vermeulen, N.; Sipe, J. E. Corrigendum: Third order optical nonlinearity of graphene (2014 New J. Phys. 16 053014). *New Journal of Physics*, **2016**, 18(*2*), 029501.

71. Cheng, J. L.; Vermeulen, N.; Sipe, J. E. Third-order nonlinearity of graphene: Effects of phenomenological relaxation and finite temperature. *Physical Review B*, **2015**, 91(*23*), 235320.

72. Cheng, J. L.; Vermeulen, N.; Sipe, J. E. Erratum: Third-order nonlinearity of graphene: Effects of phenomenological relaxation and finite temperature [Phys. Rev. B **91** , 235320 (2015)]. *Physical Review B*, **2016**, 93, 039904(E).

73. Morimoto, T.; Nagaosa, N. Scaling laws for nonlinear electromagnetic responses of dirac fermion. *Physical Review B*, **2016**, 93(*12*), 125125.

74. Bao, Q.; Loh, K. P. Graphene photonics, plasmonics, and broadband optoelectronic devices. *ACS Nano*, **2012**, 6(*5*), 3677–3694.

75. Sasaki, K. I.; Kato, K.; Tokura, Y.; Oguri, K.; Sogawa, T. Theory of optical transitions in graphene nanoribbons. *Physical Review B*, **2011**, 84(*8*), 085458.

76. Chung, H. C.; Lee, M. H.; Chang, C. P.; Lin, M. F. Exploration of edge-dependent optical selection rules for graphene nanoribbons. *Optics Express*, **2011**, 19(*23*), 23350–23363.

77. Strikha, M. V.; Vasko, F. T. Electro-optics of graphene: Field-modulated reflection and birefringence. *Physical Review B*, **2010**, 81(*11*), 115413.

78. Winnerl, S.; Göttfert, F.; Mittendorff, M.; Schneider, H.; Helm, M.; Winzer, T.; Malic, E.; Knorr, A.; Orlita, M.; Potemski, M.; Sprinkle, M.; Berger, C.; de Heer, W. A. Time-resolved spectroscopy on epitaxial graphene in the infrared spectral range: relaxation dynamics and saturation behavior. *Journal of Physics: Condensed Matter*, **2013**, 25(*5*), 054202.

79. Mishchenko, E. G. Dynamic conductivity in graphene beyond linear response. *Physical Review Letters*, **2009**, 103(*24*), 246802.

80. Nasari, H.; Abrishamian, M. S.; Berini, P. Nonlinear optics of surface plasmon polaritons in subwavelength graphene ribbon resonators. *Optics Express*, **2016**, 24(*1*), 708–723.

81. Wang, Y.; Andersen, D. R. Quantum size effects in the terahertz nonlinear response of metallic armchair graphene nanoribbons. *IEEE Journal of Selected Topics in Quantum Electronics*, **2017**, 23(*1*), 5100108.

82. Liao, W.; Zhou, G.; Xi, F. Optical properties for armchair-edge graphene nanoribbons. *Journal of Applied Physics*, **2008**, 104(*12*), 126105.

83. Mašek, J.; Kramer, B. On the conductance of finite systems in the ballistic regime: dependence on fermi energy, magnetic field, frequency, and disorder. *Zeitschrift für Physik B Condensed Matter*, **1989**, 75(*1*), 37–45.

84. Velickỳ, B.; Mašek, J.; Kramer, B. ac-conductance of an infinite ideal quantum wire in an electric field with arbitrary spatial distribution. *Physics Letters A*, **1989**, 140(*7*), 447–450.

85. Kramer, B.; Mašek, J.; Špička, V.; Velickỳ, B. Coherent electronic transport properties of quasi-one-dimensional systems. *Surface Science*, **1990**, 229(*1*), 316–320.

86. Wróbel, J.; Kuchar, F.; Ismail, K.; Lee, K. Y.; Nickel, H.; Schlapp, W. Quantized conductance of a quasi-ballistic one-dimensional wire. *Surface Science*, **1992**, 263(*1*), 261–264.

87. Wróbel, J.; Kuchar, F.; Ismail, K.; Lee, K. Y.; Nickel, H.; Schlapp, W.; Grabecki, G.; Dietl, T. The influence of reduced dimensionality on the spin-splitting in gaalas/gaas quantum wires. *Surface Science*, **1994**, 305(*1*), 615–619.

88. Winnerl, S.; Orlita, M.; Plochocka, P.; Kossacki, P.; Potemski, M.; Winzer, T.; Malic, E.; Knorr, A.; Sprinkle, M.; Berger, C.; de Heer, W. A.; Schneider, H.; Helm, M. Carrier relaxation in epitaxial graphene photoexcited near the dirac point. *Physical Review Letters*, **2011**, 107(*23*), 237401.

89. Strait, J. H.; Wang, H.; Shivaraman, S.; Shields, V.; Spencer, M.; Rana, F. Very slow cooling dynamics of photoexcited carriers in graphene observed by optical-pump terahertz-probe spectroscopy. *Nano Letters*, **2011**, 11(*11*), 4902–4906.

90. Johannsen, J. C.; Ulstrup, S.; Cilento, F.; Crepaldi, A.; Zacchigna, M.; Cacho, C.; Turcu, I. C. E.; Springate, E.; Fromm, F.; Raidel, C.; Seyller, T.; Parmigiani, F.; Grioni, M.; Hofmann, P. Direct view of hot carrier dynamics in graphene. *Physical Review Letters*, **2013**, 111(*2*), 027403.

91. Gierz, I.; Petersen, J. C.; Mitrano, M.; Cacho, C.; Turcu, I. E.; Springate, E.; Stöhr, A.; Köhler, A.; Starke, U.; Cavalleri, A. Snapshots of non-equilibrium dirac carrier distributions in graphene. *Nature Materials*, **2013**, 12(*12*), 1119–1124.

92. George, P. A.; Strait, J.; Dawlaty, J.; Shivaraman, S.; Chandrashekhar, M.; Rana, F.; Spencer, M. G. Ultrafast optical-pump terahertz-probe spectroscopy of the carrier relaxation and recombination dynamics in epitaxial graphene. *Nano Letters*, **2008**, 8(*12*), 4248–4251.

93. Jnawali, G.; Rao, Y.; Yan, H.; Heinz, T. F. Observation of a transient decrease in terahertz conductivity of single-layer graphene induced by ultrafast optical excitation. *Nano Letters*, **2013**, 13(*2*), 524–530.

94. Yang, Y.; Murali, R. Impact of size effect on graphene nanoribbon transport. *IEEE Electron Device Letters*, **2010**, 31(*3*), 237–239.

95. Liao, A. D.; Wu, J. Z.; Wang, X.; Tahy, K.; Jena, D.; Dai, H.; Pop, E. Thermally limited current carrying ability of graphene nanoribbons. *Physical Review Letters*, **2011**, 106(*25*), 256801.

96. Thongrattanasiri, S.; Manjavacas, A.; Javier García de Abajo, F. Quantum finite-size effects in graphene plasmons. *ACS Nano*, **2012**, 6(*2*), 1766–1775.

97. Romanets, P. N.; Vasko, F. T. Transient response of intrinsic graphene under ultrafast interband excitation. *Physical Review B*, **2010**, 81(*8*), 085421.

98. Tse, W.-K.; Das Sarma, S. Energy relaxation of hot dirac fermions in graphene. *Physical Review B*, **2009**, 79(*23*), 235406.

99. Bischoff, D.; Varlet, A.; Simonet, P.; Eich, M.; Overweg, H. C.; Ihn, T.; Ensslin, K. Localized charge carriers in graphene nanodevices. *Applied Physics Reviews*, **2015**, 2(*3*), 031301.

100. Born, M.; Wolf, E. *Principles of Optics*, 7th ed.; Cambridge University Press: Cambridge, UK, 1999.

101. Rotenberg, E.; Bostwick, A.; Ohta, T.; McChesney, J. L.; Seyller, T.; Horn, K. Origin of the energy bandgap in epitaxial graphene. *Nature Materials*, **2008**, 7(*4*), 258–259.

102. Xia, F.; Perebeinos, V.; Lin, Y.-m.; Wu, Y.; Avouris, P. The origins and limits of metal-graphene junction resistance. *Nature Nanotechnology*, **2011**, 6(*3*), 179–184.

103. Chen, Y.-C.; Cao, T.; Chen, C.; Pedramrazi, Z.; Haberer, D.; de Oteyza, D. G.; Fischer, F. R.; Louie, S. G.; Crommie, M. F. Molecular bandgap engineering of bottom-up synthesized graphene nanoribbon heterojunctions. *Nature Nanotechnology*, **2015**, 10(*2*), 156–160.

104. Cheng, F.; Zhou, G. Alternating current transport property for a two-channel interacting quantum wire. *Solid State Communications*, **2011**, 151(*18*), 1256–1260.

105. Glazov, M. M. Second harmonic generation in graphene. *JETP Letters*, **2011**, 93(*7*), 366–371.

106. Kravets, V. G.; Grigorenko, A. N.; Nair, R. R.; Blake, P.; Anissimova, S.; Novoselov, K. S.; Geim, A. K. Spectroscopic ellipsometry of graphene and an exciton-shifted van hove peak in absorption. *Physical Review B*, **2010**, 81(*15*), 155413.

107. Oka, T.; Aoki, H. Photovoltaic hall effect in graphene. *Physical Review B*, **2009**, 79(*8*), 081406.

108. Karch, J.; Olbrich, P.; Schmalzbauer, M.; Zoth, C.; Brinsteiner, C.; Fehrenbacher, M.; Wurstbauer, U.; Glazov, M. M.; Tarasenko, S. A.; Ivchenko, E. L.; Weiss, D.; Eroms, J.; Yakimova, S.; Lara-Avila, S.; Kubatkin, S.; Ganichev, S. D. Dynamic hall effect driven by circularly polarized light in a graphene layer. *Physical Review Letters*, **2010**, 105(*22*), 227402.

109. Jiang, C.; Shalygin, V. A.; Panevin, V. Y.; Danilov, S. N.; Glazov, M. M.; Yakimova, R.; Lara-Avila, S.; Kubatkin, S.; Ganichev, S. Helicity-dependent photocurrents in graphene layers excited by midinfrared radiation of a co 2 laser. *Physical Review B*, **2011**, 84(*12*), 125429.

110. Karch, J.; Olbrich, P.; Schmalzbauer, M.; Brinsteiner, C.; Wurstbauer, U.; Glazov, M. M.; Tarasenko, S. A.; Ivchenko, E. L.; Weiss, D.; Eroms, J.; Ganichev, S. D. Photon helicity driven electric currents in graphene. *arXiv preprint arXiv:1002.1047*, **2010**.

111. Karch, J.; Drexler, C.; Olbrich, P.; Fehrenbacher, M.; Hirmer, M.; Glazov, M. M.; Tarasenko, S. A.; Ivchenko, E. L.; Birkner, B.; Eroms, J.; Weiss, D.; Yakimova, R.; Lara-Avila, S.; Kubatkin, S.; Ostler, M.; Seyller, T.; Ganichev, S. D. Terahertz radiation driven chiral edge currents in graphene. *Physical Review Letters*, **2011**, 107(*27*), 276601.

112. Liu, Y.; Bian, G.; Miller, T.; Chiang, T.-C. Visualizing electronic chirality and berry phases in graphene systems using photoemission with circularly polarized light. *Physical Review Letters*, **2011**, 107(*16*), 166803.

113. Sørngård, S. A.; Simonsen, S. I.; Hansen, J. P. High-order harmonic generation from graphene: Strong attosecond pulses with arbitrary polarization. *Physical Review A*, **2013**, 87(*5*), 053803.

114. Gu, Z.; Fertig, H. A.; Arovas, D. P.; Auerbach, A. Floquet spectrum and transport through an irradiated graphene ribbon. *Physical Review Letters*, **2011**, 107, 216601.

115. Calvo, H. L.; Perez-Piskunow, P. M.; Pastawski, H. M.; Roche, S.; Torres, L. E. F. F. Non-perturbative effects of laser illumination on the electrical properties of graphene nanoribbons. *Journal of Physics: Condensed Matter*, **2013**, 25(*14*), 144202.

116. Wang, X.; Ouyang, Y.; Li, X.; Wang, H.; Guo, J.; Dai, H. Room-temperature all-semiconducting sub-10-nm graphene nanoribbon field-effect transistors. *Physical Review Letters*, **2008**, 100(*20*), 206803.

117. Banadaki, Y. M.; Srivastava, A. Investigation of the width-dependent static characteristics of graphene nanoribbon field effect transistors using non-parabolic quantum-based model. *Solid-State Electronics*, **2015**, 111, 80–90.

118. Nanmeni Bondja, C.; Geng, Z.; Granzner, R.; Pezoldt, J.; Schwierz, F. Simulation of 50-nm gate graphene nanoribbon transistors. *Electronics*, **2016**, 5(*1*), 3.

119. Wong, J.-H.; Wu, B.-R.; Yang, P.-H.; Lin, M.-F. Low-energy electronic properties of graphene and armchair ribbon superlattices. *The Journal of Physical Chemistry C*, **2013**, 117(*14*), 7326–7333.

120. Yuan, S.; Roldán, R.; Jauho, A.-P.; Katsnelson, M. I. Electronic properties of disordered graphene antidot lattices. *Physical Review B*, **2013**, 87(*8*), 085430.

121. Gómez, S.; Burset, P.; Herrera, W. J.; Yeyati, A. L. Selective focusing of electrons and holes in a graphene-based superconducting lens. *Physical Review B*, **2012**, 85(*11*), 115411.

122. Rozhansky, I. V.; Kachorovskii, V. Y.; Shur, M. S. Helicity-driven ratchet effect enhanced by plasmons. *Physical Review Letters*, **2015**, 114(*24*), 246601.

123. Huidobro, P. A.; Kraft, M.; Maier, S. A.; Pendry, J. B. Graphene as a tunable anisotropic or isotropic plasmonic metasurface. *ACS Nano*, **2016**, 10(*5*), 5499–5506.

124. Pal, G.; Apel, W.; Schweitzer, L. Landau level splitting due to graphene superlattices. *Physical Review B*, **2012**, 85(*23*), 235457.

125. Park, C.-H.; Yang, L.; Son, Y.-W.; Cohen, M. L.; Louie, S. G. Anisotropic behaviours of massless dirac fermions in graphene under periodic potentials. *Nature Physics*, **2008**, 4(*3*), 213–217.

126. Park, C.-H.; Yang, L.; Son, Y.-W.; Cohen, M. L.; Louie, S. G. New generation of massless dirac fermions in graphene under external periodic potentials. *Physical Review Letters*, **2008**, 101(*12*), 126804.

127. Savelev, S. E.; Alexandrov, A. S. Massless dirac fermions in a laser field as a counterpart of graphene superlattices. *Physical Review B*, **2011**, 84(*3*), 035428.

128. de Dios-Leyva, M.; Cuan, R. Group velocity in finite graphene superlattices. *Superlattices and Microstructures*, **2015**, 83, 488–497.

129. Jiang, L.; Yuan, R.-Y.; Zhao, X.; Lv, J.; Yan, H. Nonlinear optical response in kronig–penney type graphene superlattice in terahertz regime. *Modern Physics Letters B*, **2015**, 29(*13*), 1550060.

130. Mittendorff, M.; Winnerl, S.; Kamann, J.; Eroms, J.; Weiss, D.; Schneider, H.; Helm, M. Ultrafast graphene-based broadband thz detector. *Applied Physics Letters*, **2013**, 103(*2*), 021113.

131. Meunier, V.; Souza Filho, A. G.; Barros, E. B.; Dresselhaus, M. S. Physical properties of low-dimensional sp^2-based carbon nanostructures. *Reviews of Modern Physics*, **2016**, 88, 025005.

132. Dolcini, F.; Grabert, H.; Safi, I.; Trauzettel, B. Oscillatory nonlinear conductance of an interacting quantum wire with an impurity. *Physical Review Letters*, **2003**, 91(*26*), 266402.

133. Bockrath, M.; Cobden, D. H.; Lu, J.; Rinzler, A. G.; Smalley, R. E.; Balents, L.; McEuen, P. L. Luttinger-liquid behaviour in carbon nanotubes. *Nature*, **1999**, 397(*6720*), 598–601.

134. Trauzettel, B.; Safi, I.; Dolcini, F.; Grabert, H. Appearance of fractional charge in the noise of nonchiral luttinger liquids. *Physical Review Letters*, **2004**, 92(*22*), 226405.

135. Cuniberti, G.; Sassetti, M.; Kramer, B. Transport and elementary excitations of a luttinger liquid. *Journal of physics: Condensed matter*, **1996**, 8(*2*), L21–L26.

136. Burke, P. J. Luttinger liquid theory as a model of the gigahertz electrical properties of carbon nanotubes. *IEEE Transactions on Nanotechnology*, **2002**, 1(*3*), 129–144.

137. Naeemi, A.; Meindl, J. D. Compact physics-based circuit models for graphene nanoribbon interconnects. *IEEE Transactions on Electron Devices*, **2009**, 56(*9*), 1822–1833.

138. Imambekov, A.; Glazman, L. I. Universal theory of nonlinear luttinger liquids. *Science*, **2009**, 323(*5911*), 228–231.

139. Villegas, C. E. P.; Tavares, M. R. S.; Hai, G.-Q.; Vasilopoulos, P. Plasmon modes and screening in double metallic armchair graphene nanoribbons. *Physical Review B*, **2013**, 88(*16*), 165426.

140. Shylau, A. A.; Badalyan, S. M.; Peeters, F. M.; Jauho, A.-P. Electron polarization function and plasmons in metallic armchair graphene nanoribbons. *Physical Review B*, **2015**, 91(*20*), 205444.

141. Sanderson, M.; Ang, Y. S.; Gong, S.; Zhao, T.; Hu, M.; Zhong, R.; Chen, X.; Zhang, P.; Zhang, C.; Liu, S. Optical bistability induced by nonlinear surface plasmon polaritons in graphene in terahertz regime. *Applied Physics Letters*, **2015**, 107(*20*), 203113.

142. Kumar, V.; Kumar, U.; Setlur, G. S.; others,. Coherent nonlinear electromagnetic response in twisted bilayer and few-layer graphene. *Pramana*, **2014**, 83(*4*), 597–617.

143. Liu, Z.; Sanderson, M.; Zhang, C.; Cao, J. C. Nonlinear optical conductivity of bilayer graphene with rashba spin-orbit interaction in the terahertz regime. *Journal of Applied Physics*, **2015**, 118(*4*), 043106.

144. Bonaccorso, F.; Colombo, L.; Yu, G.; Stoller, M.; Tozzini, V.; Ferrari, A. C.; Ruoff, R. S.; Pellegrini, V. Graphene, related two-dimensional crystals, and hybrid systems for energy conversion and storage. *Science*, **2015**, 347(*6217*), 1246501.

145. Gradshteyn, I. S.; Ryzhik, I. M. *Table of integrals, series, and products*, 8th ed.; Elsevier: amsterdam, 2014.

146. Ang, Y. S.; Chen, Q.; Zhang, C. Nonlinear optical response of graphene in terahertz and near-infrared frequency regime. *Frontiers of Optoelectronics*, **2015**, 8(*1*), 3–26.

147. Caffarelli, L.; Silvestre, L. An extension problem related to the fractional laplacian. *Communications in Partial Differential Equations*, **2007**, 32(*8*), 1245–1260.

148. Wei, G. W.; Zhao, Y. B.; Xiang, Y. Discrete singular convolution and its application to the analysis of plates with internal supports. part 1: Theory and algorithm. *International Journal for Numerical Methods in Engineering*, **2002**, 55(*8*), 913–946.

149. Katz, M. G.; Tall, D. A cauchy-dirac delta function. *Foundations of Science*, **2013**, 18(*1*), 107–123.

150. Liu, X.; Jin, X.; Lee, J.-H.; Zhu, L.; Kwon, H.-I.; Lee, J.-H. A full analytical model of fringing-field-induced parasitic capacitance for nano-scaled mosfets. *Semiconductor Science and Technology*, **2010**, 25(*1*), 015008.

151. Vladimirov, V. S. *Equations of Mathematical Physics*, 2nd ed.; Marcel Dekker: New York, 1971.